Modelling External Light Transmission Through to the Human Fetus

A thesis

submitted in partial fulfilment

of the requirements for the Degree

of

Doctor of Philosophy in Mathematics

at

The University of Waikato

by

Zac Isaac

THE UNIVERSITY OF
WAIKATO
Te Whare Wānanga o Waikato

2024

Abstract

Little is known about the visual experience of human fetuses within the womb. For many years, the uterus was assumed to be a dark environment, limited only to illumination under intense radiation. Recent research, however, shows that the human fetus exhibits brain activity when presented with visual stimuli and displays a preference for face-like stimuli presented via laser diode application to the maternal abdominal exterior. Despite growing evidence to support the notion of a visually engaged fetus during gestation, there has been minimal research undertaken to determine the extent to which the human uterus is illuminated by external light sources. Beyond aiding with experimental research in fetal vision, an understanding of uterine illumination begins to reveal the impact of varying environmental conditions on the fetal visual experience, with direct relevance to ongoing research across fields such as fetal vision, photoacoustics, and ectogenesis. This thesis outlines a mathematical model developed for the purposes of simulating the propagation of light sources through maternal tissue to the human fetus, with applications exploring the effect of adipose on transdermal monochromatic stimuli, the degree of uterine illumination imposed by natural light, and an extension to the illumination of a full maternal abdomen via a model that can account for curvature, varying tissue layer thicknesses, and the temporal aspects of pregnancy.

Note on Publications

This thesis is with publications. The details of the publications are as follows:

Chapter 3: Submitted, Accepted for Publication

Zac Isaac, Jacob Heerikhuisen, Vincent Reid. The effect of adipose tissue on transdermal monochromatic light presented to the human fetus using Monte Carlo simulations. *Accepted for Publication in Scientific Reports - Nature*, 2024.

Chapter 5: Submitted, Under Review

Zac Isaac, Jacob Heerikhuisen, Vincent Reid. Modeling the propagation of natural light to the human womb using Monte Carlo simulations. *Submitted to Proceedings of the Royal Society B*, 2024.

Chapter 7: To Be Submitted

Zac Isaac, Jacob Heerikhuisen, Vincent Reid. Modeling the full human uterine visual environment. *To be Submitted to Journal of the Royal Society Interface*, 2024.

Acknowledgements

My time at the University of Waikato sums to nearly 9 years in total, and I have met many people here and elsewhere who have contributed to my journey. Below are the acknowledgements that first come to mind.

I wish to initially extend my deepest gratitude and thanks to my Chief Supervisor, Associate Professor Jacob Heerikhuisen. When we first met in 2020, I was a soon-to-be master's student with minimal skills but an enormous desire to learn and grow as a researcher. You guided me through my MSc and offered the chance to work towards a Ph.D. — something I never believed to be within my capability. Your easygoing approach to supervision, teaching, and research has resonated with me from the beginning of my time under your academic wing, and I look back on my growth over the years with both genuine shock at my progress and thankfulness for every aspect of your support and guidance.

Next, I would like to extend my immense gratitude to my Co-Supervisor, Professor Vincent Reid. Your palpable enthusiasm for your field has frequently been the driving factor behind my decisions to continue with this Ph.D., despite regretting beginning the journey many times. You have also continued to offer your time, energy, and advice to support my journey. Your continued support through my difficult stages, my successes, and my failures is something for which I cannot completely express my thanks.

I wish to next thank the collective academic and general staff of the School of Computing and Mathematical Sciences for their various contributions to my academic journey. In particular, I would like to thank Professor Sean Oughton for providing the initial "spark" in my overall research journey, Dr. Woei Chet Lim for consistently being the best lecturer to tutor for, and Maria Admiraal, Buddhika Subasinghe, and Carol Home for putting up with my endless non-academic queries, requests, and problems over the years — and never without a smile!

My close family must surely come next. Each of whom, in their own way,

has contributed immensely in guiding me to this point in my life.

To my mother, Pauline: I joke about how horrible it is to have an Asian mother — always critical of anything below the best in every aspect of life. However, your approach to parenting is what has primarily spurred me to this point in life. You always pressed me to say “yes” to opportunities, and I have carried this attitude with me through life. You grilled me for every academic mistake growing up, and though I deplored it at the time, I look back on those moments as having instilled a desire to succeed and always seek improvement. You are my role model and I love you.

To my brother, Michael: How different we are — one submitting a Ph.D. thesis in mathematics and the other a professional kickboxer. On the surface, it’s unfathomable how we are so closely related. On deeper inspection, however, I can see we are very alike. You are the most determined, disciplined, persevering person I have ever met, and I have frequently looked at you for inspiration when things have gotten tough in my life over the past decade. I cannot verbally express the respect I have for you as a person.

To my father, Paul: thank you for instilling a love of science within me at a young age (intentional or not) and for always reminding me of how your dad never finished his Ph.D. (this was actually very motivating). To my step father, Gordon: thank you for putting up with my mother (!) whenever I’ve given up and for showing me how to keep going every day.

To my girlfriend, Alisha: you bring joy to my life, brighten my days, and I love you. Thank you for being my light at the end of each tunnel.

To my best friend, Hannah: you have been the rock in my life for many years now, walking with me through the trials and tribulations of my entire academic pathway without ever batting an eyelid. I am forever indebted to you.

To my very good friends, Edward, Hamish, Sean, and Tay: the banter and (at times) academic conversations we’ve had over the years have essentially been my fuel on many occasions. Thank you.

To the people across my multiple student clubs and associations, in particular those I’ve met through CS^3: thank you for being the best way to procrastinate from my real work and for the MANY happy memories you’ve

contributed to during my time at university.

I also wish to acknowledge the Royal Society Marsden Fund for providing the research funding to pay for this Ph.D., its associated costs, my living stipend, and my attendance at various conferences over the years.

Finally, as terrible as it is, I want to pat myself on the back. I dropped out of university after one semester and spent years working in supermarkets. Everybody told me I'd never be able to go back and finish my degree. I fought through years of mental health problems, addiction, and suicidal issues. People called me an idiot who'd thrown his life away. Now, I am completing my Ph.D. in mathematics. In doing so, I hope I've made the people I care about proud, and I'd like to respectfully dismiss those who said I couldn't.

List of Figures

List of Tables

Contents

Chapter 1

Introduction

Human life begins within the womb, and for many, this is also the starting point for visual development and visual experience; however, very little is known about the uterine visual landscape. For years, the illumination of this environment by external light sources was assumed to be negligible or zero [Myowa-Yamakoshi and Takeshita, 2006], unless the maternal abdomen was exposed directly to a powerful light source [Liley, 1972].

In recent years, investigations of fetal visual development and the fetal visual experience have been confined to researchers in fields such as Developmental Psychology; however, experimental work indicates that the human fetus is capable of recognising and responding to external visual stimuli, such as laser diodes [Reid et al., 2017], and initial simple modelling performed suggested that the fetus may not develop in the same completely dark environment as previously assumed [Del Giudice, 2011].

Hence, the revelation that the human fetus can be engaged via transdermal laser stimuli has reignited interest in exploring, for instance, the appearance of such stimuli to the fetus and the attenuation of light signals through maternal tissue. Such work is typically performed through the use of mathematical models that utilise Monte Carlo methods, referred to as the “gold standard” in tissue optics [Periyasamy and Pramanik, 2017], to simulate large numbers of photons as they propagate through a tissue environment — in a similar manner to “ray tracing”. These simulations can be constructed to provide an estimate of delivered stimuli brightness, potential visual appearance to the fetus, and an understanding of the relationship between light and maternal tissue.

Further, with the advent of products such as the artificial womb known as BioBag [Partridge et al., 2017], the need for an understanding of how light interfaces with maternal tissue and amniotic fluid to reach the fetus is paramount to ensure that products are developed in a way that replicates the human uterine environment. Similarly, there is motivation in fields such as developmental psychology, transabdominal oximetry, and photoacoustics to explore the extent to which light penetrates maternal abdominal tissue and understand how transdermal stimuli appear to the fetus. Consequently, this research plays a key role in aiding both the future development of commercial products and in guiding future experimental work in fetal vision.

This thesis first outlines the history and concepts involved with Monte Carlo modelling, explores the history of tissue optics, and discusses prior applications of computational modelling techniques to problems involving light and the human fetus. Next, a new mathematical model based on a Monte Carlo algorithm is developed and used to explore the interaction of point light sources with maternal tissue and amniotic fluid on the way to reaching the fetus. This model is then extended and expanded for applications to natural light and clothing. Finally, we introduce tissue curvature and varying tissue thicknesses to allow the model to simulate natural light entering the womb from all directions and across gestation.

1.1 Thesis Objectives

The primary objective of this thesis is to develop and implement mathematical models to simulate the dispersion, scattering, and attenuation of arbitrary light signals projected through dynamically dispersive maternal human tissue.

To achieve this, the following research objectives must be implemented:

1. By incorporating existing datasets and tissue type profiles into the simulations, explore the interaction of light with different tissues to build a realistic model of how external point light sources appear to the fetus. Use this model to investigate the optimal point light source for delivering a visual stimulus to the fetus and to link the intensity of externally applied point sources to the intensity reaching the fetus as a function of the thickness of intervening tissue and fluid layers (Chapter 5).
2. Simulate the effect of skin coverings and extend simulations from point sources of light to natural light sources distributed across larger regions of the maternal abdomen (Chapter 7).
3. Extend the model to account for light entering the curved maternal abdomen from all directions and to enable the model to replicate the evolution of tissue thickness over the course of pregnancy (Chapter 9).

1.2 Contributions

The main contributions of this thesis to the field of research are:

1. Exploring the extent to which point source laser diode stimuli illuminate the womb and offering the first attempt at understanding how such stimuli may appear to the fetus, as well as introducing an adaptable model that can be used for Monte Carlo simulations of photon-tissue interactions.
2. Introducing an expanded approach to Monte Carlo modelling of photon interactions with maternal tissue which provides the field's first attempt at understanding the uterine illumination provided by natural external light sources, as well as an initial understanding of the extent to which clothing impacts the visual environment.

3. Extending the model to allow for curvature of the womb, illumination from all directions with varying intensities, and tissue layer thicknesses that may vary across time and space. This is the first such model of the human womb and allows exploration of the evolution of the uterine visual landscape across the period of gestation.

1.3 List of Publications

During the course of this research, the following articles have been submitted to peer-reviewed journals:

Zac Isaac, Jacob Heerikhuisen, Vincent Reid. The effect of adipose tissue on transdermal monochromatic light presented to the human fetus using Monte Carlo simulations. *Accepted for Publication in Scientific Reports - Nature*, 2024.

Zac Isaac, Jacob Heerikhuisen, Vincent Reid. Modeling the propagation of natural light to the human womb using Monte Carlo simulations. *Submitted to Proceedings of the Royal Society B*, 2024.

The following articles are soon to be submitted to peer-reviewed journals:

Zac Isaac, Jacob Heerikhuisen, Vincent Reid. Modeling the full human uterine visual environment. *To be Submitted to the Journal of the Royal Society Interface*, 2024.

1.4 Chapter Outline

The thesis is organised as follows:

Chapter 2 provides background information that is beneficial for understanding the context of this field, the approaches used in similar applications, and the motivation behind the usage of specific methods in our research.

Chapter 3 provides a comprehensive outline of the base algorithm and theory employed by steady-state Monte Carlo models of light propagation in multiple layers of simple, homogeneous tissue.

Chapter 4 discusses the motivation leading to Chapter 5.

Chapter 5 introduces our developed model and applies it to an initial problem where we explore the extent to which adipose tissue impacts point source stimuli delivered to the fetus.

Chapter 6 discusses the motivation and model development leading to Chapter 7.

Chapter 7 extends the modelling in Chapter 5 to account for natural light across a larger region of tissue and also introduces skin coverings.

Chapter 8 discusses the motivation and model development leading to Chapter 9.

Chapter 9 extends the previous planar tissue modelling to the entire curved human womb, allowing a more physically accurate exploration of the evolution of the entire uterine visual landscape across gestation.

Finally, the thesis is concluded in **Chapter 10** with a discussion of the overall thesis contributions, an analysis of limitations and future improvements, and an overview of further research paths.

References

M. Del Giudice. Alone in the Dark? Modeling the Conditions for Visual Experience in Human Fetuses. *Developmental Psychobiology*, 53:214–219, 2011.

Z. Isaac, J. Heerikhuisen, and V. Reid. The effect of adipose tissue on transdermal monochromatic light presented to the human fetus using Monte Carlo simulations. *Scientific Reports - Nature*, accepted, 2024.

Z. Isaac, J. Heerikhuisen, and V. Reid. Modeling the full human uterine visual environment. *Journal of the Royal Society Interface*, forthcoming.

Z. Isaac, J. Heerikhuisen, and V. Reid. Modeling the propagation of natural light to the human womb using Monte Carlo simulations. *Proceedings of the Royal Society B*, under review, 2024.

A. W. Liley. The foetus as a personality. *Australian & New Zealand Journal of Psychiatry*, 6(2):99–105, 1972.

M. Myowa-Yamakoshi and H. Takeshita. Do human fetuses anticipate self-oriented actions? a study by four-dimensional (4d) ultrasonography. *Infancy*, 10(3):289–301, 2006.

E. Partridge, M. Davey, M. Hornick, P. McGovern, A. Mejaddam, J. Vrecenak, C. Burgos, A. Olive, R. Caskey, T. Weiland, J. Han, A. Schupper, J. Connelly, K. Dysart, J. Rychik, H. Hedrick, W. Peranteau, and A. Flake. An extra-uterine system to physiologically support the extreme premature lamb. *Nature Communications*, 8:15112, 05 2017.

V. Periyasamy and M. Pramanik. Advances in Monte Carlo Simulation for Light Propagation in Tissue. *IEEE Reviews in Biomedical Engineering*, PP, 08 2017.

V. M. Reid, K. Dunn, R. J. Young, J. Amu, T. Donovan, and N. Reissland. The Human Fetus Preferentially Engages with Face-like Visual Stimuli. *Current Biology*, 27:1825–1828, 03 2017.

Chapter 2

Background and Context

In this section, we provide background context for the mathematical modelling employed within this research. In addition, we outline several areas in which these techniques have been applied. The discussion of such applications serves to motivate the usage of such methods in our own research.

2.1 Historical and Theoretical Context

The term “Monte Carlo method” refers to a wide class of mathematical and computational techniques used to predict the outcomes of an uncertain event through generation of approximate results via repeated random sampling. More generally, the Monte Carlo (MC) method can be used to provide numerical solutions to problems involving the evolution over time of object-object interactions [Bielajew, 2013] — i.e., randomness can be used to approximate the outcomes of complex, but deterministic, aspects of a problem. Within an individual MC simulation, we follow the temporal evolution of a model whose changes follow a complex set of often intractable equations. Instead, the evolution proceeds in a stochastic manner dependent on random numbers generated during the simulation. If we were to repeat the process, our simulation results would likely differ individually from those of the first due to the random number generation; however, the agreement across the two simulations would fall within some “statistical error” [Landau and Binder, 2014], and the result will eventually converge as we continue to increase the sample size.

Famously, the supposed inspiration for the MC method occurred in the late 1940s, during a time when nuclear weapons projects required the investigation of neutron diffusion in fissionable material [Eckhardt, 1987]. Due to the complexities involved with this research, physicists made slow progress on analytical solutions despite having access to most of the required data. This issue remained a hindrance until the physicist Stanislaw Ulam began to consider (while recovering from an illness) several methods of determining the chances of successfully completing a game of solitaire. After attempting conventional calculations via combinatorics and finding little success, he instead proposed the possibility of playing one hundred games while counting the number of successful outcomes [Eckhardt, 1987]. This could then present an estimate of the overall likelihood of successful completion. With the growing usage of fast computers for research, Ulam noted the relative ease with which this method involving random experiments could be pursued and began to consider its extension to his own research problems around neutron diffusion. The name "Monte Carlo method" was consequently coined by Ulam's colleague, Nicholas Metropolis, in reference to the famous casino and its relevance to the randomness employed via the method [Metropolis, 1987].

Though the story of Ulam and his solitaire problem provides an interesting segue into the development of the modern MC method, the idea of using stochastic sampling methods to determine numerical solutions had been explored several times before the 1900s. Most prominently, Comte de Buffon [1777] posed the following problem: assuming a floor is made of parallel strips of equal width wood, if we drop a needle onto the floor, what is the probability that it lies across the boundary line between two strips? Comte de Buffon proposed a solution which involved a MC-like method where needles were repeatedly tossed onto the floor, with the needles crossing lines counted and then used to determine the probability of interest. A further early consideration of using random sampling methods to obtain numerical solutions was later made by Pierre-Simon Laplace, who suggested the implementation of a similar process to that of Comte de Buffon in order to determine the value of π [Laplace, 1886].

Regardless of when the first usage of the MC method occurred, its implementation in the laboratories of Los Alamos by Ulam and his colleagues — at a time when computers were emerging — led to an explosion of research utilising MC methods across the fields of physics, chemistry, and computing: Bielajew [2013] estimated that over 300,000 papers had been published utilising the method by 2011.

Mathematically, the MC method is simple. When a desired quantity is to be calculated, we first express it as the expectation of a random variable X — that is, $\mu = \mathbb{E}(X)$. Next, we generate from the distribution of X a predetermined number of independent and random values $X_1, X_2, \ldots, X_n$ and proceed to determine their average as our estimate of μ:

$$\mu \approx \hat{\mu}_n = \frac{1}{n} \sum_{i=1}^{n} X_i. \tag{2.1}$$

The complication with this simple approach arrives through the dependence of X on other variables — that is, $X = f(\boldsymbol{Y})$, where $\boldsymbol{Y}$ represents a vector of unknown constraints determining X. In this case, $\boldsymbol{Y} \in \mathcal{D} \subseteq \mathbb{R}^d$, with a probability density function (PDF), $p(\boldsymbol{y})$, that determines the likelihood of $\boldsymbol{Y}$ being within a given range. Consequently, in the case of X being dependent on other variables, our method for determination of the expectation becomes

$$\mu = \int_{\mathcal{D}} f(\boldsymbol{y}) p(\boldsymbol{y}) d\boldsymbol{y}. \tag{2.2}$$

It is important here to highlight how it does not necessarily matter what exact variable(s) or constraints that $\boldsymbol{Y}$ represents. Rather, so long as $X = f(\boldsymbol{Y})$ is a quantity that can be averaged, we can look to apply the MC method.

The justification for applying the Monte Carlo method can be seen through the law of large numbers. Specifically, if we take our random variable X as before (with an existing value for $\mu = \mathbb{E}(X)$) and again generate the independent and identically distributed values $X_1, X_2, \ldots, X_n$ with the same distribution as

X, we can see the following through applying the weak law of large numbers:

$$\lim_{n\to\infty} P(|\hat{\mu}_n - \mu| \leq \epsilon) = 1, \tag{2.3}$$

where $P(\dots)$ represents the probability of the argument occurring, and this holds for any value of ϵ greater than 0. In short, the probability of our estimated average, $\hat{\mu}_n$, missing the true average, μ, by more than ϵ tends to zero as we increase the sample size. Further, the strong law of large numbers says that

$$P\left(\lim_{n\to\infty} |\hat{\mu}_n - \mu| = 0\right) = 1. \tag{2.4}$$

In other words, the absolute difference between our estimated average and the actual average value will eventually become zero (and remain there) in the limit as the sample size approaches infinity.

2.2 Applications of the MC Method

As Bielajew [2013] notes, the MC method has been employed in many fields. A common application is seen in problems that involve the calculations of particle trajectories in a scattering medium. Within these problems, there are aspects that rely on variables with given probability distributions — consider, for example, how the speeds of gas particles obey a Maxwell-Boltzmann distribution [Maxwell, 1860]. It is at this point, when distributions become an important component of the problem, that MC methods clearly become a useful tool — that is, we can generate random values from these distributions for use in computing estimates for a variable's average.

As previously mentioned, perhaps the most famous usage of the MC method was also its first. The neutron diffusion problems being investigated in the laboratories of Los Alamos in the 1940s involved determining the distribution of neutrons in space and time as a function of the geometrical configuration and of the medium's physical properties. Within the medium in which these nuclear particles exist, there is the possibility for the particles to undergo absorption, scattering, or fission (in which case further nuclear particles are produced). In order to determine the behaviour of this system, one might consider finding solutions via analytical methods with the Boltzmann equations; however, these “classical methods” are frequently laborious due to the high dimensionality with three space components and three velocity components [Metropolis and Ulam, 1949]. Thus, the MC approach was employed to avoid dealing with the multiple integrations and probability matrix computations involved with the relevant integro-differential equations.

In using the MC method in such instances, one instead considers single chains of events beginning with individual particles and following their progeny [von Neumann and Richtmyer, 1947]. These chains of events may, in a sense, also be viewed as Markov chains — that is, conditional on the current state of the system, the chains’ previous and future states are (practically) independent. Interestingly, the Markov Chain Monte Carlo method was consequently introduced by Metropolis et al. [1953]. Within the chains of events, trajectories are calculated through equations of motion and by taking appropriate random variables at certain points to represent the occurrences of processes such as scattering or fission. Following a single particle through its “walk” then provides a sample of a chain reaction within the system. Subsequent generation of many such walks then allows for the calculation of average results for quantities of interest, alongside the development of a macroscopic picture of the distribution of neutrons within the medium. Due to the relative ease of mechanically coding this iterative process into computers (both of the time and now), the MC method was crucial in the development of neutron transport research at Los Alamos and within the fields of atomic and nuclear physics.

As a more contemporary example demonstrating the extent of MC method usage, in the field of heliophysics, research often involves exploring the interaction between the sun’s outward-flowing solar wind and the inward-flowing local interstellar plasma. Again, this is a situation that involves considering trajectories of particles within a scattering medium, with statistical functions governing distributions of variables such as particle speeds (for instance). As opposed to following a continuum approach to exploring this interaction, Baranov and Malama [1993] introduced a model of neutral hydrogen in the heliosphere that used a Monte Carlo approach to simulate the trajectories of hydrogen atoms. This built on the earlier proposition by Malama [1991] for a MC scheme which would simulate the penetration of neutral interstellar atoms into the solar system. Further work within the field continues to make use of MC methods. For example, see Heerikhuisen et al. [2006], who present a comparison between MC and multi-fluid approaches to modelling interactions between interstellar hydrogen atoms and the solar wind.

Much usage of MC methods has occurred within the fields of medicine — it is estimated that roughly 10% of all papers employing MC relate to medicine [Bielajew, 2013]. There are several reviews that discuss the application of MC methods to medical physics (see Bielajew [2013] for an example); however, a common theme is to acknowledge the work of Berger [1963] in providing a foundational framework for MC electron and photon transport (and their consequent medical applications). This paper was of paramount importance for the application of MC methods to problems in medical physics, especially, due to the rapid development of technologies and procedures employing radiation treatment. Within these treatments, energetic photons or charged particles are used to penetrate tissue and cause DNA damage to cancerous cells (as in radiation therapy, for example). Once more, this is a situation where the trajectories of particles in a scattering (and absorbing) medium require calculation with consideration of statistical processes such as the distribution of scattering angles. Further, due to the nature of the involved applications, there are high demands for accuracy of these treatments (across tissues that differ in composition and density, and across varying radiation doses, measurements, and instruments). As a result, MC methods currently provide the only way of computing predictions of the required quantities that meet the required levels of accuracy [Bielajew, 2013].

Following our discussion of the applications of MC methods to medical physics, an evidently clear area of focus is that of tissue optics — the transport of photons through a tissue medium. There exists a broad array of research undertaken already within this area in its relatively short history, and a focal point of investigation has been into the specific simulation of (and development of models for) photon transmission through human tissue. This subset of research falls within the wider field of computational biomedical optics, and it is within this broad field that the work of this Ph.D. is primarily focused. Further, the employment of MC methods is paramount to modelling the trajectories of photons in tissue, and it is from here that this thesis will continue its literature review in the following section.

2.3 Before MC Modelling

Before the common use of MC models in this field, analytic approaches focused heavily on using the transport equation [Keijzer et al., 1989]. Also known as the Boltzmann equation in statistical mechanics, when applied to the propagation of light, the transport equation is frequently referred to as the equation of (radiative) transfer (see Chandrasekhar [1960] for background theory). Despite the evident appeal to having a central governing equation underlying the involved physical processes for tissue optics, such equation-based approaches are increasingly limited in contemporary research. Mostly, this is due to the common case that analytical solutions are not available for situations which may be of physical interest in tissue optics [Welch and van Gemert, 2011]. For instance, Keijzer et al. [1989] note that, although the equation of transfer has been solved for a 1-D geometry, solutions for 2-D or 3-D geometry require the angular distribution of scattered light to be severely restricted. These limitations are in the same vein as those mentioned for solving the neutron diffusion problems analytically in Section 2.2. Indeed, it is partly due to the fact that there are no general solutions to these transport equations for tissue that the field has been forced to look to alternative methods.

A useful distinction employed in some applications of transport theory involves separating problems into three distinct regimes based on the volume density of scattering particles [Wang and Wu, 2007]. Consequently, it can be shown — for dense mediums such as soft tissue at optical wavelengths — that the equation of transfer is able to be simplified to what is known as the diffusive theory approximation [Welch and van Gemert, 1995]. By assuming the propagation of light to be a diffusive process, this approximation can assist with finding reasonable solutions in situations where analytical solutions for the equation of transfer are not available [Welch and van Gemert, 2011].

Thus, prior to the introduction of MC modelling for tissue optics, applying the diffusion approximation and solving the resultant diffusion equations by analytic or numerical means was a productive method of research. For instance, Kubelka [1948] derived the Kubelka-Munk system of differential equations which model the diffuse transmittance and reflectance of plane tissue layers. Further, via the same assumption of diffuse light, Kubelka [1954] extended the model to incorporate nonhomogeneous layers (where the scattering and absorption coefficients varied with distance from the surface). More recently, applications of the diffusive approximation have made use of theoretical equations (such as Kubelka-Munk) in comparison to empirical measurements of photon transport. For instance, Wan et al. [1981] measured *in vitro* human tissue transmittance and compared this to predictions from diffusion theory with reasonable success. Similarly, Flock et al. [1989] found results for several variables from diffusion theory models to hold reasonable agreement with those previously found empirically.

Although the diffusion approximation can provide results in decent (strong, even) agreement with those found empirically, it has several limitations. Perhaps primarily, its validity in tissue is limited to situations where the light has been highly scattered [Welch and van Gemert, 2011] or the probability of scattering events is much greater than that of absorption events [Duderstadt and Hamilton, 1976]. Hence, for example, tissues with high absorption (e.g., high levels of melanin) and low scattering coefficients would not be modelled as accurately as the reverse case via the diffusion approximation. As a result, the diffusion approximation begins to break down for the case where there is high significance for absorption alone or as well as scattering processes — as can be the case for tissue, though Flock et al. [1989] note that mammalian tissues often satisfy the relative probabilities condition in the red and near infrared regions of the spectrum.

Similarly, though the diffusion theory approximation can provide valid results and predictions far from the boundaries of a tissue region, its validity near the boundaries is dependent on the formulation of the boundary conditions; however, it is not usually the case for this approximation that these boundary conditions can be fulfilled — i.e., diffusion theory is not valid near the boundary [Duderstadt and Hamilton, 1976]. An example of this can be seen in the work of Flock et al. [1989], who found that the diffusion approximation's results fell away in terms of accuracy near the boundary (especially in comparison to those of the MC model).

Further, the diffusion theory approximation can fail when photon path lengths are too small (see Graaff et al. [1993]), it performs poorly when modelling the upper regions of tissue where an incident laser beam primarily diffuses (see Keijzer et al. [1989]), and — similar to analytic methods — there are wavelength ranges where the approximation fails to provide reliable results (see Patterson et al. [2005a] and Patterson et al. [2005b]). Consequently, modelling research within tissue optics has moved towards what is referred to as the "gold standard" [Periyasamy and Pramanik, 2017]: MC simulation. This progression will be discussed further in the next section.

From an experimental perspective, prior to the introduction of MC methods to tissue optics, investigations into the propagation of light through tissue had largely been limited to *in vitro* studies (with no *in vivo* systematic research conducted). Much of the earlier *in vitro* research focused on the transmission of skin tissue, such as the work of Hardy et al. [1956] who noted that attenuation due to absorption and photon scattering at infrared wavelengths could be combined into a single exponential form (a related theoretical idea used in simulations is the Beer-Lambert Law, discussed in Section 3.3.1). This property did not extend to the visible light range, however, which was proposed to be due to inhomogeneities of skin samples (e.g., melanin pigmentation) at increasing depths.

In contrast, *in vivo* studies are still relatively limited in tissue optics since the advent of MC methods. Consequently, optical properties for these cases are still being measured, though technological improvements over the past three decades are allowing for rapid progress. For a review of the advancements made in this area, see (for example) Sandell and Zhu [2011]; however, this literature review shall not further address how the optical properties of tissue are derived.

As discussed in Section 2.2, researchers had already begun to widely apply MC simulation methods to radiation transport studies prior to the mid-1950s [Profio, 1979]. Despite the early forays of radiation transport researchers into MC modelling (see Raeside [1976], for instance), efforts to bring MC methods to tissue optics did not begin until at least the early 1980s.

2.4 Early Computational Developments

Computer simulation of photon propagation through biological tissue via the MC method was first conducted by Wilson and Adam [1983]. In this work, a computational model was developed to simulate the propagation of light through homogeneous tissue under different absorption and scattering ratios. Specifically, light attenuation was assumed to result from a combination of absorption and isotropic scattering, the latter of which allowed a much-simplified model alongside the assumed homogeneity of tissue. The isotropic scattering incorporated by Wilson and Adam [1983] was identified as a limitation, due to the recognition of tissue as being highly forward-scattering [Jacques and Prahl, 1987] — i.e., most scattering events in tissue result in photons scattering with an angle of less than 90 degrees from their initial propagation direction. Hence, future modifications to the model would eventually involve the extension to anisotropic photon scattering, where the proportions of forward- and back-scatter at collision events (through the scattering angle) could be adjusted accordingly based on medium-specific parameters.

Subsequently, in measuring the radiant intensity of laser light scattering (as a function of angle) for human tissue, Jacques et al. [1987] demonstrated that the data could be well-described by an analytic expression known as the Henyey-Greenstein (H-G) function. Initially used to describe the scattering of light by clouds of interstellar dust [Henyey and Greenstein, 1941], the H-G function allows variation from back-scattering through isotropic scattering to forward-scattering by the adjustment of a single parameter: the anisotropy, g, which measures the level of forward direction conserved after each scattering event. Typically, the value of g in biological tissue is $\sim$0.9, indicating that it is highly forward-scattering [Tuchin, 2007]. As it allows this variation of scattering with relative ease, the subsequent incorporation of anisotropic scattering via the H-G function was introduced to MC simulation of photon propagation in biological tissue by Keijzer et al. [1989]. Later programs employed in the literature have continued to follow this method of anisotropic scattering until the present day. For a more theoretical discussion of the anisotropy parameter and the H-G function, see Sections 3.1.3 and 3.5.2.

In addition, the model of Keijzer et al. [1989] introduced a common nomenclature used in structuring photon transport programs [Jacques and Wang, 1995]:

- "Hop", where the photon (or, more commonly, photon packet with predesignated weight) takes a step along its trajectory,
- "Drop", describing the photon interacting with the tissue at its new position in a manner that involves a portion of the packet's weight being

absorbed, and

- "Spin", which is where the photon is scattered into a new direction according to a chosen scattering function (commonly, the H-G function).

Until the late-1980s, MC modelling of photon transport in biological tissue described photon spatial positions via cylindrical coordinates (Figure 2.1), with direction of travel further being described by the direction angles θ, ϕ (see Wilson and Adam [1983] and Keijzer et al. [1989]). In part, this was due to the ability to employ axial symmetry in the coordinate systems to lessen computational load. A distinct disadvantage of this method, however, was the need for repeated calls to computationally expensive trigonometric functions to determine direction and spatial location at each propagation step during simulations. Hence, it is convenient to instead utilise direction cosines, which reduce the number of calculations required and do not change along "Hops" (but will change at scattering events) [Carter and Cashwell, 1975]. This procedure is discussed more in Section 3.2. In addition, changing to Cartesian coordinates to represent the spatial location of the photon aids simplicity of the program and results in the direction of propagation being uniquely specified with respect to the Cartesian axes. These changes were incorporated by Prahl et al. [1989], alongside a presentation of validation benchmarks and an analysis of methods to improve MC method efficiency.

2.5 MCML and the Investigation of Layers

Work prior to the 1990s involved simulating the propagation of photons through one layer of skin, with consideration given to interactions between the photons and tissue-air interfaces (e.g., when photons exit the medium); however, no programming emphasis was placed on modelling the propagation of photons with multiple tissue-tissue boundaries incorporated. For example, see Keijzer et al. [1989], where subsequent MC simulation of tissue inhomogeneities and layered structures is briefly mentioned as a future possibility. Skin has long

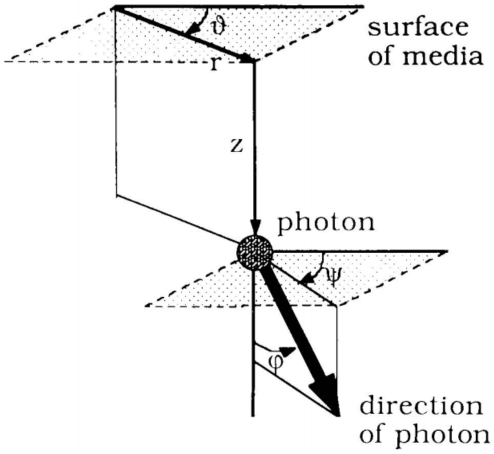

Figure 2.1: A diagram displaying the cylindrical coordinate system employed in early models. Image credit: Keijzer et al. [1989].

been known to be a complex arrangement of tissue structures and vessels, roughly divided into three distinct layers: the epidermis, dermis, and subcutaneous fat layer (see Figure 2.2). Hence, an obvious extension to the standard MC models used in the field at this time involved the consideration of tissues with multiple optically different planar layers.

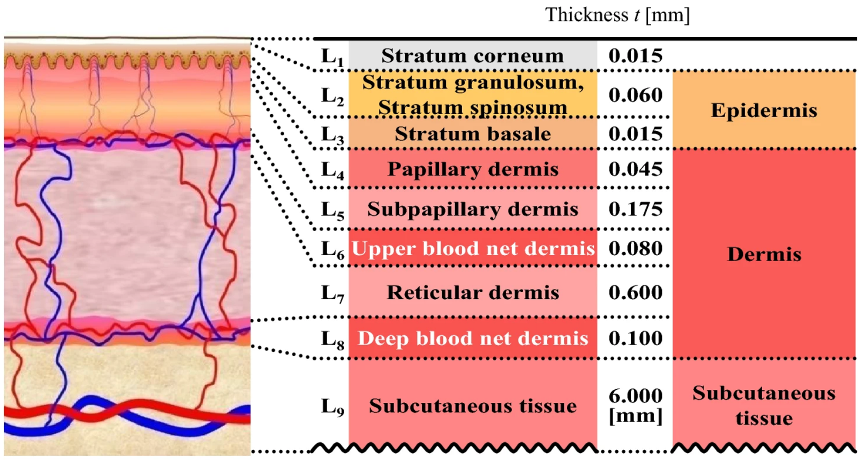

(a) Cross section of skin **(b)** Nine-layered skin model **(c)** Three-layered skin model

Figure 2.2: **(a)** Schematic illustration of skin tissue with complicated structuring, **(b)** nine-layer skin tissue model with layer names and thicknesses, and **(c)** common three-layer tissue model. Image credit: Das et al. [2020].

The addition of multiple tissue layers to the standard form of the MC modelling structure was first discussed and employed by Wang et al. [1995]. In this seminal work, the authors formally introduced the Monte Carlo Multi-Layered (MCML) program, which allows for multiple planar layers of tissue (see Figure 2.3) and permits the user to identify different optical properties and thicknesses for each layer without re-compiling the program for each specification.

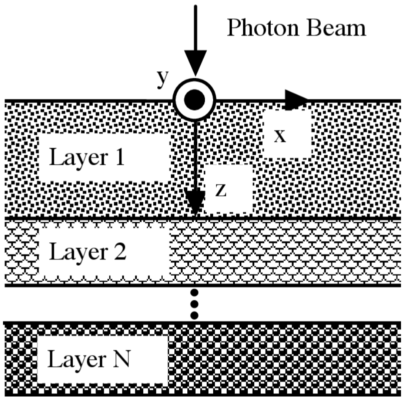

Figure 2.3: A visualisation of the coordinate system utilised for MCML. Each layer is distinct and consists of infinitely wide (x, y) tissue. Note that, due to the 2D representation of a 3D environment, the y-axis points out of the page here. Image credit: Wang et al. [1995].

The steps employed by MCML are logical and simple to follow (see Figure 2.4), which is a key reason for the subsequent popularity of both the program and algorithm. A more comprehensive description of the general photon propagation modelling process is given in Chapter 3; however, the MCML procedure is essentially as follows. At launch, an appropriate random number is generated to determine the “Hop” of the photon packet. This “Hop” (path length) is compared to the distance to the interface boundary in the photon’s direction of trajectory. If the photon is going to hit the boundary, it is moved to the intersection point and determination of transmission or reflection is completed via comparison of random numbers with calculated probabilities before finalising any remaining trajectory in the appropriate (reflected or transmitted) direction. If the photon is not going to hit the boundary, it moves to its new location, undergoes any attenuation due to absorption, and scatters appropriately. This process is repeated with a given individual photon packet until it exits the medium entirely or its weight diminishes below a preset threshold. The routine then repeats until all packets have been simulated.

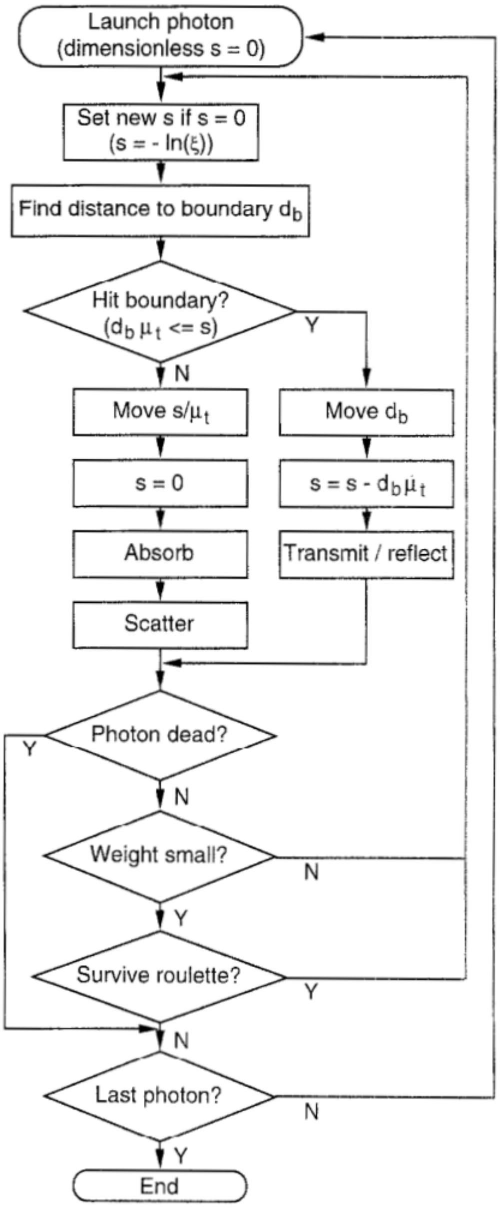

Figure 2.4: A basic flowchart describing the method for the simulation of photon trajectories in MCML. Image credit: Wang et al. [1995].

MCML has since been widely distributed via the internet (see, for instance, Prahl [2017]) and is commonly used as a base to build from when solving various problems. As an example, Jacques [1998] used a simplified version of MCML to provide analytic expressions that replicate MC simulations for light distributions in biological tissue from plane, line, and point sources in planar, cylindrical, and spherical coordinates. Further, Jacques [1998] compared the results of their MC simulations with diffusion theory expressions and found that the latter poorly predicted the values for fluence rates (though the shapes of fluence rate distributions were accurate).

The introduction of MCML enabled many investigations involving various numbers of tissue layers in the model beyond the previous single-layer standard. For example, in estimating the melanin concentration and blood and oxygen saturation levels of human tissue, Nishidate et al. [2004] considered the skin as consisting of two layers: the epidermis and the dermis, thus omitting the stratum corneum and subcutaneous tissue from Figure 2.2b. Other studies consider three-layer models, such as Nasouri et al. [2014], which models the subcutaneous tissue in addition to the epidermis and dermis (i.e., Figure 2.2c).

Further research has investigated the use of models with varying numbers of layers and their outputs as a means to determine the errors made with *in vitro* experimental measurements, such as the work of Nishidate et al. [2003]. In this paper, a two-layer experiment consisting of the epidermis and dermis is run for visible light alongside a four-layer experiment which separates the dermis into an upper and lower layer, with a blood layer running between to represent structures such as veins, tumours, or internal bleeding. This adjacent setup is run for near-infrared light wavelengths. A framework such as this allows for parameters (such as absorption coefficients) to be experimentally determined via the two-layer measurements before consequently estimating haemoglobin concentration and oxygen saturation of the blood layer via the four-layer experiment and comparing to those determined via MC simulation. Subsequent research has expanded upon this usage of adjacent tissues with varying layer numbers. Nishidate et al. [2005] proposed the method as useful for visualising the depth distribution of local blood layers in tissue, which has applications in laser light treatment of issues such as tumours and internal bleeding. Further usage of this method then enabled visualisation of the thickness distribution of the local blood region in addition to the depth distribution [Nishidate et al., 2007], which again has clear applications in biomedical optics.

Investigations into multiple layers of tissue in the model extend to incorporating all nine regions shown in Figure 2.2b. Recent studies such as that of Maeda et al. [2010], who investigated MC simulation of spectral reflectance, and Das et al. [2020], who constructed a skin reflectance spectral database, make use of nine-layer models in their simulations. Specifically, Maeda et al. [2010] make the extension after noting that earlier studies utilising two- or three-layer models assume homogeneous distributions of chromophores (molecules which absorb light at particular wavelengths) over the layers simulating the epidermis and dermis. This means the models are incapable of accounting for chromophore localization, which has implications for the utilised optical properties and consequent behaviour of simulated photons. In addition, Maeda et al. [2010] reference sequential earlier studies whose models include seven layers for the skin tissue (see Meglinski and Matcher [2002] and Meglinski and Matcher [2003]). These studies employ the nine layers identified in Figure 2.2b, with L2 and L3 merged together and L4 merged with L5. Maeda et al. [2010] identify limitations of this seven-layer model surrounding the assumption of zero wavelength-dependence for the scattering coefficient and anisotropy parameter, alongside the implicitly assumed homogeneity of the epidermis and upper dermis layers. These limitations are altered in the nine-layer model by the inclusion of further layers and the addition of wavelength-dependence to the mentioned parameters.

As might be expected, across the literature, the general consensus for the inclusion of more layers to the model is that simulations show improved correspondence to those obtained by direct measurement (both *in vivo* and *in vitro*) when further layers are incorporated. A common theme is the acknowledged ability for increased layers to more accurately model skin tissue inhomogeneities in the z-direction — i.e., variations between the layers. For example, Das et al. [2020] reference the histological classification involved in the development of their nine-layer model; the existence of fibre components in the dermis such as collagen and elastin relate to the tissue's scattering properties, while melanin and haemoglobin in the epidermis and dermis (respectively) relate closely to the absorption properties of skin. Levels of these components in skin tissue vary with depth and specific layer, so the incorporation of a nine-layer structure provides increased capability for realism in the model beyond the traditional three-layer simulations employed in the late 1990s and early 2000s.

The cost involved with expanding models and layer numbers is lost efficiency. Although the previously outlined examples may improve accuracy and realism, models with fewer layers are easier to build and implement, as well as requiring less computational resources to run simulations. This relative efficiency allowed quantitative results to be reasonably produced in the early years of this field. The consequent advent of programs such as MCML [Wang et al., 1995] to build from, and the ready availability of increased computational power in the modern day, has allowed wider implementation of additional layers. This, in turn, has resulted in simulations that are more precise in nature, due to increased accuracy in modelling finer details within the tissue.

2.6 Beyond MCML

Though MCML is widely used for MC simulation of photon propagation in tissue, its main feature is also its primary drawback: its standard geometry allows only planar layers of tissue. That is, each layer is infinitely wide in the x- and y-directions (see Figure 2.3). As such, MCML is not readily appropriate for modelling photon propagation through mediums that are not consistent of planar layers of tissue, nor can it readily model photon propagation through layers with individual inhomogeneities (each layer being infinitely wide implicitly requires each tissue layer to be homogeneous across its lateral dimensions).

Early methods of countering these limitations included studies which independently investigated the modelling of port-wine stain birthmarks via models consisting of infinite epidermis and dermis layers, with infinitely long cylinders embedded within the dermis to represent enlarged capillaries (see, for example Smithies and Butler [1995] and Lucassen et al. [1996]). Further similar research has embedded cuboidal [Zhu and Liu, 2012] and spherical objects [Wang et al., 1997] within the tissue to simulate the presence of tumours. Note that these methods of embedding objects within layers differ slightly to the models employed by, for instance, Nishidate et al. [2003], who simply introduce an additional infinitely wide layer within the model.

Several recent studies have also built on the baseline MCML program to more easily model multi-layered tissue with various embedded objects of rudimentary geometries, such as spheres, cylinders, ellipsoids, or cubes. As an example, MCML with embedded objects (MCML-EO) was developed by Periyasamy and Pramanik [2014] to model these situations, building off the aforementioned earlier work on modelling embedded objects. There have been several further significant computational developments within the field of tissue optics that follow similar veins to that of MCML. The most prominent contemporary examples of these are MOSE, TIM-OS, and MMCM — each of which will be briefly outlined in the following discussion.

2.6.1 MOSE

A simple solution to the primary hindrance in the MCML model is to break each planar region into pieces. Doing this allows for inhomogeneities across the lateral dimensions of the tissue to be accounted for and represented within the simulation. This type of model is referred to as a voxelated tissue model (voxel being a volume pixel) and is a common developmental direction within the field since the introduction of MCML. One of the earliest usages of this voxel-based MC approach was that of Pfefer et al. [1996], who utilised cubic voxels within modular adaptable grids to simulate the propagation of light through various geometric shapes (as well as models derived from images of rat skin). See Figure 2.5 for a visualization of the environment. Results from this work found good agreement with previously published data, both quantitatively and qualitatively [Pfefer et al., 1996].

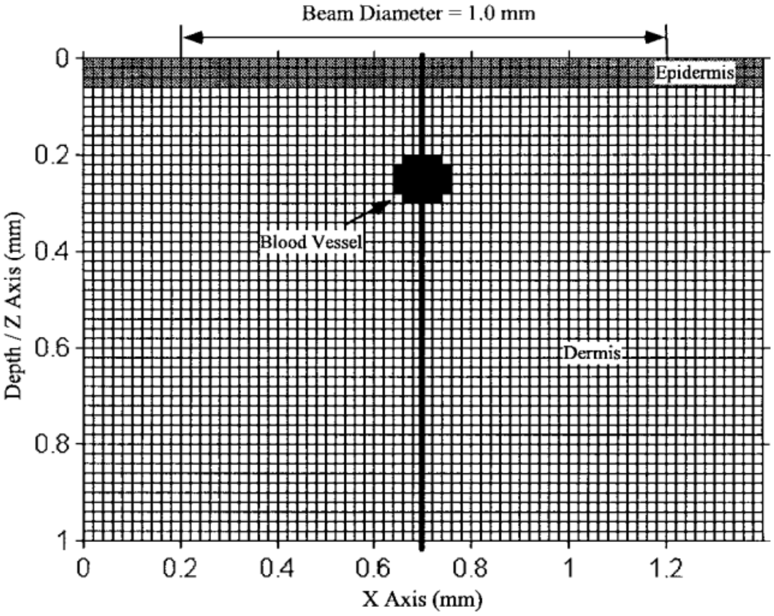

Figure 2.5: An xz-plane cross-section of the cubic voxel model. Note that there are two layers presented: the epidermis and the dermis. Each layer is divided into cubes. Additionally, a blood vessel is simulated via voxels. The bold line running vertically through the centre can be ignored here. Image credit: Pfefer et al. [1996].

The usage of cubic voxels was extended by a prominent model known as tMCimg [Boas et al., 2002], which takes on 3-D structural data obtained via MRI or CT scans to produce a voxel-based model through which photons can propagate. This allows the modelling of photon migration through arbitrary complex tissue structures, though an apparent limitation is that it requires external data of the involved geometries. Further work completed by Patwardhan et al. [2005] extended the voxelated tissue approach to incorporate a voxel library, which allowed the researchers to independently alter the physical and optical properties of individual voxels to model complex tissues such as skin lesions across different mediums and wavelengths. Figure 2.6 presents a flowchart explaining the algorithm employed within the outlined voxel models.

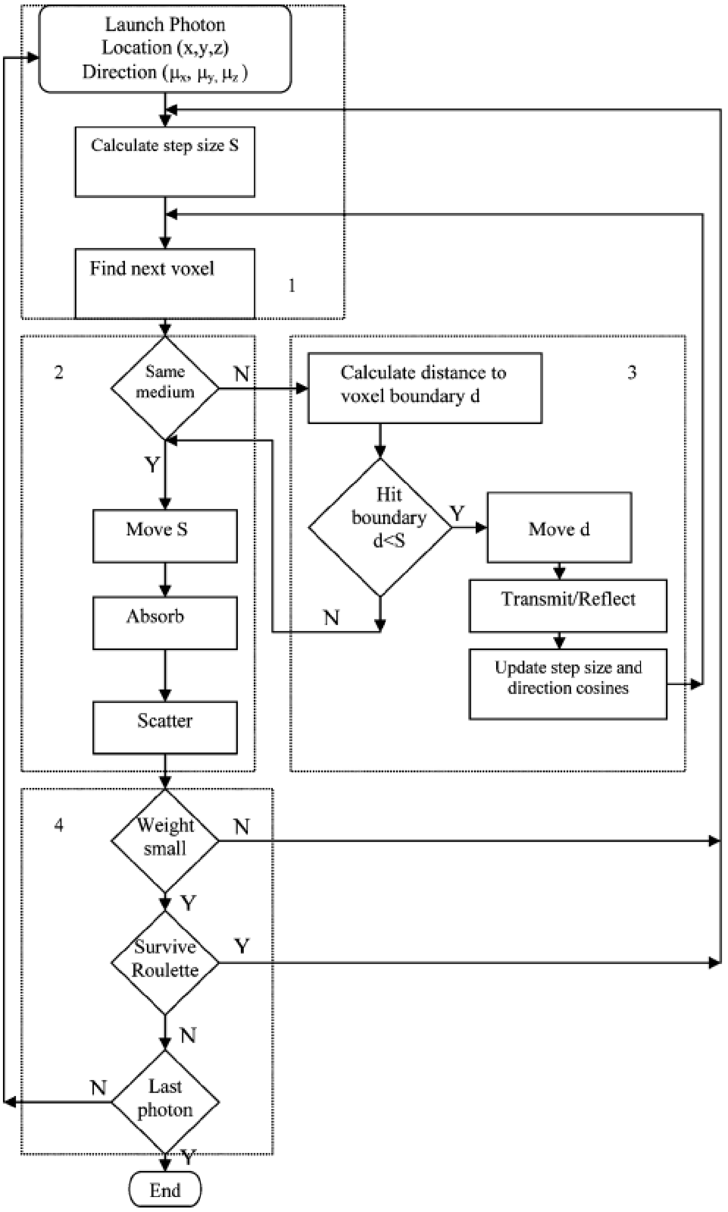

Figure 2.6: A basic flowchart describing the method for the simulation of photon trajectories employed in voxelated tissue models. Note this is similar to Figure 2.4, though there is an additional check required for inter-voxel boundaries. Image credit: Patwardhan et al. [2005].

Clearly, a limiting factor with cubic voxels is the relative difficulty involved in using them to model curved surfaces and boundaries. The inability to include precise boundary information (e.g., normal vectors) leads to the potential introduction of errors. Some can be avoided by increasing the resolution of the grid (i.e., increasing grid density by reducing voxel size); however, the associated cost is the requirement of more computational power and memory. One way to avoid this problem and incorporate curved surfaces and boundaries is to instead use "building blocks" such as cylinders, ellipsoids, and polyhedrons, which was the approach taken by Li et al. [2004] in developing their mouse optical simulation environment (MOSE) to model light transport through a living mouse. This program was built in a manner aimed at modelling small animals, though it was later extended to the more general use case of the *molecular* optical simulation environment (also MOSE) by Ren et al. [2013]. For reference, the flowchart describing the MOSE programs is effectively the same as that of Figure 2.6. A two-dimensional tissue structure demonstrating the regime incorporated in MOSE is shown in Figure 2.7.

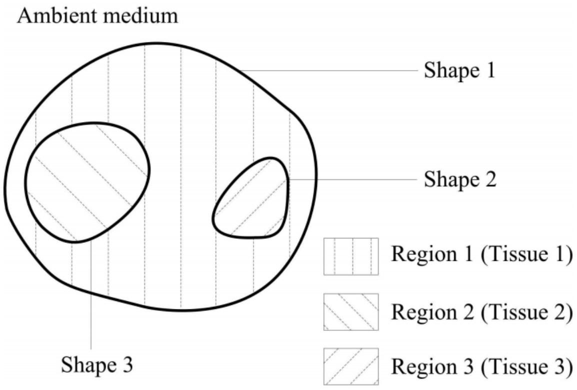

Figure 2.7: A simple two-dimensional example of the tissue structure incorporated by MOSE. Here, Tissue 1 is outermost, with its exterior boundary (Shape 1) separating the tissue from the ambient medium. Similarly, Shapes 2 and 3 define the boundaries separating the internal Tissues 2 and 3 from Tissue 1. Image credit: Ren et al. [2010].

Evidently, the lateral inhomogeneities problems encountered by MCML were able to be alleviated with these voxel-type programs; however, although the inclusion of further geometric shapes as building blocks assisted with curved boundaries, a primary issue with the original MOSE program remained: many structures in biology are not easily defined by these standard shapes.

Consequently, mathematical models were developed to incorporate a surface-based mesh to accurately define tissue boundaries in the simulations. Early examples include those of Côté and Vitkin [2005] and Margallo-Balbás and French [2007], both of which use triangle-based surface meshes to more accurately approximate the (curved) interfaces. These are similar in nature to those used in computer graphics — hence, normal vectors are easier to define. More recently, the molecular version of MOSE also implemented the same approach [Ren et al., 2013]. An example of this type of surface mesh setup can be seen in Figure 2.8.

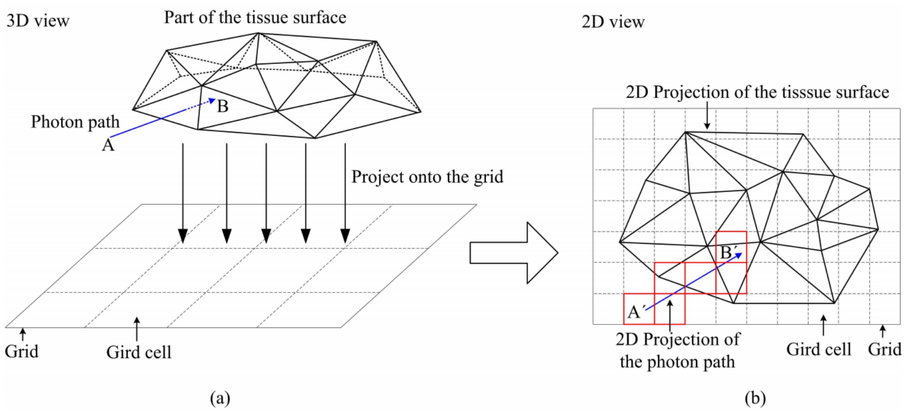

Figure 2.8: In (a), we see a three-dimensional view showing part of the tissue surface modelled by MOSE with a triangle-based surface mesh. In determining the intersection of the photon path and the tissue surface, the mesh is projected onto a two-dimensional grid. This is shown in (b). Similarly, the photon's path is projected onto the grid. The algorithm then involves checking which triangle meshes are allocated to each grid cell crossed by the projected photon path. In this manner, the triangle surfaces to be checked for intersections are reduced to only those whose two-dimensional projections overlap the grid cells crossed by the photon's path projection. Image credit: Ren et al. [2010].

Problems with these surface mesh-based approaches, though, involved difficulties in modelling media with continuously varying optical properties, and also the large number of triangles needing to be scanned when determining intersections of photons with surfaces (again, see Figure 2.8 for a brief outline of the algorithm). The latter issue leads to high requirements for computational resources and resultant increased processing times. Hence, several adjustments have been made to counteract this inefficiency, including the usage of GPUs in MC simulation. One of the first usages of GPUs in simulating photon propagation through any material was by Alerstam et al. [2008], while the first extension of GPU implementation to three-dimensional complex photon propagation simulations in tissue was performed by Fang and Boas [2009]. As a further example, see Ren et al. [2010] for an application related to this discussion.

2.6.2 TIM-OS

There are at least two ways to look at resolving the computational and parameter continuity issues that remained with the previously discussed surface-based mesh models. First, one could modify the manner in which the model incorporates surfaces and tissue regions. Second, one could improve the algorithm involved with performing the calculations required to determine the locations of ray-surface interactions. Two prominent recent models which each follow one of these distinct paths were reported in 2010.

Firstly, Shen and Wang [2010] modified the way surfaces and tissue regions were modelled by introducing a novel method based on a (somewhat) blended voxel/mesh scheme known as tetrahedron-based inhomogeneous Monte Carlo optical simulation (TIM-OS). The algorithm employed by TIM-OS is presented in Figure 2.9. Essentially, this model utilizes tetrahedrons (shapes with four triangular faces) as voxels to build the tissue. This improves the flexibility promoted by the earlier (rigid) voxel schemes, while also incorporating the ease of modelling curved surfaces introduced by mesh-based schemes. The key aspect which allows this method to be more computationally efficient than its predecessors lies in the reduction of the number of calculations required for photon-surface interactions. Specifically, the mean free path of a photon is usually smaller than the size of the tetrahedrons [Shen and Wang, 2010],

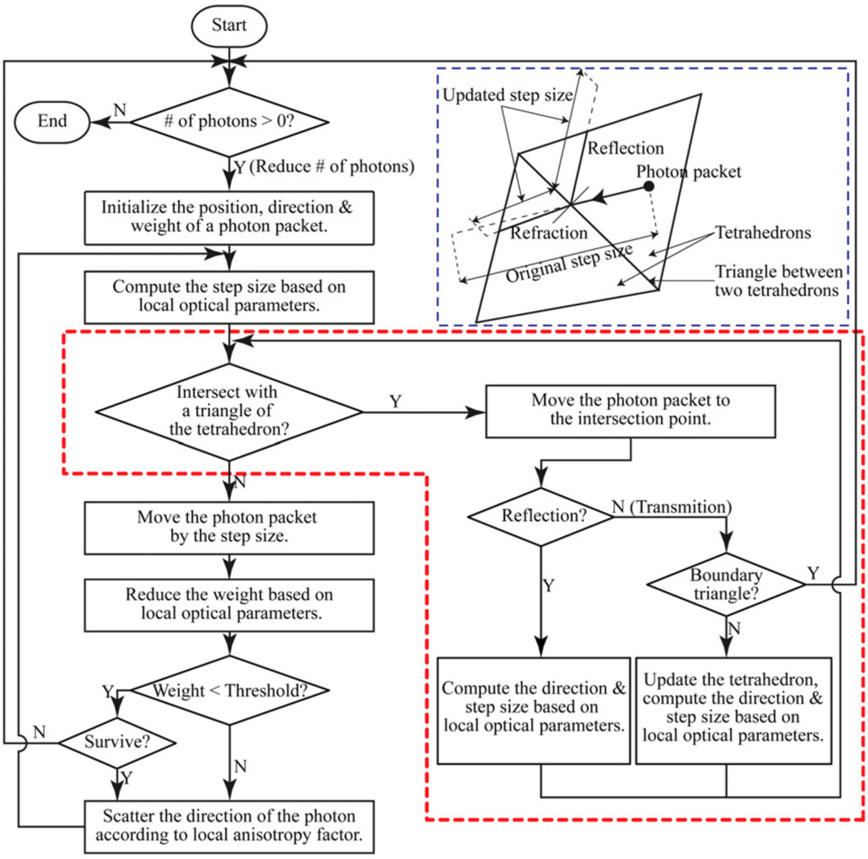

Figure 2.9: A basic flowchart describing the algorithm employed by the TIM-OS scheme. In red, the primary difference between this model and others (such as MCML) is detailed. This section explains the logic involved when a photon packet intersects a tetrahedron's surface. In blue, the photon-triangle interaction is detailed. Essentially, when a photon intersects a tetrahedron's surface, the updated step size and direction is determined after establishing reflection or transmission. The photon then continues along its new trajectory. Image credit: Shen and Wang [2010].

which results in most photon steps being made within the boundaries of the tetrahedron wherein the step began. Consequently, no surface interactions take place in these cases. On the occasions where a photon does happen to exit a tetrahedron, because the voxel only consists of four simple faces, there are only four possible surfaces with which the photon could interact. Hence, the necessary search space is heavily reduced, and this heavily decreases computational burdens when modelling.

2.6.3 MMCM

The second major recent model which addresses the aforementioned problems with surface-based mesh models is known as the mesh-based Monte Carlo method (MMCM). Introduced by Fang [2010], this method takes inspiration from works in computer graphics in order to improve the algorithm involved with determining ray-surface interactions (specifically, the authors cite Platis and Theoharis [2003]). In particular, the method implements a ray-tracing algorithm that utilises Plücker coordinates to represent surfaces and trajectories. In short, Plücker coordinates allow the specification of directed lines in three-dimensional space using vectors that are six-dimensional [Coxeter, 1957], with the particular benefit to this application being that the relative orientation of two rays can then be determined through their permuted inner product. The usage can be further extended to allow for computationally simple tests which check for (directional) ray-surface intersections. For further discussion of this application of Plücker coordinates, refer to (for example) Platis and Theoharis [2003]; however, a primary benefit of this coordinate system to Fang [2010] was that its simplicity allowed large improvements in computational efficiency. Because the ray-surface interactions could be determined through relatively simple calculations with Plücker coordinates, the checking process for whether a photon intersects any surface was largely improved.

In addition, Fang [2010] references the ability of their MMCM model to simulate continuously varying optical properties within regions of skin by interpolating properties defined on surface vertices. Hence, the MMCM model allowed further improvements to the field's existing modelling problems, as it also began to address the issues involved with modelling optical parameter continuities across tissue.

2.6.4 Preferred Methods

As a conclusion to our discussion of the computational developments within the field of tissue optics, we note that the diverse array of employed models and methods poses at least one further problem: is there a particular method that is more prominent or superior? There have been several comparisons and evaluations made in recent years (see, for example, Zhu and Liu [2013] or Wang et al. [2018]). A common conclusion is that TIM-OS performs simulations most efficiently in terms of speed, with MMCM a close runner-up. One drawback with these packages is the need for scripts to be written in order to run simulations — hence, their ease of use is somewhat low. Conversely, MOSE is user-friendly but limited in its applications due to its algorithm's low efficiency. Lastly, although MCML is an old package with limited initial usage, it is often recognised as particularly useful due to its ease of modification — many contemporary models use MCML as a foundation program and make additions to modify the package as necessary. Further, most models that use MC methods to simulate photon propagation through tissue employ algorithms that are heavily derivative of the original MCML algorithm. Consequently, in Chapter 3, our inspection of the base algorithm is akin to that of MCML and can be extended to most models in use within this field.

2.7 Research Focuses in Tissue Optics

Aside from the previously discussed specific computational developments made within tissue optics (and the highlighted associated investigations), there have been many further clear areas of research that have drawn focus over the field's history. In this section, we briefly highlight additional prominent areas with relevance to this project.

Evidently, determining the optical properties of tissue is a primary point of concern, as these properties not only define the propagation problem itself for light transport but also hold importance for applications of research such as this project. Generally, measurements of such properties are conducted experimentally before then being introduced to models as appropriate for further investigations and to cross-check against other research results. Both Cheong et al. [1990] and Jacques [2013] provide comprehensive summaries of these properties, their dependence on wavelength, and the experimental approaches used to determine their values.

MC modelling in tissue optics is often compared with diffusion theory (see Flock et al. [1989] or Jacques and Pogue [2008], for instance). As one might expect from the discussion in Section 2.3, there is often agreement between the models in most measures and regions; however, this agreement only extends insofar as the limitations of diffusion theory are not overly evident (for example, in regions close to boundaries). Some work has investigated the feasibility of hybrid models which combine the benefits of diffusion theory away from boundaries with those of MC close to boundaries (e.g., Flock et al. [1988]). This has the benefit of providing accurate results across all regions, while lessening computational load caused by applying the MC method in regions where the diffusion approximation may suffice [Hayashi et al., 2003]. This holds relevance to the present project, as it is an interesting means to increase computational efficiency and to introduce additional comparisons within future mathematical model outputs. With simulations that may run photon counts into the billions, any additional optimizations that can be made without sacrificing accuracy are important to consider.

On a similar computational efficiency note, there has been research into applying both condensed MC simulations [Graaff et al., 1993] and condensed history MC simulations (see Bhan and Spanier [2007] or Kawrakow [2000], for instance) to photon propagation in tissue. Though these ideas are different in practice, they hold similar conceptual goals — both aim to minimise computational work by generating accurate results from less calculations. Graaff et al. [1993] found success in extrapolating from the results of one MC simulation to obtain results such as reflectance and transmittance for other values of the albedo without having to redo the simulation. In contrast, Bhan and Spanier [2007] sought to reduce the number of individual interaction events experienced by a photon during its flight by way of compressing large numbers of minor interactions (where the actual impact to the photon's trajectory is often small) into smaller numbers of "super-events". A similar approach is applied in the diffusive regime (see Section 3.1.3.1), though these condensed MC methods are more flexible and applicable beyond the diffusion approximation's confines. Again, such optimizing techniques are important to consider for this model.

2.8 Applications to Illumination of the Uterus

The specific application of MC methods to the propagation of light through the uterus and to the fetus is a somewhat novel research area in terms of the existing literature. In this section, we discuss the (brief) literature in existence with direct relevance to the work presented in Chapters 5, 7, and 9 of this thesis. As it is beyond the scope of this review, we will make only minor reference to the existing literature in the wider fields of the developmental sciences.

One early attempt at modelling the transmission of light to the human fetus was that of Del Giudice [2011]. In this paper, the author combined experimental and modelling approaches to gain an approximate qualitative model of the amount of illuminance reaching the uterine cavity in comparison to external illuminance. The transmission coefficients for various samples of avian tissue and clothing were determined by first physically measuring the illuminance present with and without the samples above a light source. Next, multiple linear regression methods were used to determine a regression equation for the abdominal wall. The approaches employed and results generated were similar to those previously determined by Fulford et al. [2003] and Jacques et al. [2008], respectively, though the latter used rats and guinea pigs before proposing an extension to the human fetus. In addition, Fulford et al. [2003] focused primarily on using the results to measure fetal brain activity in response to visual stimuli.

There are several clear limitations to the work of Del Giudice [2011], aside from the fact that the work was intended to be qualitative. First, the model assumes uniformity in the tissue. In reality, there is (for instance) variation in tissue density around the uterus which should be considered. Further, the model does not consider any effect due to amniotic fluid — clearly, there would be some impact to light transmission from this presence. Building on the assumption of tissue uniformity, the model additionally is only able to provide an estimate for light-coloured skin, and there is no means to incorporate any depth-related inhomogeneity in estimates. Evidently, there are many more points which could be made that indicate further development being required for this model; however, the key claim made by Del Giudice [2011] is that reasonable luminance might be expected within the uterus for relatively low levels of exterior lighting.

Citing the results of Del Giudice [2011], subsequent work by Reid et al. [2017] then presented diode light sources to the fetus by way of illumination of the maternal abdomen. Reid et al. [2017] concluded through use of equations from Jacques [2013] that the stimuli presented would appear as shown in Figure 2.10. Note that this study did not explicitly incorporate any mathematical modelling in determining the light predicted to be presented to the fetus.

The work of Reid et al. [2017] was later questioned by Scheel et al. [2018], who noted that the light predicted to be presented to the fetus was likely incorrect due to an erroneous implicit assumption made in determining the appearance. Specifically, Reid et al. [2017] only accounted for light scattering once en route to the fetus — their prediction assumed only a simple, singular scattering at the interface between air and maternal tissue. In reality, the propagation of light through the tissue and amniotic fluid would consist of many such interaction events (scattering and absorption), resulting in a much

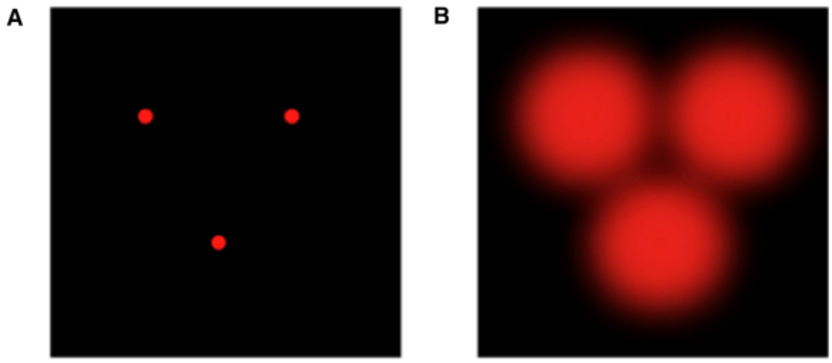

Figure 2.10: A conceptual illustration of one set of stimuli shone into the abdomen (left) and those calculated to be presented to the fetus (right). Image Credit: Reid et al. [2017].

further attenuated image being presented to the fetus than originally predicted by Reid et al. [2017]. Consequently, Scheel et al. [2018] predicted (via simple MC methods) the actual presentation to have been closer to Figure 2.11.

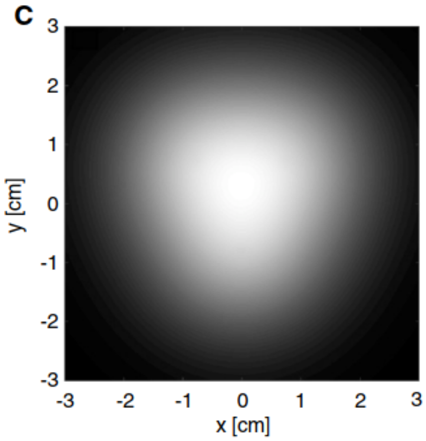

Figure 2.11: One estimated light pattern visible to the fetus, corresponding to the left stimuli in Figure 2.10. Image Credit: Scheel et al. [2018].

Hence, for the purposes of this literature review, we note that there has been an instance of MC modelling applied to similar situations as those initially explored within this thesis, insofar as there has been an estimate of how an external light source presents to the fetus; however, it was simplistic in execution due to its demonstrative intention. One evident limitation is the static nature of the model, in the sense that it considers only the transmission of light to the fetus through a single measurement of tissue thickness [Scheel et al., 2018]. In reality, the thickness of maternal abdominal tissue varies across not only individuals but also in measurement location (e.g., higher tissue density near the spine than the ribcage) and temporally across the gestation period.

Beyond the aforementioned research, the literature is relatively sparse with regard to MC modelling of light propagation to the fetus. In preparing this thesis, few studies were found to use MC methods to simulate photon transport to the fetus. Examples include Gan et al. [2011] and Jumadi et al. [2014], both of which use commercial MC packages (TracePro and ASAP, respectively) to simulate aspects related to power incident on and around the fetus for applications in fetal heart rate detection [Gan et al., 2011] and experimental safety design [Jumadi et al., 2014]. As well as being focused on a different aspect of simulation, these papers are of low value to this research as the modelling techniques are minimally discussed or expanded upon.

A more recent investigation employing MC methods is that of Gunther et al. [2021]. These authors model the effect of amniotic fluid on the amount of light reaching the fetus, with reference to uses for detecting fetal distress in relation to potential caesarean delivery. The authors simulate two scenarios: one where the fluid is present and one where it is not. By comparing the two situations, they are able to determine how much reflectance is due to the fluid and how much is simply due to the fetus, as well as developing their understanding of the amount of light incident on the fetus. Though such research is somewhat similar in principle to the focus of this thesis, a crucial difference is that the paper considers only one location of the fetal head and stimuli delivery — there is no simulation of stimuli delivery from alternative locations. In addition, it does not consider any individual variation in tissue profile.

There is relatively little further research modelling photon transmission to the fetus through any means (MC or otherwise). One example is that of Jacques et al. [2000], who use the diffusion approximation to implement the perturbation method in order to simulate photon transport through the fetal brain; however, again, there is little consideration of the dynamically dispersive tissue involved with the maternal abdomen, and the paper serves primarily as a proof-of-concept for future applications. In addition, the authors make several large assumptions, such as assuming infinite maternal abdomen tissue to more easily employ the diffusion approximation.

To summarise, the pre-existing research of direct relevance to this project is limited. Those papers that do investigate similar scenarios do so with: different conditions, alternative means of modelling, simplistic assumptions, and/or limited extension to the temporal (and dynamic) nature of pregnancy. Consequently, the modelling proposed for the work involved in this thesis would appear to be the first of its kind to account for such a wide range of variables and considerations.

References

E. Alerstam, T. Svensson, and S. Andersson-Engels. Parallel computing with graphics processing units for high-speed Monte Carlo simulation of photon migration. *Journal of Biomedical Optics*, 13(6):1 – 3, 2008.

V. B. Baranov and Y. G. Malama. Model of the solar wind interaction with the local interstellar medium: Numerical solution of self-consistent problem. *Journal of Geophysical Research*, 98:15157–15163, 1993.

M. J. Berger. Monte Carlo Calculation of the Penetration and Diffusion of Fast Charged Particles. *Methods in Computational Physics*, 135, 1963.

K. Bhan and J. Spanier. Condensed history Monte Carlo methods for photon transport problems. *Journal of Computational Physics*, 225:1673–1694, 09 2007.

A. F. Bielajew. History of Monte Carlo. In J. Seco and F. Verhaegen, editors, *Monte Carlo Techniques in Radiation Therapy*, pages 3–17, 2013.

D. A. Boas, J. P. Culver, J. J. Stott, and A. K. Dunn. Three dimensional Monte Carlo code for photon migration through complex heterogeneous media including the adult human head. *Opt. Express*, 10(3):159–170, Feb 2002.

L. L. Carter and E. D. Cashwell. Particle-transport simulation with the Monte Carlo method. Technical report, Los Alamos Scientific Lab., N. Mex. (USA), 1 1975.

S. Chandrasekhar. *Radiative Transfer*. Dover Publications, 1960.

W.F. Cheong, S.A. Prahl, and A.J. Welch. A review of the optical properties of biological tissues. *IEEE Journal of Quantum Electronics*, 26(12):2166–2185, 1990.

G. L. L. Comte de Buffon. *Essai d'arithmétique morale*. Supplément à l'Histoire Naturelle, 1777.

D. Côté and I. A. Vitkin. Robust concentration determination of optically active molecules in turbid media with validated three-dimensional polarization sensitive Monte Carlo calculations. *Opt. Express*, 13(1):148–163, Jan 2005.

H. S. M. Coxeter. *Non-Euclidean Geometry: Fifth Edition*. University of Toronto Press, 1957.

K. Das, T. Yuasa, I. Nishidate, H. Funamizu, and Y. Aizu. Simulated reflectance spectra and point spread functions in database constructed by moderate grouping of nine layers in skin model. *Optical Review*, 27, 02 2020.

M. Del Giudice. Alone in the Dark? Modeling the Conditions for Visual Experience in Human Fetuses. *Developmental Psychobiology*, 53:214–219, 2011.

J. J. Duderstadt and L. J. Hamilton. *Nuclear Reactor Analysis*. 1 1976.

R. Eckhardt. Stan Ulam, John von Neumann, and the Monte Carlo Method. *Los Alamos Science*, 15:131–137, 1987.

Q. Fang. Mesh-based Monte Carlo method using fast ray-tracing in Plücker coordinates. *Biomed. Opt. Express*, 1(1):165–175, Aug 2010.

Q. Fang and D. A. Boas. Monte Carlo Simulation of Photon Migration in 3D Turbid Media Accelerated by Graphics Processing Units. *Opt. Express*, 17 (22):20178–20190, Oct 2009.

S. T. Flock, B. C. Wilson, and M. S. Patterson. Hybrid Monte Carlo - Diffusion Theory Modelling Of Light Distributions In Tissue. In Michael W. Berns, editor, *Laser Interaction with Tissue*, volume 0908, pages 20 – 28. International Society for Optics and Photonics, SPIE, 1988.

S. T. Flock, M. S. Patterson, B. C. Wilson, and D. R. Wyman. Monte Carlo modeling of light propagation in highly scattering tissues. I. Model predictions and comparison with diffusion theory. *IEEE Transactions on Biomedical Engineering*, 36(12):1162–1168, 1989.

J. Fulford, S. H. Vadeyar, S. H. Dodampahala, R. J. Moore, P. Young, P. N. Baker, D. K. James, and P. A. Gowland. Fetal brain activity in response to a visual stimulus. *Human Brain Mapping*, 20, 2003.

K. B. Gan, E. Zahedi, and M. Mohd Ali. Investigation of optical detection strategies for transabdominal fetal heart rate detection using three-layered tissue model and Monte Carlo simulation. *Optica Applicata*, 41:277–282, 01 2011.

R. Graaff, M. Koelink, F. Mul, W. G. Zijistra, C. Dassel, and J. Aarnoudse. Condensed Monte Carlo simulations for the description of light transport. *Applied Optics*, 32:426–34, 02 1993.

J. Gunther, B. Jayet, A. Jacobs, R. Burke, J. Kainerstorfer, and S. Andersson-Engels. Effect of the presence of amniotic fluid for optical transabdominal fetal monitoring using Monte Carlo simulations. *Journal of Biophotonics*, 14, 06 2021.

J. D. Hardy, H. T. Hammel, and D. Murgatroyd. Spectral transmittance and reflectance of excised human skin. *Journal of Applied Physiology*, 9(2):257–264, 1956.

T. Hayashi, Y. Kashio, and E. Okada. Hybrid Monte Carlo-diffusion method for light propagation in tissue with a low-scattering region. *Applied Optics*, 42(16):2888–2896, Jun 2003.

J. Heerikhuisen, V. Florinski, and G. P. Zank. Interaction between the solar wind and interstellar gas: A comparison between Monte Carlo and fluid approaches. *Journal of Geophysical Research (Space Physics)*, 111(A6), June 2006.

L. G. Henyey and J. L. Greenstein. Diffuse radiation in the Galaxy. *The Astrophysical Journal*, 93:70–83, January 1941.

S. Jacques, N. Ramanujam, G. Vishnoi, R. Choe, and B. Chance. Modeling photon transport in transabdominal fetal oximetry. *Journal of Biomedical Optics*, 5:277–82, 08 2000.

S. Jacques, D. Weaver, and S. Reppert. Penetration of Light Into the Uterus of Pregnant Mammals. *Photochemistry and Photobiology*, 45:637 – 641, 01 2008.

S. L. Jacques. Light distributions from point, line and plane sources for photochemical reactions and fluorescence in turbid biological tissues. *Photochemistry and Photobiology*, 67(1):23–32, 1998.

S. L. Jacques. Optical properties of biological tissues: a review. *Physics in Medicine & Biology*, 58(11):R37–R61, 5 2013.

S. L. Jacques and B. W. Pogue. Tutorial on diffuse light transport. *Journal of Biomedical Optics*, 13(4):1 – 19, 2008.

S. L. Jacques and S. A. Prahl. Modeling optical and thermal distributions in tissue during laser irradiation. *Lasers Surg. Med.*, 6:494–503, 1987.

S. L. Jacques and L. Wang. Monte Carlo Modeling of Light Transport in Tissues. In Ashley J. Welch and Martin J. C. Van Gemert, editors, *Optical-Thermal Response of Laser-Irradiated Tissue*, pages 73–100. Springer US, 1995.

S. L. Jacques, C. A. Alter, and S. A. Prahl. Angular dependence of HeNe laser light scattering by human dermis. *Lasers in the Life Sciences*, 1:309–333, 1987.

N. A. Jumadi, K. B. Gan, M. Mohd Ali, and E. Zahedi. Investigating the Effect of Total Radiated Power on Fetus Using Optical Simulation Approach Based on Exposure Safety Limit for Eye and Tissue Injury. *Journal of Life Sciences and Technologies*, 2:24–27, 01 2014.

I. Kawrakow. Accurate condensed history Monte Carlo simulation of electron transport. II. Application to ion chamber response simulations. *Medical Physics*, 27(3):499–513, 2000.

M. Keijzer, S. Jacques, S. Prahl, and A. Welch. Light distributions in artery tissue: Monte Carlo simulations for finite-diameter laser beams. *Lasers in Surgery and Medicine*, 9:148–154, 1989.

P. Kubelka. New Contributions to the Optics of Intensely Light-Scattering Materials. Part I. *Journal of the Optical Society of America*, 38(5):448–457, May 1948.

P. Kubelka. New Contributions to the Optics of Intensely Light-Scattering Materials. Part II: Nonhomogeneous Layers. *Journal of the Optical Society of America*, 44(4):330–335, Apr 1954.

D. P. Landau and K. Binder. *A Guide to Monte Carlo Simulations in Statistical Physics*. Cambridge University Press, 4 edition, 2014.

P. S. Laplace. Theorie analytique des probabilités, Livre 2. In *Oeuvres complétes de Laplace*, volume 7, pages 365–366, 1886.

H. Li, J. Tian, F. Zhu, W. Cong, L. V. Wang, E. A. Hoffman, and G. Wang. A mouse optical simulation environment (MOSE) to investigate bioluminescent phenomena in the living mouse with the Monte Carlo method. *Academic Radiology*, 11(9):1029–1038, 2004.

G. W. Lucassen, W. Verkruysse, M. Keijzer, and M. J. C. van Gemert. Light distributions in a port wine stain model containing multiple cylindrical and curved blood vessels. *Lasers in Surgery and Medicine*, 18(4):345–357, 1996.

T. Maeda, N. Arakawa, M. Takahashi, and Y. Aizu. Monte Carlo simulation of spectral reflectance using a multilayered skin tissue model. *Optical Review*, 17:223–229, 05 2010.

Y. G. Malama. Monte-Carlo Simulation of Neutral Atoms Trajectories in the Solar System. *Astrophysics and Space Science*, 176(1):21–46, February 1991.

E. Margallo-Balbás and P. J. French. Shape based Monte Carlo code for light transport in complex heterogeneous tissues. *Opt. Express*, 15(21):14086–14098, Oct 2007.

J. C. Maxwell. V. Illustrations of the dynamical theory of gases.—Part I. On the motions and collisions of perfectly elastic spheres. *The London, Edinburgh, and Dublin Philosophical Magazine and Journal of Science*, 19 (124):19–32, 1860.

I. Meglinski and S. Matcher. Quantitative assessment of skin layers absorption and skin reflectance spectra simulation. *Physiological measurement*, 23:741–53, 12 2002.

I. Meglinski and S. Matcher. Computer simulation of the skin reflectance spectra. *Computer methods and programs in biomedicine*, 70 2:179–86, 2003.

N. Metropolis. The beginning of the Monte Carlo method. *Los Alamos Science*, pages 125–130, 1987.

N. Metropolis and S. Ulam. The Monte Carlo Method. *Journal of the American Statistical Association*, 44(247):335–341, 1949.

N. Metropolis, A. W. Rosenbluth, M. N. Rosenbluth, A. H. Teller, and E. Teller. Equation of state calculations by fast computing machines. *Journal of Chemical Physics*, 21:1087–1092, 1953.

B. Nasouri, T. E. Murphy, and H. Berberoglu. Simulation of laser propagation through a three-layer human skin model in the spectral range from 1000 to 1900 nm. *Journal of Biomedical Optics*, 19(7):1 – 9, 2014.

I. Nishidate, Y. Aizu, and H. Mishina. Estimation of absorbing components in a local layer embedded in the turbid media on the basis of visible to near-infrared (vis-nir) reflectance spectra. *Optical Review*, 10:427–435, 09 2003.

I. Nishidate, Y. Aizu, and H. Mishina. Estimation of melanin and hemoglobin in skin tissue using multiple regression analysis aided by Monte Carlo simulation. *Journal of Biomedical Optics*, 9(4):700 – 710, 2004.

I. Nishidate, Y. Aizu, and H. Mishina. Depth visualization of a local blood region in skin tissue by use of diffuse reflectance images. *Optics Letters*, 30 (16):2128–2130, Aug 2005.

I. Nishidate, T. Maeda, Y. Aizu, and K. Niizeki. Visualizing depth and thickness of a local blood region in skin tissue using diffuse reflectance images. *Journal of Biomedical Optics*, 12(5):1 – 12, 2007.

M. S. Patterson, B. C. Wilson, and D. R. Wyman. The Propagation of Optical Radiation in Tissue I. Models of Radiation Transport and their Application. *Lasers in Medical Science*, 6:155–168, 2005a.

M. S. Patterson, B. C. Wilson, and D. R. Wyman. The propagation of optical radiation in tissue. ii: Optical properties of tissues and resulting fluence distributions. *Lasers in Medical Science*, 6:379–390, 2005b.

S. V. Patwardhan, A. P. Dhawan, and P. A. Relue. Monte Carlo simulation of light-tissue interaction: three-dimensional simulation for trans-illumination-based imaging of skin lesions. *IEEE Transactions on Biomedical Engineering*, 52(7):1227–1236, July 2005.

V. Periyasamy and M. Pramanik. Monte Carlo simulation of light transport in turbid medium with embedded object—spherical, cylindrical, ellipsoidal, or cuboidal objects embedded within multilayered tissues. *Journal of Biomedical Optics*, 19(4):1 – 10, 2014.

V. Periyasamy and M. Pramanik. Advances in Monte Carlo Simulation for Light Propagation in Tissue. *IEEE Reviews in Biomedical Engineering*, PP, 08 2017.

T. J. Pfefer, J. Kehlet Barton, E. K. Chan, M. G. Ducros, B. S. Sorg, T. E. Milner, J. S. Nelson, and A. J. Welch. A three-dimensional modular adaptable grid numerical model for light propagation during laser irradiation of skin tissue. *IEEE Journal of Selected Topics in Quantum Electronics*, 2(4): 934–942, December 1996.

N. Platis and T. Theoharis. Fast ray-tetrahedron intersection using plucker coordinates. *Journal of Graphics Tools*, 8(4):37–48, 2003.

S. A. Prahl. Monte Carlo Multi-Layered (MCML). `https://omlc.org/software/mc/mcml/`, 2017.

S. A. Prahl, M. Keijzer, S. L. Jacques, and A. J. Welch. A Monte Carlo model of light propagation in tissue. In G. J. Müller and D. H. Sliney, editors, *SPIE Proceedings of Dosimetry of Laser Radiation in Medicine and Biology*, volume IS 5, pages 102–111, 1989.

A. E. Profio. *Radiation Shielding and Dosimetry*, pages 168–199. Wiley, 1979.

D. E. Raeside. Monte Carlo Principles and Applications. *Physics in Medicine & Biology*, 21(2):181–197, 3 1976.

V. Reid, K. Dunn, R. Young, J. Amu, T. Donovan, and N. Reissland. The Human Fetus Preferentially Engages with Face-like Visual Stimuli. *Current Biology*, 28:824, 03 2017.

N. Ren, J. Liang, X. Qu, J. Li, B. Lu, and J. Tian. GPU-based Monte Carlo simulation for light propagation in complex heterogeneous tissues. *Opt. Express*, 18(7):6811–6823, Mar 2010.

S. Ren, X. Chen, H. Wang, X. Qu, G. Wang, J. Liang, and J. Tian. Molecular Optical Simulation Environment (MOSE): A Platform for the Simulation of Light Propagation in Turbid Media. *PLOS ONE*, 8:e61304, 04 2013.

J. Sandell and T. Zhu. A review of in-vivo optical properties of human tissues and its impact on PDT. *Journal of Biophotonics*, 4:773–87, 11 2011.

A. M. Scheel, S. J. Ritchie, N. J. L. Brown, and S. L. Jacques. Methodological problems in a study of fetal visual perception. *Current Biology*, 28(10): R594–R596, 2018.

H. Shen and G. Wang. A tetrahedron-based inhomogeneous Monte Carlo optical simulator. *Physics in Medicine and Biology*, 55(4):947–962, jan 2010.

D. J. Smithies and P. H. Butler. Modelling the distribution of laser light in port-wine stains with the Monte Carlo method. *Physics in Medicine & Biology*, 40(5):701–731, may 1995.

V. V. Tuchin. *Tissue Optics*, pages 132–142. SPIE, 2007.

J. von Neumann and R. D. Richtmyer. 2. Statistical Methods in Neutron Diffusion. In A. R. Bednarek and Francoise Ulam, editors, *Analogies Between Analogies: The Mathematical Reports of S. M. Ulam and his Los Alamos Collaborators*, pages 17–36. University of California Press, 1947.

S. Wan, J. A. Parrish, R. R. Anderson, and M. Madden. Transmittance of Nonionizing Radiation in Human Tissues. *Photochemistry and Photobiology*, 34(6):679–681, 1981.

L. Wang, S. L. Jacques, and L. Zheng. MCML — Monte Carlo modeling of light transport in multi-layered tissues. *Computer Methods and Programs in Biomedicine*, 47(2):131–146, 1995.

L. Wang, S. Ren, and X. Chen. Comparative evaluations of the Monte Carlo-based light propagation simulation packages for optical imaging. *Journal of Innovative Optical Health Sciences*, 11:1750017, 2018.

L. V. Wang and H. Wu. *Biomedical Optics: Principles and Imaging.* Wiley, 2007.

L. V. Wang, R. E. Nordquist, and W. R. Chen. Optimal beam size for light delivery to absorption-enhanced tumors buried in biological tissues and effect of multiple-beam delivery: a Monte Carlo study. *Appl. Opt.*, 36(31):8286–8291, Nov 1997.

A. J. Welch and M. J. C. van Gemert. *Optical-Thermal Response of Laser-Irradiated Tissue.* Springer New York, 1995.

A. J. Welch and M. J. C. van Gemert. *Optical-Thermal Response of Laser-Irradiated Tissue.* Springer Netherlands, 2011.

B. C. Wilson and G. Adam. A Monte Carlo model for the absorption and flux distributions of light in tissue. *Medical Physics*, 10(6):824–830, 1983.

C. Zhu and Q. Liu. Hybrid method for fast Monte Carlo simulation of diffuse reflectance from a multilayered tissue model with tumor-like heterogeneities. *Journal of Biomedical Optics*, 17(1):1 – 4, 2012.

C. Zhu and Q. Liu. Review of Monte Carlo modeling of light transport in tissues. *Journal of Biomedical Optics*, 18(5):1 – 13, 2013.

Chapter 3

An Inspection of the Algorithm and Theoretical Considerations

Here, we provide a comprehensive outline of the base algorithm and theory employed by steady-state MC models of light propagation in multiple layers of simple, homogeneous tissue. A summary flowchart of the general processes common to all models is provided in Figure 3.1 for reference.

3.1 The Input File

The medium through which the photons propagate is specified by several optical properties. Specifically, as a photon follows its trajectory, there are two types of interaction it may have with the medium. First, the presence of light-absorbing molecules (referred to as chromophores) within the medium allows for the possibility of photon absorption. This occurs when a photon transfers its energy to an electron in the absorbing molecule, exciting it to a higher energy level. Second, as light interacts with particles in the medium, there is also the potential for photon scattering — for instance, due to differing indices of refraction across the boundaries of the particles (caused by a difference in phase velocities). Photons may also undergo scattering events upon collision with molecules within the medium, resulting in photon absorption and re-emission from the molecule. Hence, within our model, we require medium-specific pa-

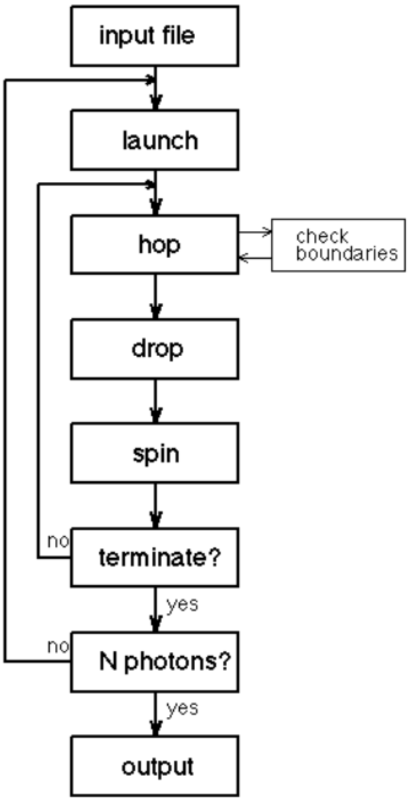

Figure 3.1: A basic flowchart outlining the common algorithm employed in simulating photon trajectories. Image credit: Jacques [2011].

rameters to be defined that account for the likelihood of photon absorption and photon scattering. In this section, we discuss these parameters alongside several others relevant to our model.

3.1.1 Absorption Coefficient, μ_a

In considering absorption, we first envisage a spherical chromophore for simplicity. Imagining the absorption capabilities of this chromophore, we picture that its geometrical area (A [cm^2]) impedes the propagation of light and casts a shadow of area σ_a [cm^2], where the size of this shadow is proportional to the chromophore's geometric area — i.e., $\sigma_a = Q_a A$, where Q_a is a dimensionless proportionality constant referred to as the absorption efficiency. As we are considering absorption here, we interpret the shadow (referred to as an effective cross-section) cast by our idealised chromophore to represent absorption. Figure 3.2 provides an illustration of this concept.

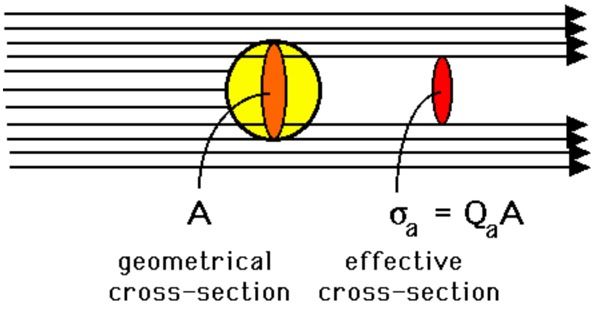

Figure 3.2: The schematics of the absorption shadow. Image credit: Jacques and Prahl [1998a].

Allowing for the presence of many chromophores in our medium, we assume they are concentrated with number density ρ_a [cm^{-3}]. Hence, the total effective cross-sectional area for absorption per unit volume of medium is given by $\mu_a = \sigma_a \rho_a$, where μ_a is in units [cm^{-1}] and is referred to as the absorption coefficient. Further physical insight into this result is provided in Section 3.1.2.1. Note also that absorption by different absorbers is here considered to be independent. Lastly, we can take the physical interpretation of this coefficient to be that the probability of photon absorption in the medium per infinitesimal path length Δs is given by $\mu_a \Delta s$.

3.1.2 Scattering Coefficient, μ_s

We then define the scattering coefficient, μ_s, analogously. Our spherical particle is now designated as a scatterer with geometrical area A [cm^2], and we again assume incident light in the form of photons is impeded; however, it is now scattered into new directions rather than being absorbed. This impeding of the propagation can again be visualised for ease as a shadow with area σ_s [cm^2], where the size of this shadow is proportional to the particle's geometric area — i.e., $\sigma_s = Q_s A$, where Q_s is a dimensionless proportionality constant referred to as the scattering efficiency. We interpret the process of diverting photons around the particle and casting a shadow (effective cross-section) to represent scattering. Figure 3.3 provides an illustration of this concept.

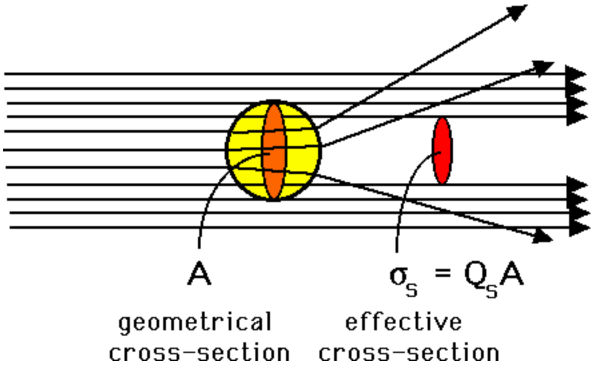

Figure 3.3: The schematics of the scattering process. Image credit: Jacques and Prahl [1998d].

Following the same extension from one particle to many as for the absorption coefficient, we determine the scattering coefficient, $\mu_s = \sigma_s \rho_s$, where μ_s has units [cm^{-1}]. This is the cross-sectional area for scattering per unit volume of medium and, again, we can take the physical interpretation of this coefficient to be that the probability of a photon scattering in the medium per infinitesimal path length Δs is given by $\mu_s \Delta s$. More physical insight for the scattering coefficient is provided in the following section.

3.1.2.1 Mean Free Path, λ

An extension to the concepts of the absorption and scattering coefficients is that of the mean free path. Within this context, the mean free path, λ, is typically used to refer to the average distance a photon will travel between tissue interactions (i.e., absorption or scattering events). To physically motivate this concept, we first consider the photon as a classical particle (in a similar manner to that implicit in the discussions of the previous subsections). Note that this assumption is the norm for MC modelling of photon interactions within tissue [Wang and Wu, 2007].

We next refer to Figure 3.4. Assuming the particle has a diameter d and a radius of $d/2$, we can determine the effective interaction area (cross-section) to be the circle drawn out by a radius equal to the summation of the particle's radius and that of the particle from the medium (say, $D/2$). Hence, we have an effective interaction area around the photon of $\frac{1}{4}\pi(d+D)^2$, which is represented by the dashed circle in the image and also corresponds to the summation of our previously mentioned shadows for absorption and scattering. Note that the figure shows the medium particle as being the same size as the photon; however, we can picture it as having some radius $D/2$.

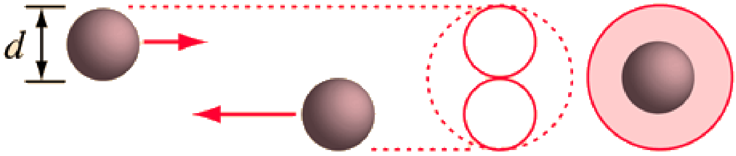

Figure 3.4: A diagram illustrating the effective interaction area around the photon. Adapted from: HyperPhysics [2016].

If we then envisage this photon to travel a distance of $\bar{v}t$ in some time, t, we can picture the effective interaction area to map out a volume given by $\frac{1}{4}\pi(d+D)^2\bar{v}t$. Taking our interacting tissue particles to be concentrated in this volume (and the medium) with number density ρ, we can see the number of interactions by a photon in this volume will be given by $\frac{1}{4}\pi(d+D)^2\bar{v}t\rho$. Hence, the mean free path of a photon can then be calculated as the division of the total path length by the number of collisions in that volume:

$$\lambda = \frac{\bar{v}t}{\frac{1}{4}\pi(d+D)^2\bar{v}t\rho} \tag{3.1}$$

$$= \frac{1}{\frac{1}{4}\pi(d+D)^2\rho} \tag{3.2}$$

$$= \frac{1}{\sigma\rho} \tag{3.3}$$

$$= \frac{1}{\mu}, \tag{3.4}$$

where we have here used σ to represent the effective interaction area and μ to represent the interaction coefficient. This second variable is often referred to as the attenuation coefficient, and this will be expanded on in Section 3.3.1.

There are several variants of the above mean free path, and these are derived in a similar manner. Most commonly, we consider the scattering mean free path ($\frac{1}{\mu_s}$) and the mean absorption length ($\frac{1}{\mu_a}$), which respectively define the average distance a photon will travel between scattering or absorption events.

3.1.3 Anisotropy Factor, g

Following from the concept of a scattering coefficient, for reasons which will be made clearer in later discussion, we also introduce the anisotropy factor, g. This parameter is a dimensionless, tissue-dependent constant that defines the average interaction outcome between a photon and a scatterer. Specifically, when a photon undergoes a scattering event, there is a component of its initial forward trajectory which is retained after the collision, and the average of this value across all scattering events is g. Referring to Figure 3.5, we see that a scattering event results in a deflection of the photon from its initially rightward horizontal trajectory by the angle θ. In addition, there is an azimuthal angle of scattering, ψ, about the horizontal axis (in this figure) which further defines the photon's trajectory; however, if we take the rightward direction to be "forward", the retained forward direction after any such scattering event is independent of ψ and simply calculated as $\cos(\theta)$.

If we consider all possible scattering events occurring within the medium, it becomes clear that the average forward direction retained after a scattering event is equivalent to the mean value of $\cos(\theta)$. Thus, we have, by definition, $g = \langle\cos(\theta)\rangle$. More discussion surrounding the mathematical definition of g is provided in Section 3.5.2.1.

Clearly, g has possible values given by $-1 \leq g \leq 1$, with the extreme low of $g = -1$ corresponding to a solely backward scattering medium and the extreme high of $g = 1$ corresponding to a solely forward scattering medium. Both instances are anisotropic (by definition, as their anisotropy values are not equal to 0, meaning scattering is more likely in a particular direction), while

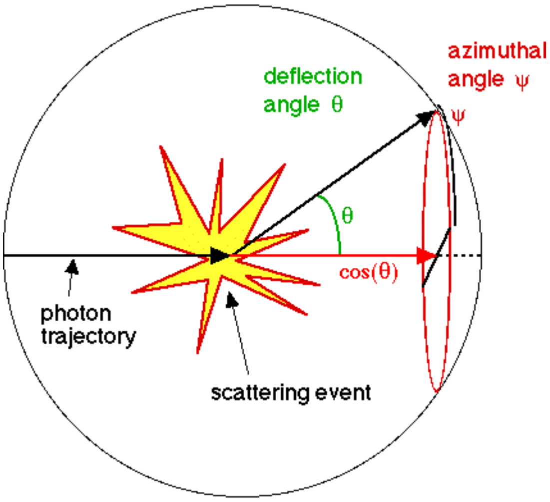

Figure 3.5: A cartoon illustration of the scattering event and involved geometries. Image credit: Jacques and Prahl [1998b].

the case of an isotropic medium (where there is equal likelihood of scattering in all directions) would correspond to $g = 0$. Hence, the anisotropy factor is an important optical parameter for the model in the sense that it defines the nature of the medium. In our case, most biological tissues have a g value of $\sim$0.9 (see Section 2.4), which indicates a highly forward scattering medium — i.e., most scattering interactions result in the photons continuing to travel in a heavily forward-oriented direction.

3.1.3.1 Reduced Scattering Coefficient, μ_s'

With the scattering coefficient, μ_s, and the anisotropy parameter, g, both now defined, we are able to introduce the reduced scattering coefficient (also known as the transport scattering coefficient):

$$\mu_s' = \mu_s(1 - g). \tag{3.5}$$

The physical interpretation of the reduced scattering coefficient can be summarised in a similar manner to those coefficients described in Sections 3.1.1 and 3.1.2 — i.e., it describes the distance travelled before interaction — however, there are several important differences. In particular, the reduced scattering coefficient is defined during the derivation of the diffusion equation. We do not here present a theoretical discussion or derivation of the diffusion approximation (nor its fundamental equations), though one might refer to Wang and Wu [2007] for a review.

As a result of this derivational context, the reduced scattering coefficient is used in situations where the diffusion approximation applies — that is, where there are many scattering events before an absorption event ($\mu_s \gg \mu_a$, as also discussed in Section 2.3). In particular, its interpretation describes the diffusion of photons as involving a random walk with isotropic scattering and steps of size $\frac{1}{\mu_s'}$, with the caveat that each of these steps consists of many smaller anisotropic scattering steps of size $\frac{1}{\mu_s}$. As an example, see Figure 3.6.

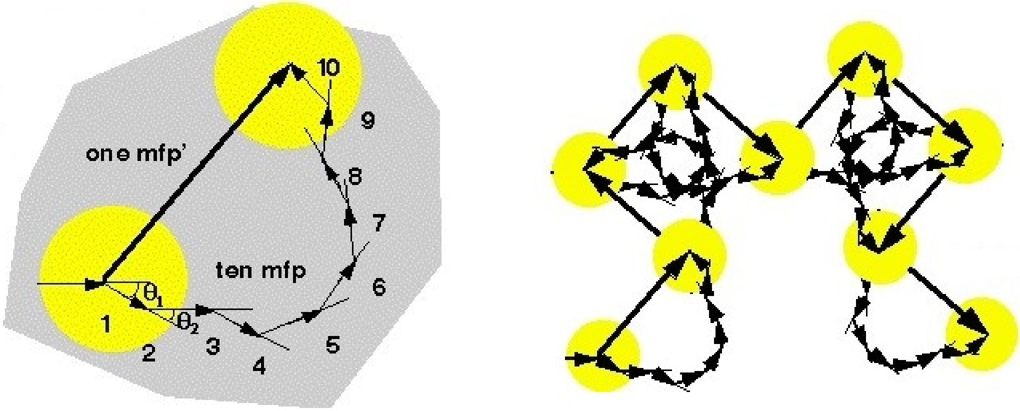

Figure 3.6: A cartoon showing (left) the equivalence of ten small anisotropic scattering steps of size $\lambda = 1/\mu_s$ to a single larger step with the reduced mean free path of $\lambda' = 1/\mu_s'$. On the right, a demonstration shows that many of these larger steps with isotropic scattering can represent many smaller steps with anisotropic scattering. Image credit: Jacques and Prahl [1998c].

Further understanding of the reduced scattering coefficient can be gained from considering scattering distributions. For instance, in Figure 3.7, we see an example polar plot for an isotropic distribution. If we imagine a beam of light approaching from the left of the figure's central scattering particle, the circular plot indicates the particle will scatter light in all directions with equal efficiency. In other words, all directions are equally likely for the photon to be scattered into. This can be represented by a scattering function of the form

$$p(\theta) = \frac{1}{4\pi}, \tag{3.6}$$

where $p(\theta)$ indicates the probability of scattering into a particular angle (θ) — see Section 3.5.2 for further discussion of scattering functions. Evidently, this corresponds to isotropic scattering because it is simply dividing a sphere equally into 4π steradians. Note also that integrating over all angles gives

$$\int_0^{\pi} p(\theta) 2\pi \sin(\theta) \mathrm{d}\theta = 1, \tag{3.7}$$

as expected for a probability distribution (our scattering function).

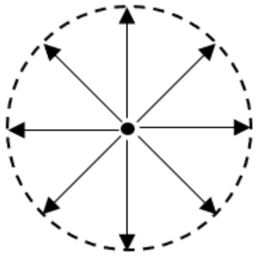

Figure 3.7: An example polar plot showing an isotropic distribution, where the incoming photons are equally likely to scatter in any direction from the central scatterer. Note that this would, in practice, be a three-dimensional situation; however, we here restrict it to two dimensions for simplicity. Image credit: Self.

If we then consider an anisotropic scattering distribution (for example, as shown in Figure 3.8), we can begin to further understand the reduced scattering coefficient.

First, we recall from Section 3.1.3 that the value of g for an anisotropic distribution, such as (A) in Figure 3.8, is $g = \langle\cos(\theta)\rangle > 0$. Similarly, for an isotropic distribution (such as in Figure 3.7), $g = \langle\cos(\theta)\rangle = 0$.

Next, in attempting to model this anisotropic distribution, we note that we cannot simply assume each interaction to exclusively involve isotropic scattering. This will result in light scattering differently to that which we would

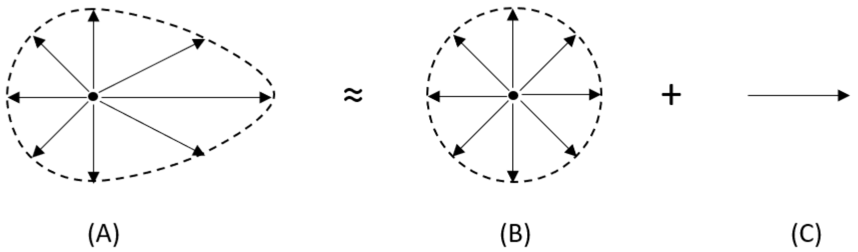

Figure 3.8: A cartoon (not to scale) showing the approximation of an anisotropic scattering distribution (A) as the combination of an isotropic scattering distribution (B) and a portion of the incoming beam that did not scatter (C). Image credit: Self.

expect in mediums where $g > 0$, such as in human tissue ($g \approx 0.9$ — see Section 2.4). Instead, we attempt to approximate the anisotropic scattering as a sum of two distributions. As shown in Figure 3.8, we approximate (A) as consisting of a smaller amount of isotropic scattering (B) and a totally forward-directed component (C). Note again that the diagram is not drawn to scale. By approximating this way, we are essentially imagining the forward-directed light (C) to bias the isotropic scattering (B) in such a way that the overall distribution of outgoing photons is more forward-directed than backward and consequently looks as shown in (A).

Specifically, we look to weight the isotropic distribution (B) by an amount given by $1 - g$, where g is the actual anisotropy of (A), and we weight the forward-directed light (C) by an amount g. In doing so, we ensure that the total distribution weight still sums to unity. In addition, if we then inspect the overall anisotropy, we see that it is simply zero for (B) (because an isotropic distribution with weighting of $1 - g \implies 0 \times (1 - g)$), and it is g for (C) — because forward-directed light with a weighting of $g \implies 1 \times g$. Consequently, the combination of the two distributions gives a single distribution with anisotropy equal to g, which is what we are attempting to approximate.

The term "reduced scattering" coefficient becomes apparent when we consider (C) to represent light which did not scatter — i.e., it is a component which remained part of the incident beam. Hence, we are literally approximating our light beam with another that undergoes a reduced amount of scattering.

Lastly, we know the intensity will fall off for (A) as exponential decay given by $I_0 \exp(-[\mu_a + \mu_s]s)$, where I_0 is initial intensity and s represents propagation distance — see Section 3.3.1. With our reduced scattering distribution, however, the beam propagation through this "reduced" medium would not decay in the same way, as we assumed the light in (C) did not scatter at all. As a result, we update μ_s with $(1-g)\mu_s$ to reflect this reduction in scattering, so that our beam's intensity now falls off as $I_0 \exp(-[\mu_a + (1-g)\mu_s]s)$, where we then define $\mu_s' = \mu_s(1-g)$ to give the exponential decay as

$$I(s) = I_0 \exp(-[\mu_a + \mu_s']s). \tag{3.8}$$

Hence, we see where the reduced scattering coefficient can practically be introduced. If we encounter situations (such as those commonly found in tissues) where visible and near-infrared light propagates through a medium which can be approximated through the diffusion regime, we can look to employ this concept. In doing so, we can increase the efficiency of our simulations because, by introducing μ_s' and noting that $\frac{\mu_s'}{\mu_s} \approx 0.1$, we increase the distance propagated before interactions occur (from $\frac{1}{\mu_s}$ to $\frac{1}{\mu_s'}$, due to the decrease from μ_s to μ_s').

3.1.4 Refractive Index, n

The final optical parameter required to specify the tissue medium is its refractive index. This dimensionless constant is given by $n = \frac{c}{v}$, where c is the speed of light in a vacuum and v is the speed of light in the medium (or the phase velocity of light in the medium). This defines the change in speed experienced by the light as it propagates and, consequently, the amount of "bending" photon trajectories undertake between mediums. The refractive index further leads to Snell's Law, which is discussed in 3.3.3.1.

3.1.5 Further Parameters

With the absorption coefficient, scattering coefficient, anisotropy, and refractive index specified, we have the information required to simulate propagation through an infinite, optically homogeneous medium. We note that, in reality, the tissue cannot be infinitely wide; however, it is fine to treat it as such here, on the condition that the spatial extent of the photon distribution is much thinner than the width of the tissue [Wang et al., 1995]. In the case where we have only one layer with defined parameters (as has been implied by the previous sections), our photons are able to propagate indefinitely. In the more realistic case, we must define the parameters across multiple mediums, resulting in several individually optically homogeneous mediums. In that scenario, we must also specify the thicknesses (usually measured in centimetres) of any constituent layers, as well as specifying their refractive indices. Lastly, depending on the type of simulation conducted, we need to specify the refractive index of the medium immediately before the light enters the tissue and also that of the medium after exiting the tissue.

3.2 Launch

In the case of a single collimated narrow beam, we generally begin the photons at the origin of a Cartesian coordinate system: $(x, y, z) = (0, 0, 0)$. In order to later make use of axial symmetry, we initially describe the trajectory via spherical coordinates, where θ measures the deflection from the positive z-axis and ϕ measures the rotation around the z-axis (i.e., the azimuthal angle). As mentioned in Section 2.4, however, it is common to utilise direction cosines to describe the trajectory vector, given by (u_x, u_y, u_z). As such, we take the trajectory described previously in spherical coordinates and project it onto the Cartesian axes. A visualisation is presented in Figure 3.9. We are left with the following:

$$u_x = \sin(\theta)\cos(\phi),$$

$$u_y = \sin(\theta)\sin(\phi),$$

$$u_z = \cos(\theta).$$

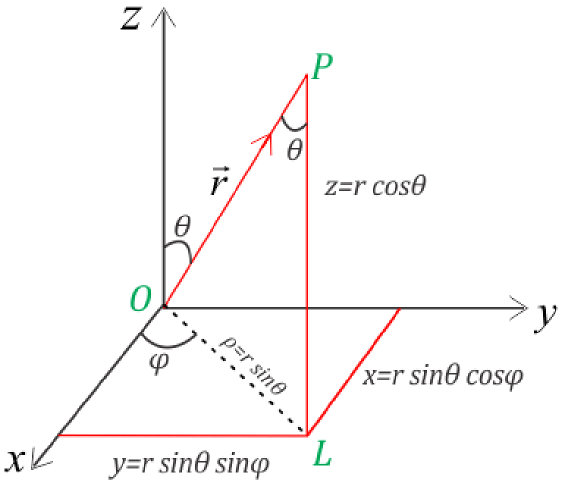

Figure 3.9: A visualisation of the initial trajectory in spherical and Cartesian coordinates. We project vector $\vec{r}$ onto the Cartesian axes and determine its equivalent components. Note, for our purposes, that $\vec{r}$ is of unit length (that is, $|\vec{r}| = r = 1$ in the diagram), as we are only interested in directional components. Image credit: PhysicsCatalyst [2021].

Depending on the type of light source being simulated, it may be necessary to adjust the generation of photon starting locations and their initial trajectories. For instance, taking the starting location to be the aforementioned origin and assigning $u_x = u_y = 0$ and $u_z = 1$, we can simulate a perfectly collimated beam where photons enter the tissue perpendicularly exactly at the origin. Alternatively, one may wish to simulate, for example, an isotropic point source or a collimated Gaussian beam or a wider area of illumination. These and other variations can be accounted for by adjusting the starting points and/or initial trajectories of the photons as necessary, which may introduce distributions. As we are explaining the general algorithm here, the specific starting location and trajectories chosen can be ignored for now, but specific scenarios enter in the applications explored in Chapters 5, 7, and 9.

Lastly, at launch, we note that each photon actually represents a photon "packet" — i.e., a bundle of photons — rather than simply an individual photon. This is a simple variation reduction technique known as implicit photon capture, with its purpose being to improve the efficiency of the MC simulation. In future sections, we will discuss the reasons behind this decision; however, we state here that each packet is assigned a "Weight" variable, W, which is initially set to unity and adjusted appropriately during the packet's propagation.

3.3 Hop

3.3.1 Determining the Step Size

In the next stage after initialising the photons, we begin to propagate them through the tissue. This process requires determination of a variable step size by sampling the appropriate probability density function (PDF). To build this concept, we first introduce the attenuation coefficient:

$$\mu_t = \mu_a + \mu_s. \tag{3.9}$$

By recalling our definitions for the absorption and scattering coefficients from Sections 3.1.1 and 3.1.2, we can see that the attenuation coefficient is defined such that the probability of photon interaction with the medium (through either absorption or scattering) per infinitesimal path length Δs is given by $\mu_t \Delta s$.

In addition, we next show a derivation of the Beer-Lambert law, which relates the attenuation of propagating light in a medium to the properties of that medium. First, consider a beam of intensity I that propagates across a distance ds, as shown in Figure 3.10. Note, for reference, that (regardless of the direction of flow) intensity is here defined as the energy flow per unit area per unit time (also known as fluence rate). As the beam crosses the distance, the constituent light attenuates as it propagates through the medium. Specifically, some is lost to absorption and some is lost to scattering, and we represent this by a change in intensity, dI, given by

$$dI = -(I\mu_a ds + I\mu_s ds), \tag{3.10}$$

where the value is negative to describe the depletion of the beam. Hence, the outgoing beam has intensity $I + dI$.

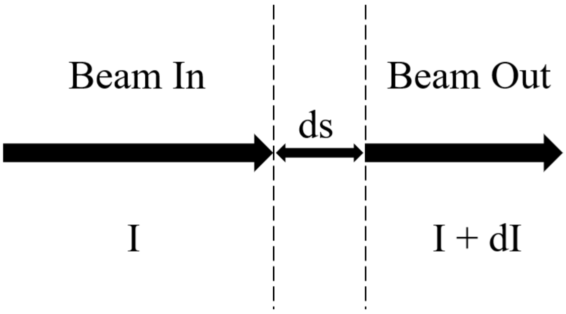

Figure 3.10: An incoming beam of intensity I is attenuated across a distance ds so that the outgoing beam has intensity $I + dI$. Image credit: Self.

Taking the differential equation in 3.10 and making use of Equation 3.9, we solve to reach the Beer-Lambert Law:

$$\begin{aligned} \Rightarrow \quad & \frac{dI}{I} = -\mu_t ds \\ \Rightarrow \quad & I(s) = I_0 \exp(-\mu_t s). \qquad (3.11) \end{aligned}$$

Here, we have used I_0 to represent the initial beam intensity.

Next, we introduce the transmittance, T, which describes the probability of photon survival after propagation over a distance, s, and is defined as

$$T = \frac{I(s)}{I_0}. \tag{3.12}$$

In other words, this gives the probability of no photon interactions with the medium after propagating a path length s. Further, we can take Equation 3.11

with the path length s_1 and use Equation 3.12 to write

$$T(s_1) = \exp(-\mu_t s_1). \tag{3.13}$$

Then, if this represents the probability of no photon interactions with the medium after a path length of s_1, we can write the complement (the probability that the photon has an interaction within s_1) as

$$P\{s < s_1\} = 1 - \exp(-\mu_t s_1). \tag{3.14}$$

Hence, we have the PDF given by

$$p(s_1) = \frac{\mathrm{d}P\{s < s_1\}}{\mathrm{d}s_1} = \mu_t \exp(-\mu_t s_1), \tag{3.15}$$

and we can see that Equation 3.14 is also the cumulative distribution function (CDF) for the step size.

Finally, we use the inverse distribution method (IDM) to sample step sizes from the PDF. This method can be summarised fairly simply. Assuming we wish to sample a variable χ based on its PDF, we first generate a random number ξ between 0 and 1. As the number is randomly generated, it should have a uniform distribution. Then, we take the CDF for χ and set it equal to our random number, ξ:

$$\int_a^\chi p(\chi) d\chi = P(\chi) = \xi, \tag{3.16}$$

where $a < \chi < b$. We then solve for χ:

$$\chi = P^{-1}(\xi). \tag{3.17}$$

This method is illustrated in Figure 3.11.

Thus, to sample the step size, we set its CDF equal to a uniformly distributed random number, ξ, and solve for the step size:

$$\begin{aligned} 1 - \exp(-\mu_t s_1) &= \xi \\ \Rightarrow \qquad s_1 &= -\frac{\ln(1-\xi)}{\mu_t} \\ \Rightarrow \qquad s_1 &= -\frac{\ln(\xi_1)}{\mu_t}. \end{aligned} \tag{3.18}$$

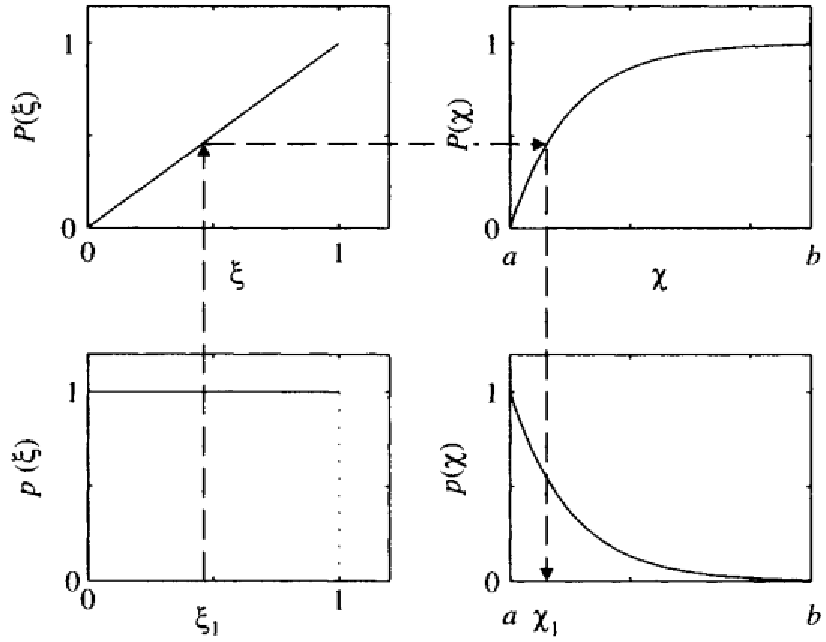

Figure 3.11: An illustration of the IDM. Image credit: Wang and Wu [2007].

In the final line, we have recognised that ξ is uniformly distributed between 0 and 1, so $1-\xi$ can be replaced with ξ_1, and our step size may now be sampled accordingly through use of Equation 3.18; however, in the above derivation, we did not consider the instance of a multilayered medium in which our photon packet might freely propagate across multiple layers before eventually experiencing an interaction. This possibility needs to be accounted for in determining the step size, as each layer can have unique interaction coefficients.

Consequently, we consider the possibility for a multilayered medium. In this instance, we modify Equation 3.13 to account for the summation of probabilities over every segment traversed by the packet before interaction:

$$P\left\{s \geq s_t\right\} = \exp\left(-\sum_i \mu_{ti} s_i\right), \tag{3.19}$$

where i designates the particular segment being traversed, μ_{ti} here represents the attenuation coefficient for the ith segment, s_i gives the length of that ith segment, and s_t is the sum of all individual segment steps — i.e., $s_t = \sum_i s_i$.

In the same manner as previously, we set this probability equal to a random number (again ξ) to obtain an equation from which we can sample the step size:

$$\sum_i \mu_{ti} s_i = -\ln(\xi). \tag{3.20}$$

Thus, we have for the multilayered medium a generalised form of Equation 3.18. In particular, we note that the LHS of Equation 3.20 represents the total *dimensionless* step size. Despite the fact that the photon packet may propagate through multiple smaller substeps of size s_i across different layers during its total step size of s_t, it is only once the photon packet travels the full dimensionless step size of $-\ln(\xi)$ that we will allow an interaction to occur. At this point, it is conventional to force the entire packet to undergo both absorption and scattering [Wang and Wu, 2007].

Hence, our process will consist of generating a total step size (via Equation 3.18), checking whether the packet will cross a boundary during the first substep of its propagation (Section 3.3.3), moving the packet and determining the result of any boundary interactions (Sections 3.3.2 and 3.3.3.4), updating the remaining step size appropriately (by reducing to zero if completing the entire step, or by first converting to dimensionless step size then recalculating the remainder via the coefficients of the new layer if necessary), and finally repeating until the original dimensionless step has been completed.

3.3.2 Update Position

After determining the step size, s_1, the photon's position is then updated by projecting s_1 onto the x, y, z axes through use of the direction cosines given in Section 3.2. This gives the updated position coordinates (x_1, y_1, z_1) as

$$x_1 = x_0 + s_1 u_x,$$

$$y_1 = y_0 + s_1 u_y,$$

$$z_1 = z_0 + s_1 u_z,$$

where we have here used (x_0, y_0, z_0) to refer to the previous coordinates.

3.3.3 Check Boundaries

In our simple, homogeneous tissue — i.e., the infinite medium previously mentioned — we have only one boundary to consider: that of the surface. Consequently, there are only two possible cases for boundary crossings during a photon's propagation: the initial crossing when the photon enters the tissue, and the case where photons may attempt to escape the tissue by coming back through the surface. Hence, we need to consider what happens to photon trajectories during these instances. Additionally, we must extend our thinking to the case of multiple tissue layers within the model, where a photon may potentially cross a boundary during any given step. These possibilities are represented in Figure 3.1 as the sideways step attached to the "Hop" stage. To determine the outcomes of these boundary interactions, we first need to introduce several fundamental aspects of optics.

3.3.3.1 Snell's Law

We recall the law of refraction (also known as Snell's law), which can be simply derived from (Fermat's) principle of least time and describes the relationship between the angle of incidence, θ_1, and the angle of transmission (or angle of refraction), θ_2, occurring when waves traverse a boundary between two distinct isotropic media:

$$n_1 \sin(\theta_1) = n_2 \sin(\theta_2), \tag{3.21}$$

where n_1 and n_2 represent the respective refractive indices of the first and second mediums. Figure 3.12 depicts the measuring geometry of a typical interaction.

3.3.3.2 Fresnel Equations

Next, we must introduce the Fresnel equations for dielectric media. Collectively, these describe how electromagnetic radiation (for our purposes, light) reflects and transmits when incident on the boundary interface between two

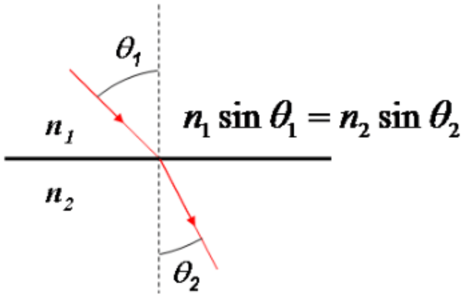

Figure 3.12: An example interaction where Snell's law is in effect. The angles of incidence and transmission are, by convention, defined with respect to the boundary normal (dashed line). Image credit: Olson et al. [2011].

optically different mediums. The derivation of these equations is relatively simple to follow, though it is long and deviates a lot from our focus; hence, we only briefly outline their background, meanings, and usages in this section. A more thorough treatment and derivation is available in many textbooks on optics — for instance, see Hecht [2001].

Upon light striking an interface between two mediums, 1 and 2, with different refractive indices, n_1 and n_2, there is both some reflection of light and an amount of refraction experienced by the transmitted light. For our simulations, we are interested in knowing how much light is reflected, how much is transmitted, what the respective angles of reflection and refraction will be, and how these values vary with changes in the refractive indices and the initial angle of incidence. This information is determined by the Fresnel equations.

We first consider an arbitrary incident beam of light upon an interface between two mediums. At the point of contact with the interface, we introduce a normal vector to the surface. The plane containing both the incident ray and the local interface normal is defined as the plane of incidence. Figure 3.13 shows an example.

In Figure 3.13, the incident ray projects from a medium with refractive index here given by n_i and strikes the interface with an angle of incidence now defined as θ_i. The plane of incidence is seen to contain the incident ray

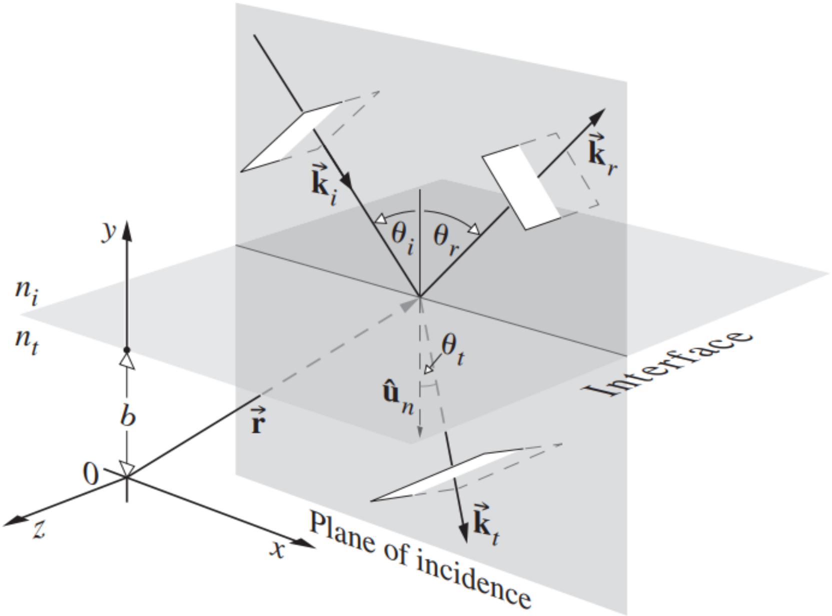

Figure 3.13: A 3-D visualization of the schematics involved when an incident ray of light interacts with an interface between two mediums with distinct refractive indices. Image credit: Hecht [2001].

and unit vector ($\hat{\boldsymbol{u}}_n$) normal to the interface (by convention, this points in the direction from the incident to the transmitting medium). The law of reflection, which is easily derived from Fermat's principle of least time in a similar manner to Equation 3.21, states that the angle of incidence is equal to the angle of reflection (the angle, θ_r, created by the reflected ray and the normal to the surface). In other words,

$$\theta_i = \theta_r, \tag{3.22}$$

and so we see the reflected component of the incident ray propagating back into the incident medium at an angle of reflection given by θ_r. For specular reflection — i.e., where Equation 3.22 holds — the reflected ray is also in the plane of incidence. Further, when refraction occurs, the refracted (transmitted) ray is in the plane as well. This can be seen in Figure 3.13 as the refracted incident ray component propagating into the second medium (here with refractive index n_t) at an angle of transmission given as θ_t.

Upon inspecting our plane of incidence (and ignoring the 3-D aspects for now), we have the situation as presented in Figure 3.14. Note that we have further vectors annotated to represent the electric ($\vec{\boldsymbol{E}}$) and magnetic ($\vec{\boldsymbol{B}}$) fields, which are the fundamental carriers of electromagnetic waves (light).

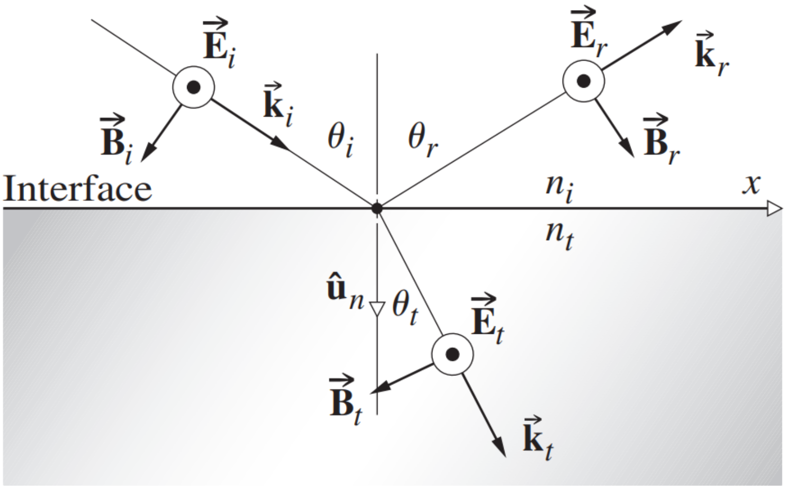

Figure 3.14: A 2-D visualization of an incident ray of light interacting with the interface between two mediums with distinct refractive indices. Image credit: Hecht [2001].

Light is a transverse wave (i.e., its oscillations are perpendicular to the direction of its propagation), though the oscillations involved with the wave are in the form of electric and magnetic fields. We recall that the propagation vector ($\hat{\boldsymbol{k}}$), $\vec{\boldsymbol{E}}$, and $\vec{\boldsymbol{B}}$ form a right-handed system. Physically, this means the motional emf generated is an electric field perpendicular to the direction of propagation through the magnetic field, and the electric field has no component in the direction of propagation. Mathematically, this is shown as:

$$\hat{\boldsymbol{k}} \times \vec{\boldsymbol{E}} = v\vec{\boldsymbol{B}}, \tag{3.23}$$

$$\hat{\boldsymbol{k}} \cdot \vec{\boldsymbol{E}} = 0. \tag{3.24}$$

Next, we consider two extreme cases for the orientations of the involved fields: first, where the electric field is perpendicular to the plane of incidence (one form of this situation is shown in Figure 3.14, where $\vec{\boldsymbol{E}}$ points outwards), and the second case where the electric field is parallel to the plane of incidence (for instance, by swapping the directions of the fields in Figure 3.14). These cases correspond to two linear polarization components of the incident wave: s-polarization when the electric field is normal to the plane, and p-polarization when the field is parallel to the plane. Though it may initially appear to do so, these extreme case plane-polarized forms will not present a hindering assumption to our work; it is easily shown that producing two orthogonal linearly polarized waves is possible from any form of light (for further, see Hecht [2001]).

Thus, with our now plane-polarized light, we may impose boundary conditions on the $\vec{\boldsymbol{E}}$-field and $\vec{\boldsymbol{B}}$-field across the interface (again, see Hecht [2001]) to introduce the Fresnel equations:

$$\begin{aligned}
r_{\perp} &= \frac{n_i\cos(\theta_i) - n_t\cos(\theta_t)}{n_i\cos(\theta_i) + n_t\cos(\theta_t)} &&= -\frac{\sin(\theta_i - \theta_t)}{\sin(\theta_i + \theta_t)}, && (3.25)\\
t_{\perp} &= \frac{2n_i\cos(\theta_i)}{n_i\cos(\theta_i) + n_t\cos(\theta_t)} &&= +\frac{2\sin(\theta_t)\cos(\theta_i)}{\sin(\theta_i + \theta_t)}, && (3.26)\\
r_{\parallel} &= \frac{n_t\cos(\theta_i) - n_i\cos(\theta_t)}{n_i\cos(\theta_t) + n_t\cos(\theta_i)} &&= +\frac{\tan(\theta_i - \theta_t)}{\tan(\theta_i + \theta_t)}, && (3.27)\\
t_{\parallel} &= \frac{2n_i\cos(\theta_i)}{n_i\cos(\theta_t) + n_t\cos(\theta_i)} &&= +\frac{2\sin(\theta_t)\cos(\theta_i)}{\sin(\theta_i + \theta_t)\cos(\theta_i - \theta_t)}, && (3.28)
\end{aligned}$$

where $r_{\perp}$ and $t_{\perp}$ are the amplitude reflection and transmission coefficients for the case where $\vec{\boldsymbol{E}}$ is perpendicular to the photon propagation, while $r_{\parallel}$ and $t_{\parallel}$ are the equivalent coefficients for when $\vec{\boldsymbol{E}}$ is parallel to the photon propagation. These coefficients represent, for the perpendicular and parallel cases, the ratio of the electric field amplitudes for the reflected (r coefficient) or refracted (t coefficient) rays to the equivalent amplitude of the incident ray's electric field. The equations on the left are those initially reached through imposing the boundary conditions, while those on the right are a commonly used notational simplification which can be reached through use of Snell's Law and several trigonometric identities. Note that, in using these equations, we assume a planar interface between the mediums and that the mediums themselves are homogeneous and isotropic — these points fit with our assumptions thus far.

3.3.3.3 Further Definitions

We next introduce the reflectance, defined as the ratio of reflected power to the incident power, which can be written as

$$R = \left(\frac{E_{0r}}{E_{0i}} \right)^2 = r^2. \tag{3.29}$$

As well, we introduce the transmittance (simply) for completeness. This equation (and its subsequent extreme values) is not explicitly used in this discussion or in the base algorithm; however, some MC models of light propagation in tissue do incorporate these ratios in checks and further calculations. The transmittance itself is (similar to the reflectance) defined as the ratio of transmitted power to the incident power, which can be written (in an alternative manner to that previously used in Equation 3.12, though conceptually the same):

$$T = \frac{n_t \cos(\theta_t)}{n_t \cos(\theta_i)} \left(\frac{E_{0t}}{E_{0i}} \right)^2 = \left(\frac{n_t \cos(\theta_t)}{n_t \cos(\theta_i)} \right) t^2. \tag{3.30}$$

Here, r and t are again the amplitude reflection and transmission coefficients (though note that the direction of the electric field is not specified), while E_0 represents the amplitude of the electric field and the further subscripts denote incident, reflected, or transmitted values. As the direction of $\vec{\boldsymbol{E}}$ is not specified in Equations 3.29 and 3.30, it follows that

$$R_\perp = r_\perp^2, \tag{3.31}$$

$$R_\parallel = r_\parallel^2, \tag{3.32}$$

$$T_\perp = \frac{n_t \cos(\theta_t)}{n_t \cos(\theta_i)} t_\perp^2, \tag{3.33}$$

$$T_\parallel = \frac{n_t \cos(\theta_t)}{n_t \cos(\theta_i)} t_\parallel^2. \tag{3.34}$$

In other words, if the electric field is oriented in one of the directional extremes, the reflectance and transmittance adjust accordingly.

Lastly, it is known for ordinary light which is "unpolarized" (such as assumed for our purposes) that half oscillates parallel to the plane-of-incidence and half oscillates perpendicular to that plane — i.e., there is an equal amount of power (or intensity) in two opposite linear polarizations [Prakash and Chandra, 1971]. Hence, it can be shown (e.g., in Hecht [2001]) that the total reflectance for such natural, unpolarized light is

$$R = \frac{1}{2}\left(R_{\perp} + R_{\parallel}\right), \tag{3.35}$$

and this is what we require for the determination of our boundary interactions.

3.3.3.4 Boundary Interactions in Practice

As we are aware, a photon packet may interact with a boundary during its step. We now consider the procedures involved with evaluating this occurrence and determining what the outcome is for the interaction.

The first instance of a boundary interaction during a simulation generally occurs immediately after launching: assuming we have launched the photons above the first layer of skin, this provides the first boundary (so long as there is a mismatch of indices of refraction). Generally, the light is shone so that photon packets are launched orthogonally onto the skin — hence, $\theta_i = \theta_t = 0$. Thus, by using Equations 3.25, 3.27, 3.31, 3.32, and 3.35, we are left with the reflectance as

$$R_{sp} = \left(\frac{n_i - n_t}{n_i + n_t}\right)^2, \tag{3.36}$$

in the case of normal incidence ($\theta_i = \theta_t = 0$), where we have here used the label R_{sp} to emphasise that this is specular reflectance (as opposed to diffuse). Recalling that this represents the ratio of reflected power to the incident power, we see that R_{sp} of the photon's weight is reflected, while the remainder is transmitted across the boundary. Hence, the photon packet's weight is altered as thus upon entering the second medium (noting $W_0 = 1$ at launch):

$$W = (1 - R_{sp})\,W_0. \tag{3.37}$$

Further propagation of a photon packet may result in the crossing of additional boundaries, such as those between individual tissue layers or an exit boundary (tissue-air, for example). Consequently, we now consider the process for handling this crossing.

First, we must calculate how far the nearest boundary is in the photon's direction. In this discussion, we simply consider planar interfaces between mediums (see Section 2.6 for a discussion on incorporating non-planar boundaries). From our direction cosines, we have u_z describing the orientation of the photon's trajectory in the z-direction. Specifically, we note that this value can be greater than, less than, or equal to zero depending on the photon's orientation. Hence, for our planar interfaces, we can determine the distance to the appropriate boundary, d_b, during each step as follows:

$$d_b = \begin{cases} \dfrac{z_0 - z}{u_z} & \text{for} \quad u_z > 0, \\ \infty & \text{for} \quad u_z = 0, \\ \dfrac{z_1 - z}{u_z} & \text{for} \quad u_z < 0. \end{cases} \tag{3.38}$$

Here, we have used z to represent the position of the photon in the z-direction, z_0 to represent the z-value of the current layer's upper boundary, and z_1 for the current layer's lower boundary. In determining these values, one can consider the simple trigonometry of the situation with two planar layers separated by a given distance and connected diagonally by a line at an angle of θ.

Next, we must compare the determined distance to the step size (i.e., d_b to s_1). If the distance is greater than the step size, the photon packet is moved to its next interaction site (it takes the step of size s_1) and the interactions undertaken in Sections 3.4 and 3.5 are completed. If the distance is less than the step size, the photon packet will cross the appropriate boundary. Hence, we move the photon to the boundary, and we shall next proceed to determine the specular reflectance via use of the methods discussed in Sections 3.3.3.1, 3.3.3.2, and 3.3.3.3.

In order to determine the reflectance (via Equation 3.35), we require the angle of incidence (θ_i) and the angle of transmission (θ_t). We can determine

θ_i as

$$\theta_i = \cos^{-1}(|u_z|), \tag{3.39}$$

while θ_t can then be computed via Snell's law (Equation 3.21).

We next recall the optical phenomenon of total internal reflection, in which a ray of light travelling from a medium of relatively high index of refraction is incident on a boundary between the present medium and another of relatively low index of refraction at an angle of incidence greater than a threshold known as the critical angle (θ_c, at which the refracted ray becomes parallel to the interface — i.e., $\theta_r = 90°$). When these conditions are met, there is no refraction of the ray into the second medium. Rather, the ray is completely reflected back into the incident medium. Thus, if $n_i > n_t$ and $\theta_i > \sin^{-1}\left(\frac{n_t}{n_i}\right)$, we set the local reflectance, $R_i(\theta_i)$, equal to unity in this situation.

When the conditions for total internal reflection are not met, we calculate the local reflectance via Equation 3.35, written here in its full form:

$$R_i(\theta_i) = \frac{1}{2}\left(\frac{\sin^2(\theta_i - \theta_t)}{\sin^2(\theta_i + \theta_t)} + \frac{\tan^2(\theta_i - \theta_t)}{\tan^2(\theta_i + \theta_t)}\right). \tag{3.40}$$

Again, we note that this assumes the light to be randomly polarized (i.e., unpolarized for our purposes).

Next, a pseudorandom number is generated and compared with $R_i(\theta_i)$ to decide whether the photon packet is reflected or transmitted. That is, if the number is less than or equal to $R_i(\theta_i)$, the packet is reflected. If not, it is transmitted.

In the event of reflection, the packet remains on the boundary; however, its direction is updated to represent the reflection by simply reversing the z-component — i.e., $u_z \to -u_z$. This follows from the law of reflection, Equation 3.22. The photon packet then attempts to complete the remainder of its initial step ($s_1 - d_b$ here), though the procedures described above for checking boundary distances and so forth must be completed again in case the packet will cross another boundary during the remainder of its step. This reversal of z-component and continuation with propagation is also the process for the case of total internal reflection. The photon continues through this cycle until it is able to complete its step.

In the event of transmission, we need to update the photon's direction and step size after the boundary. First, we update the direction cosines as follows:

$$u'_x = \frac{\sin(\theta_t)}{\sin(\theta_i)} u_x, \tag{3.41}$$

$$u'_y = \frac{\sin(\theta_t)}{\sin(\theta_i)} u_y, \tag{3.42}$$

$$u'_z = \operatorname{sgn}(u_z) \cos(\theta_t), \tag{3.43}$$

where the first two updated direction cosines follow from applying Snell's law and considering (for example) Figure 3.13, while the third is also evident from the same visualization.

Next, we must update the step size. This is done by taking the remaining (dimensionless) step size after moving to the boundary ($(s_1 - d_b)\mu_{ti}$) and converting it to the corresponding step size in the second medium, taking into account the different optical properties. Thus, the remaining step size is now

$$s' = \frac{(s_1 - d_b)\mu_{ti}}{\mu_{tt}}, \tag{3.44}$$

where we here use μ_{ti} and μ_{tt} to respectively represent the attenuation coefficients for the incident and transmitted mediums. The photon packet then attempts to complete the remainder of its step, though we again must check the boundary distance in the new medium along the packet's trajectory. If there is another boundary crossing along this trajectory, the processes described above repeat, and this continues until the packet can complete its current step without any further boundary crossings.

3.4 Drop

When a photon packet has completed an entire step, it reaches an interaction site. With the way in which we have defined the propagation step size, the packet is now forced to undergo an interaction, and the standard way to complete this is to force the entire packet to experience both scattering and absorption [Wang and Wu, 2007]. Hence, at this point, there are two processes that must be undertaken. First, a portion of the packet's weight must be "dropped" at the site to represent photon absorption, while the remaining portion of the packet is then scattered. Here, we outline the "Drop" part of the routine.

At this stage, it is useful to introduce a further parameter known as the albedo, a:

$$a = \frac{\mu_s}{\mu_a + \mu_s} = \frac{\mu_s}{\mu_t}. \tag{3.45}$$

Evidently, this parameter describes the ratio of scattering to attenuation (i.e., scattering to the sum of absorption and scattering), and has a value ranging from zero to one. Zero corresponds to an absence of scattering, while one corresponds to a non-absorbing medium (in terms of light, at least). As a result, we can determine that the proportion of the packet lost to absorption at the interaction site is $(1-a) = \frac{\mu_a}{\mu_t}$. Consequently, a fraction of the packet's weight is dropped due to absorption, so that the new weight for the packet becomes

$$W_1 = W_0 - W_0(1-a) = aW_0, \tag{3.46}$$

where we have used W_0 and W_1 to refer to the previous and updated weights, respectively. This remaining portion of the packet is then scattered into a new direction.

Here, it is pertinent to note one of the benefits to utilising photon packets with assigned weights. If we had simply used individual photons, each interaction site could result in the photon being completely absorbed according to the probability of absorption. Hence, with this implicit capture technique, we are able to gain absorption information at each stage of the photon's propagation, as opposed to only receiving it at times when the photon is completely absorbed. Similarly, if the photon packet has travelled a large distance already, this means a not insignificant amount of computation has gone into its propagation towards a region of potential interest. Having these packets then be absorbed in a single interaction may make redundant the work undertaken to move them there in the first place. Further discussion on these benefits can be seen in (for instance) Prahl [1988].

3.5 Spin

At this stage, the photon packet has been moved to its next interaction site, its weight has been decreased according to the amount lost due to absorption, and all that remains is for the packet to undergo scattering into a new direction before the process essentially repeats again. As briefly discussed in Section 2.4, this scattering process ("Spin") is commonly performed through use of the Henyey-Greenstein function, which we here look to discuss and motivate the use of in this model.

3.5.1 Scattering: Rayleigh and Mie

Light scattering in tissue occurs when the tissue exhibits fluctuations in its index of refraction [Welch and van Gemert, 2011], which can be interpreted as meaning the tissue's macro-structure consists of smaller individual structures. In particular, photons are scattered most strongly by structures with sizes that match the wavelength of the photon. Typically, in tissue, we consider two types of scattering. As tissue ultrastructure consists of many constituents (e.g., cells, mitochondria, membranes, etc.), there are instances where these structures are smaller than the photon wavelength and other cases where the spatial fluctuations are on the order of (or larger than) the wavelength of light. In this section, we briefly outline these two cases, though a more comprehensive, theoretical/derivational discussion is outside the scope of this document. For a more theoretical consideration, see (for example) van de Hulst [1981].

First, the instance where light is scattered by a structure much smaller than the photon wavelength corresponds to Rayleigh scattering ($r \ll \lambda$, where

r represents the particle's characteristic size and λ is here the wavelength of light). This occurs, for instance, during interactions between (visible or infrared) light and striations (ridges) in collagen fibrils [Jacques and Prahl, 1998e]. In contrast, when the spatial scale of the structure (particle) is on the order of — or larger than — the wavelength of visible/infrared light, the scattering is referred to as Mie scattering. As an example, this type of scattering occurs during interactions between photons and mitochondria [Jacques and Prahl, 1998e]. In fact, it can be shown that the Mie theory also extends to scattering by small particles, as the scattering theory reduces to that of Rayleigh for $r \ll \lambda$ [Welch and van Gemert, 2011]. Hence, as Rayleigh scattering is typically not applicable to the particles we consider in skin tissue — and its regime is covered in the limit by Mie theory — Rayleigh scattering is not heavily utilised in MC models of light propagation in tissue.

Mie scattered light is generally more forward-directed after scattering. As a result, because we know that skin tissue is also forward-scattering [Tuchin, 2007] and it consists of many particles with characteristic size on the order of the wavelength of visible or infrared light, Mie theory can provide a phase function to use in determining the scattering angle from scattering interactions in tissue [Wang and Wu, 2007].

It is not common in contemporary research, however, to use Mie theory in MC tissue optics simulations. Rather, the ability to determine the scattering distribution through the Henyey-Greenstein function by simply adjusting g for the medium (as discussed in Section 2.4) provides one clear incentive to switch from a Mie phase function. In addition, this alternative phase function matches well with empirical results, as will be discussed in the following section.

3.5.2 The Henyey-Greenstein Phase Function

We have previously noted that astrophysics researchers devised an expression in 1941 which could be used to mimic interstellar scattering — specifically, that of light by interstellar dust clouds [Henyey and Greenstein, 1941]. Also noted was that Jacques et al. [1987] were subsequently the first researchers within the field of MC simulations of photon propagation through tissue to make use of this so-called Henyey-Greenstein (H-G) phase function. Prior to this, Wilson and Adam [1983] (for example) had modelled the scattering entirely via an isotropic distribution, which we now know is not appropriate for tissue. Subsequently, however, in conducting *in vitro* tissue studies involving the measurement of the radiant intensity of scattered light as a function of the angle of exitance from the tissue, Jacques et al. [1987] found the data to be conveniently represented by the H-G function. Due to this convenience, the field has continued to make heavy use of the H-G function in further research.

It should be noted, however, that the H-G function was not necessarily chosen for its initial purpose in a manner that was based upon a mechanistic theory of scattering; rather, Henyey and Greenstein [1941] pointed out that the function was selected to approximate Mie scattering, wherein the diameter of a scattering particle is comparable in size with the wavelength of the incident light. This is ideal for skin tissue, as scattering in skin tissue is predominantly in the form of Mie scattering. Accordingly, it is perhaps clearer as to why this function is heavily utilised in MC simulations for skin tissue — alongside its outlined benefits, it also approximates the otherwise relatively useful Mie theory well. Hence, in accordance with common practice at this time, we will proceed with using the H-G function.

3.5.2.1 The H-G Function - Theoretical Background

If we next consider our photon packet to be undergoing a collision at the interaction site, it is clear to see that (in determining its new propagation direction) two angles must be sampled. For reference, see Figure 3.15. First, the deflection angle ($0 \leq \theta \leq \pi$) is calculated, which determines how the photon packet is deflected from its current trajectory. Second, the azimuthal angle ($0 \leq \psi < 2\pi$) is calculated, which determines the rotation around the axis governing the initial direction of propagation in the figure.

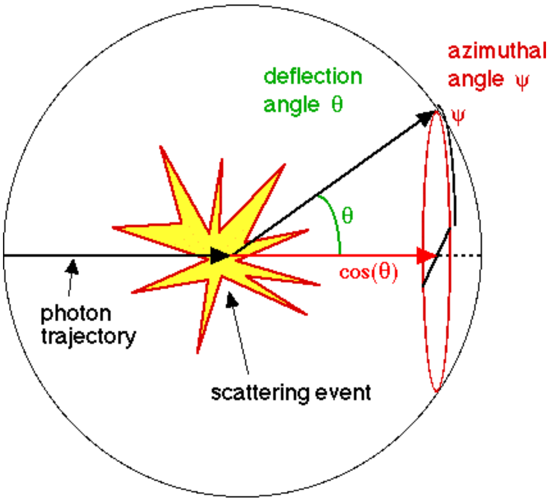

Figure 3.15: A cartoon illustration of the scattering event and involved geometries. Image credit: Jacques and Prahl [1998b].

The azimuthal angle is determined relatively simply, due to the assumption that it is uniformly distributed over the interval. With a pseudorandom number, ξ, between 0 and 1, we have

$$\psi = 2\pi\xi. \tag{3.47}$$

For the deflection angle, we must weight the distribution in accordance with what would be expected in practice. Thus, we finally introduce the Henyey-Greenstein phase function:

$$p(\theta) = \frac{1}{4\pi}\frac{1-g^2}{(1+g^2-2g\cos(\theta))^{\frac{3}{2}}}, \tag{3.48}$$

where we recall that g here is the anisotropy factor (see Section 3.1.3) which characterises the angular distribution of the scattering and the consequential shape of the scattering function. As well, we can see that this function is normalised so that the integral over 4π steradians is equal to unity:

$$\int_0^{2\pi}\left[\int_0^{\pi} p(\theta)\sin(\theta)\mathrm{d}\theta\right]\mathrm{d}\phi = 1. \tag{3.49}$$

This can be shown, for instance, via a u-substitution, with $u = 1+g^2-2g\cos(\theta)$ and $\mathrm{d}u = 2g\sin(\theta)\mathrm{d}\theta$. We also note here that the additional factor of $\sin(\theta)$ is the spherical Jacobian required for integration over the unit sphere. Likewise, we see through a similar series of substitutions that

$$\int_0^{2\pi}\left[\int_0^{\pi} p(\theta)\cos(\theta)\sin(\theta)\mathrm{d}\theta\right]\mathrm{d}\phi = g. \tag{3.50}$$

This final equation serves as a definition for the anisotropy, g, which we previously noted was the mean value of $\cos(\theta)$ (in Section 3.1.3). Hence, the H-G phase function is also an identity function: if we pick a value of g to define $p(\theta)$ through Equation 3.48, the calculation of the expected value of g through Equation 3.50 will return that precise value of g.

In practice, the H-G phase function is often written in an alternate manner to allow for relatively simple computation of the scattering angle without computationally expensive calls to trigonometric functions. This can be achieved by writing the function in terms of $\cos(\theta)$ and normalising so that the total probability of scattering a photon in any direction is equal to 1:

$$\int_{-1}^{1} p(\cos(\theta))\mathrm{d}(\cos(\theta)) = 1. \tag{3.51}$$

Substituting $p(\cos(\theta))$ into the integral, we have:

$$\int_{-1}^{1}\frac{1}{4\pi}\frac{1-g^2}{(1+g^2-2g\cos(\theta))^{\frac{3}{2}}}\mathrm{d}(\cos(\theta)) = 1, \tag{3.52}$$

which can be evaluated by use of a substitution such as $u = 1+g^2-2g\cos(\theta)$ and $\frac{\mathrm{d}u}{\mathrm{d}(\cos\theta)} = -2g$. Applying these substitutions to the integral, we are left with

$$\begin{aligned}\int_{-1}^{1} p(\cos(\theta))\mathrm{d}(\cos(\theta)) &= \int_{-1}^{1}\frac{1}{4\pi}\frac{1-g^2}{u^{\frac{3}{2}}}\frac{\mathrm{d}u}{-2g}\\ &= -\frac{(1-g^2)}{8\pi g}\int_{-1}^{1}\frac{\mathrm{d}u}{u^{\frac{3}{2}}}\\ &= \frac{(1-g^2)}{4\pi g}\left[\frac{1}{\sqrt{u}}\right]_{\cos(\theta)=-1}^{\cos(\theta)=1}\\ &= \frac{(1-g^2)}{4\pi g}\left[\frac{1}{1-g}-\frac{1}{1+g}\right]\\ &= \frac{1}{2\pi}. \end{aligned} \tag{3.53}$$

Because this integral does not equal 1 as we had intended above, we must adjust the normalisation factor ($\frac{1}{4\pi}$). Adjusting this to $\frac{1}{2}$ results in the appropriate integral outcome, and we hence have the following commonly used variation of the Henyey-Greenstein phase function:

$$p(\cos(\theta)) = \frac{1}{2}\frac{1-g^2}{(1+g^2-2g\cos(\theta))^{\frac{3}{2}}}. \tag{3.54}$$

Here, we now have normalisation such that the integral over all values of $\cos(\theta)$ is equal to unity:

$$\int_{-1}^{1} p(\cos(\theta))\mathrm{d}(\cos(\theta)) = 1. \tag{3.55}$$

Again, the anisotropy parameter is defined through this definition in a similar manner:

$$\int_{-1}^{1} p(\cos(\theta))\cos(\theta)d(\cos(\theta)) = g. \tag{3.56}$$

This can be seen as another way to view g as the mean value of $\cos(\theta)$, as we know that $\int_{-1}^{1} p(\mu)\mu d\mu = \langle\mu\rangle$ for μ distributed in the interval $[-1, 1]$.

3.5.3 Sampling the H-G Function

To determine the specific deflection angle for a scattering interaction, θ, we need to sample Equation 3.54. In doing so, we recall Equation 3.16 from our inverse distribution method, repeated below:

$$\int_{a}^{\chi} p(\chi)d\chi = P(\chi) = \xi. \tag{3.16}$$

Applying this to Equation 3.54, where now $\chi = \cos(\theta)$, we have

$$\xi = \int_{-1}^{\chi} \frac{1}{2}\frac{1-g^2}{(1+g^2-2g\cos(\theta))^{\frac{3}{2}}}d\chi, \tag{3.57}$$

which is solved to give

$$\chi = \frac{1}{2g}\left[1+g^2-\left(\frac{1-g^2}{1-g+2g\xi}\right)^2\right]. \tag{3.58}$$

Evidently, this is only valid for $g \neq 0$ — that is, as g approaches zero, this equation approaches an undefined value. We know, however, that the limit as g approaches zero corresponds to a scattering function shape that approaches isotropic scattering (by the definition of g, from Section 3.1.3). Hence, by setting $g = 0$ in Equation 3.54, we see that $p(\chi) = \frac{1}{2}$. Thus, by again applying Equation 3.16, we find

$$\begin{aligned} \xi &= \int_{-1}^{\chi} \frac{1}{2} d\chi && (3.59) \\ &= \frac{1}{2}\left(\chi + 1\right). && (3.60) \end{aligned}$$

Solving this equation for χ, we have

$$\chi = 2\xi - 1, \tag{3.61}$$

which is the case for $g = 0$.

Consequently, to summarise, we sample $\cos(\theta)$ according to the following conditions:

$$\chi = \cos(\theta) = \begin{cases} \dfrac{1}{2g}\left[1 + g^2 - \left(\dfrac{1-g^2}{1-g+2g\xi}\right)^2\right] & \text{for} \quad g \neq 0, \\ 2\xi - 1 & \text{for} \quad g = 0, \end{cases} \tag{3.62}$$

where the actual deflection, θ, of the packet is given by $\cos^{-1}(\chi)$.

3.5.4 Updating the Trajectory

The last step of the "Spin" stage, then, is to update the global trajectory of the photon packet according to the newly determined local deflection angle, θ, and local azimuthal angle, ψ. In doing so, we utilise two rotation matrices to develop equations that allow us to write the new direction in terms of the old direction. By first referring to Figure 3.16, we can quickly show through simple trigonometric manipulation that a rotation about the z-axis (here represented by the rotation angle ψ) relates the original coordinates and the new coordinates by the following rotation matrix:

$$\begin{pmatrix} x \\ y \\ z \end{pmatrix} = \begin{pmatrix} \cos(\psi) & -\sin(\psi) & 0 \\ \sin(\psi) & \cos(\psi) & 0 \\ 0 & 0 & 1 \end{pmatrix} \begin{pmatrix} x' \\ y' \\ z' \end{pmatrix} \equiv \boldsymbol{R}_z(\psi) \begin{pmatrix} x' \\ y' \\ z' \end{pmatrix} \tag{3.63}$$

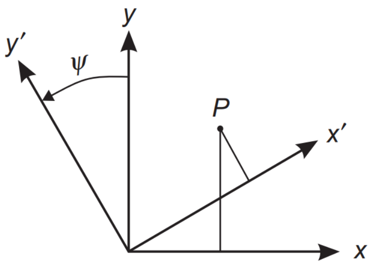

Figure 3.16: Diagram showing a positive rotation about the z-axis. Image credit: Dunn and Shultis [2012].

Similarly, if we then rotate this rotated coordinate system about the newly formed y'-axis by an angle θ (as can be seen in Figure 3.17), we can quickly show that the initially rotated coordinates are related to these newly rotated coordinates by the following rotation matrix:

$$\begin{pmatrix} x' \\ y' \\ z' \end{pmatrix} = \begin{pmatrix} \cos(\theta) & 0 & \sin(\theta) \\ 0 & 1 & 0 \\ -\sin(\theta) & 0 & \cos(\theta) \end{pmatrix} \begin{pmatrix} x'' \\ y'' \\ z'' \end{pmatrix} \equiv \boldsymbol{R}_y(\theta) \begin{pmatrix} x'' \\ y'' \\ z'' \end{pmatrix} \tag{3.64}$$

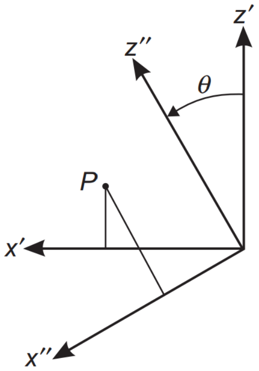

Figure 3.17: Diagram showing a positive rotation about the y'-axis. Image credit: Dunn and Shultis [2012].

Consequently, if we combine these two rotations, we find that

$$\begin{pmatrix} x \\ y \\ z \end{pmatrix} = \begin{pmatrix} \cos(\theta)\cos(\psi) & -\sin(\psi) & \sin(\theta)\cos(\psi) \\ \cos(\theta)\sin(\psi) & \cos(\psi) & \sin(\theta)\sin(\psi) \\ -\sin(\theta) & 0 & \cos(\theta) \end{pmatrix} \begin{pmatrix} x'' \\ y'' \\ z'' \end{pmatrix}, \tag{3.65}$$

which gives our rotation matrix as

$$\boldsymbol{R}_{zy}(\theta,\psi)=\boldsymbol{R}_z(\psi)\boldsymbol{R}_y(\theta)=\begin{pmatrix}\cos(\theta)\cos(\psi) & -\sin(\psi) & \sin(\theta)\cos(\psi)\\ \cos(\theta)\sin(\psi) & \cos(\psi) & \sin(\theta)\sin(\psi)\\ -\sin(\theta) & 0 & \cos(\theta)\end{pmatrix}. \tag{3.66}$$

By then considering a photon packet (as shown in Figure 3.18) moving in the direction given by $\boldsymbol{\Omega}(u_x,u_y,u_z)=(\sin(\theta)\cos(\psi),\sin(\theta)\sin(\psi),\cos(\theta))$, we seek to calculate its new direction, $\boldsymbol{\Omega'}(u'_x,u'_y,u'_z)$, after deflecting through the angle shown as θ_s and into an azimuthal angle of ψ'.

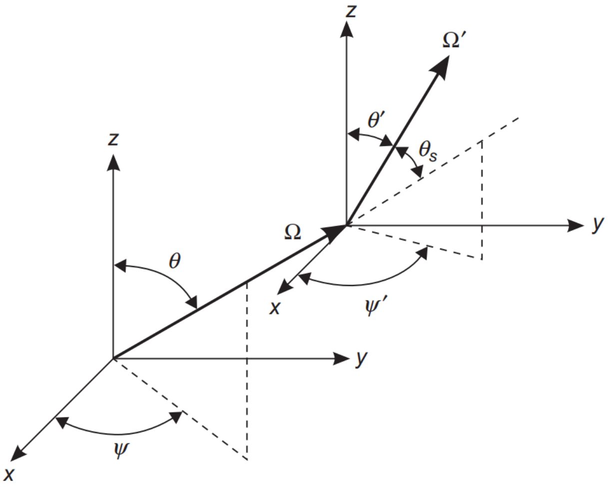

Figure 3.18: Diagram showing the relation between the coordinates of a packet before and after scattering. Image credit: Dunn and Shultis [2012].

The calculation of the new direction can be summarised as consisting of three steps. First, we rotate $\boldsymbol{\Omega}$ to a local coordinate system in which the vector lies on the z-axis. Evidently, this can be done by noting $\boldsymbol{R}_{zy}^{-1}(\theta,\psi)\boldsymbol{\Omega}=(0,0,1)$. Second, we take the transformation given by $\boldsymbol{R}_{zy}(\theta_s,\psi')(0,0,1)$, which will produce a vector in the local coordinate system with direction cosines given by our scattering angles from Figure 3.18, (θ_s,ψ'). Lastly, we take this scattered vector and rotate it back into our original coordinate system with our previously defined rotation matrix, $\boldsymbol{R}_{zy}(\theta,\psi)$. Hence, the direction of our scattered photon packet becomes

$$\boldsymbol{\Omega'}(u'_x, u'_y, u'_z) = \boldsymbol{R}_{zy}(\theta, \psi)\boldsymbol{R}_{zy}(\theta_s, \psi')\boldsymbol{R}^{-1}_{zy}(\theta, \psi)\boldsymbol{\Omega}. \tag{3.67}$$

We then wish to relate our new direction cosines to those previously calculated in order to define a recursive process for our simulation. Hence, we rewrite the transformation matrix given in Equation 3.66 through use of our previously defined direction cosines, $(u_x, u_y, u_z) = (\sin(\theta)\cos(\psi), \sin(\theta)\sin(\psi), \cos(\theta))$, giving

$$\boldsymbol{R}_{zy}(\theta, \psi) = \begin{pmatrix} u_z\cos(\psi) & -\sin(\psi) & u_x \\ u_z\sin(\psi) & \cos(\psi) & u_y \\ -\sin(\theta) & 0 & u_z \end{pmatrix}. \tag{3.68}$$

With this, we can now take the previously determined packet's new direction, Equation 3.67, and determine the following expressions:

$$u'_x = u_x\cos(\theta_s) + \sin(\theta_s)(u_z\cos(\psi)\cos(\psi') - \sin(\psi)\sin(\psi')), \tag{3.69}$$

$$u'_y = u_y\cos(\theta_s) + \sin(\theta_s)(u_z\sin(\psi)\cos(\psi') + \cos(\psi)\sin(\psi')), \tag{3.70}$$

$$u'_z = u_z\cos(\theta_s) - \sin(\theta)\sin(\theta_s)\cos(\psi'). \tag{3.71}$$

In writing these expressions, note that we have recalled $\boldsymbol{R}^{-1}_{zy}(\theta, \psi)\boldsymbol{\Omega} = (0, 0, 1)$, which largely simplifies the working.

Lastly, we can adjust these expressions further to avoid so many calls to trigonometric functions, which will help to improve the efficiency of our simulation. By recognising that $u_x = \sin(\theta)\cos(\psi)$, $u_y = \sin(\theta)\sin(\psi)$, and $\sin(\theta) = \sqrt{1 - u_z^2}$, we can write

$$u'_x = u_x\cos(\theta_s) + \frac{\sin(\theta_s)}{\sqrt{1 - u_z^2}}(u_z u_x\cos(\psi') - u_y\sin(\psi')), \tag{3.72}$$

$$u'_y = u_y\cos(\theta_s) + \frac{\sin(\theta_s)}{\sqrt{1 - u_z^2}}(u_z u_y\cos(\psi') + u_x\sin(\psi')), \tag{3.73}$$

$$u'_z = u_z\cos(\theta_s) - \sqrt{1 - u_z^2}\sin(\theta_s)\cos(\psi'), \tag{3.74}$$

and we now have our new direction cosines to continue the photon packet's propagation. These are then fed back into the "Hop" step for future movements.

One issue that may arise with these expressions is the possibility to have division by zero (or very close to it), which occurs when the photon direction is too close to the z-axis and $u_z \approx 1$. This can occur in instances where the angle is close to the normal. In these instances, we revert to using the following formulas:

$$u'_x = \sin(\theta_s)\cos(\psi'), \tag{3.75}$$

$$u'_y = \sin(\theta_s)\sin(\psi'), \tag{3.76}$$

$$u'_z = \operatorname{sgn}(u_z)\cos(\theta_s). \tag{3.77}$$

In practice, one might set a threshold (such as $|u_z| > 0.99999$) to trigger this condition.

3.6 Terminate

At this point, we have described all the processes necessary to propagate a photon (packet) through our tissue (or general medium). One element remains to be discussed, however, and this concerns the point at which to terminate a photon packet. Clearly, we must put in place conditions that will terminate a packet if it is reflected or transmitted out of the tissue (i.e., if it is reemitted from the tissue). Yet, aside from this, our photon packet presently will continue to propagate as its weight becomes ever smaller with each “Drop” stage of the propagation cycle. We note, however, that its weight will never become zero in our present setup, and if we continue to propagate a packet with a minute weight, we are adding little new information to our solution (unless the packet has propagated to an area of interest with little prior data). Further, we cannot simply absorb or discard the photon’s remaining weight after it falls below a certain threshold, as this will either skew our absorption statistics or violate the law of conservation of energy.

3.6.1 Roulette

The manner in which we overcome this problem is through the use of what is known as a roulette method. This technique requires us to set a weight threshold below which the photon packet undergoes the roulette routine. Typically, one sets a threshold value, W_{th}, equal to 0.0001 [Jacques, 2011]. Reducing this value may improve statistics at greater penetration depths within the tissue, if needed. If the packet's current weight, W_0, is below W_{th}, the packet is given a one chance in k (typically, one chance in ten [Jacques, 2011]) of surviving; however, upon surviving, its weight is altered to $W_1 = kW_0$. If the packet does not survive (a chance of $1 - 1/k$), its weight is reduced to zero and the photon packet is consequently terminated. The updating of the packet's weight is summarised here:

$$W_1 = \begin{cases} kW_0 & \text{if} \quad \xi \leq \dfrac{1}{k}, \\ 0 & \text{if} \quad \xi > \dfrac{1}{k}, \end{cases} \tag{3.78}$$

where we have reused our pseudorandom number, ξ, which is in the interval $[0, 1]$.

We can see that the use of this technique results in the packet being terminated, for instance, nine out of ten times, while the other one time out of ten increases the packet's weight ten-fold. In short, we see that the packets will generally be terminated; however, the few surviving packets conserve energy through their increased weight. With large numbers of photons being simulated, we can see that the statistically averaged result will converge towards the true result. Thus, through use of this technique, we terminate the packet in a manner that is free from bias, our energy conservation is unhindered, and we do not lose efficiency via propagating all photons until their weights reach an extremely small level.

3.6.2 Splitting

A relatively common technique in a similar vein to that discussed above is known as splitting. The purpose of this method is generally to improve statistics in regions of interest. In short, as a packet moves into a designated region of interest (one might pre-assign importances to regions in the code), its weight of W is split into m different packets, with each now having a weight of W/m. Hence, energy is conserved, but the region of interest will gather improved statistics as multiple packets are now considered. This is clearly useful as, for instance, it may be difficult for packets to reach this region, so the splitting aids with this problem.

In addition, the splitting technique can be used in conjunction with the roulette technique, in the sense that regions of lesser importance/interest may initiate a roulette process upon entry by a packet (in contrast to the splitting initiated for regions of interest). One can further adjust the roulette process so it is not focused on packet weight as above, in which case the process is very much in contrast to the splitting technique.

In our initial code, we primarily utilise only the weight-based roulette technique for photon termination; however, this may be altered in future. For further discussion on such variance reduction techniques as those discussed above, see (for example) Hendricks and Booth [1985].

References

W. L. Dunn and J. K. Shultis. 10 - Monte Carlo Simulation of Neutral Particle Transport. In W. L. Dunn and J. K. Shultis, editors, *Exploring Monte Carlo Methods*, pages 269–306. Elsevier, Amsterdam, 2012.

E. Hecht. *Optics, 4th Edition.* Pearson plc, 2001.

J. S. Hendricks and T. E. Booth. MCNP variance reduction overview. In R. Alcouffe, R. Dautray, A. Forster, G. Ledanois, and B. Mercier, editors, *Monte-Carlo Methods and Applications in Neutronics, Photonics and Statistical Physics*, pages 83–92. Springer Berlin Heidelberg, 1985.

L. G. Henyey and J. L. Greenstein. Diffuse radiation in the Galaxy. *The Astrophysical Journal*, 93:70–83, January 1941.

HyperPhysics. Mean Free Path. `http://hyperphysics.phy-astr.gsu.edu/hbase/Kinetic/menfre.html`, 2016.

S. L. Jacques. Monte Carlo Modeling of Light Transport in Tissue (Steady State and Time of Flight). In A. J. Welch and M. J. C. van Gemert, editors, *Optical-Thermal Response of Laser-Irradiated Tissue*, pages 109–144. Springer Netherlands, 2011.

S. L. Jacques and S. Prahl. Definition and units of absorption coefficient μ_a [cm^{-1}]. `https://omlc.org/classroom/ece532/class3/muadefinition.html`, 1998a.

S. L. Jacques and S. Prahl. Definition of anisotropy, g [dimensionless]. `https://omlc.org/classroom/ece532/class3/gdefinition.html`, 1998b.

S. L. Jacques and S. Prahl. Reduced scattering coefficient. `https://omlc.org/classroom/ece532/class3/musp.html`, 1998c.

S. L. Jacques and S. Prahl. Definition and units of scattering coefficient. `https://omlc.org/classroom/ece532/class3/musdefinition.html`, 1998d.

S. L. Jacques and S. Prahl. Some biological scatterers. `https://omlc.org/classroom/ece532/class3/scatterers.html`, 1998e.

S. L. Jacques, C. A. Alter, and S. A. Prahl. Angular dependence of HeNe laser light scattering by human dermis. *Lasers in the Life Sciences*, 1:309–333, 1987.

C. Olson, J. Nichols, C. Villarruel, and F. Bucholtz. On the potential use of evolutionary algorithms for electro-optic system design, 2011.

PhysicsCatalyst. Spherical coordinates system (Spherical polar coordinates). `https://https://physicscatalyst.com/graduation/spherical-coordinates-system/`, 2021.

S. A. Prahl. *Light Transport in Tissue.* PhD thesis, The University of Texas at Austin, 1988.

H. Prakash and N. Chandra. Density operator of unpolarized radiation. *Physical Review A*, 4:796–799, Aug 1971.

V. V. Tuchin. *Tissue Optics*, pages 132–142. SPIE, 2007.

H. C. van de Hulst. *Light Scattering by Small Particles.* Dover Publications, 1981.

L. Wang, S. L. Jacques, and L. Zheng. MCML — Monte Carlo modeling of light transport in multi-layered tissues. *Computer Methods and Programs in Biomedicine*, 47(2):131–146, 1995.

L. V. Wang and H. Wu. *Biomedical Optics: Principles and Imaging.* Wiley, 2007.

A. J. Welch and M. J. C. van Gemert. *Optical-Thermal Response of Laser-Irradiated Tissue.* Springer Netherlands, 2011.

B. C. Wilson and G. Adam. A Monte Carlo model for the absorption and flux distributions of light in tissue. *Medical Physics*, 10(6):824–830, 1983.

Chapter 4

First Paper Motivation

Though the human womb has long been assumed dark (or, at best, negligibly illuminated by external light sources), the precise extent of any such illumination has never been thoroughly explored. Consequently, researchers in fetal visual development fields have no targeted research on which to base the development of transdermal laser diode stimuli for fetal experimentation.

Recent work, however, indicates the human fetus responds to external visual stimuli [Reid et al., 2017], such as laser diodes, and initial modelling has suggested that the fetus may not develop in the completely dark environment previously assumed [Del Giudice, 2011]. Hence, the commonly held belief that the uterine environment is dark must be explored in greater depth to establish, for example, the range of illumination scenarios that the human fetus is exposed to over gestation.

Further, development of the human visual system begins within the womb, and there is motivation in fields such as developmental psychology, transabdominal oximetry, and photoacoustics to explore the extent to which light penetrates maternal abdominal tissue and understand how transdermal stimuli appear to the fetus. This is perhaps most apparent in the work of researchers from the field of fetal vision, where fetal behaviour is often examined via use of transdermal monochromatic stimuli delivered to the fetus through the exterior maternal abdomen [Reid et al., 2017; Reid and Dunn, 2021].

To understand the interactions between laser diode stimuli and maternal tissue, we developed and adapted a Monte Carlo model utilising third trimester histological properties of maternal tissue. This model is used to simulate transdermal monochromatic point light sources delivered to the maternal abdomen with a wavelength of 650 nm (as used in experimental applications), with varying thicknesses of adipose tissue. By adjusting this variable, we begin to understand the relationship between tissue thickness (via adipose thickness variation) and the resultant stimuli delivered to the fetus.

From the simulated outputs, we determine approximate levels of third trimester uterine illumination from such stimuli — with results ranging from being comparable to an overcast night for 2.50 cm of adipose to a full moon in clear conditions for 1.00 cm of adipose. We further discuss the scope for multiple stimuli to be visibly distinct in utero for further experimental applications.

Overall, this modelling provides quantitative guidance on the interactions between transdermal monochromatic point source laser diode stimuli and maternal tissue to practitioners and researchers in the fields of fetal vision, ultrasound, and developmental psychology.

References

M. Del Giudice. Alone in the Dark? Modeling the Conditions for Visual Experience in Human Fetuses. *Developmental Psychobiology*, 53:214–219, 2011.

V. Reid, K. Dunn, R. Young, J. Amu, T. Donovan, and N. Reissland. The Human Fetus Preferentially Engages with Face-like Visual Stimuli. *Current Biology*, 28:824, 03 2017.

V. M. Reid and K. Dunn. The fetal origins of human psychological development. *Current Directions in Psychological Science*, 30(2):144–150, 2021.

Chapter 5

The effect of adipose tissue on transdermal monochromatic light presented to the human fetus using Monte Carlo simulations

5.1 Introduction

Little is known about how the human fetus engages with the visual world. Several studies have shown evidence of fetal sensory stimulation in the uterus through auditory or olfactory stimuli [Bradley and Mistretta, 1975; Lecanuet and Schaal, 1996], yet the presence of uterine visual stimulation from external light sources has been consistently assumed as either absent or negligible [Myowa-Yamakoshi and Takeshita, 2006]. Historically, circumstances allowing for illumination of the uterus were suggested to be limited to cases where the maternal abdomen was exposed directly to a powerful light source [Liley, 1972]. Accordingly, research in the field of fetal visual development has been limited, though some experimental work has suggested there is sufficient light entering the uterine environment of pigs and guinea pigs to allow for fetal visual stimulation [Jacques et al., 1987].

More recently, work exploring the human visual experience prior to birth utilized quantitative modelling to assess the visual environment for the human fetus during the final two months of gestation, with results indicating many fetuses may develop in conditions providing sufficient illumination of the uterine cavity for visual experience [Del Giudice, 2011]. This finding renewed experimental research interest in fetal visual development, with later studies presenting diode light sources to the fetus through the maternal abdomen and concluding that fetuses show a preference for face-like stimuli [Reid et al., 2017].

Subsequent research found that uterine light is essential for the typical formation of the eye in mice [Rao et al., 2013]. This raised the question of whether light was required for all mammalian visual systems during gestation. As it is not ethically appropriate to conduct experiments with humans where the visual system may become impaired, further work explored the impact of naturalistic variation in average day length (hence, natural light exposure) during early human gestation and the associated visual outcomes for infants [Yang et al., 2013]. Findings suggested that there may be impacts to the human visual system from the number of daylight hours.

It is clear that the development of research within the field of fetal vision, combined with our growing knowledge of the uterine visual environment, has indicated the need for targeted research into the levels of light stimuli present within the human uterus across gestation. More generally, such research provides benefit to those working in transabdominal oximetry and photoacoustics through a greater understanding of the effects of tissue components on transdermal light and how stimuli might present to the fetus.

To our knowledge, modelling of light that reaches the human fetus has been limited to four previous forms of approach.

First, perturbation methods have been used to model photon transport through the fetus (a prominent example models transport through the brain [Jacques et al., 2000]); however, researchers in these areas are typically not concerned with uterine illumination or stimuli appearance to the fetus — both of interest in developmental psychology.

Second, general illumination of the uterine cavity has been modeled by measuring light transmission through biological tissue samples and estimating a regression equation [Del Giudice, 2011]. This approach demonstrated that the uterus may be an environment allowing for visual experience under certain conditions, though the method lacked flexibility and offered only an isolated snapshot of the conditions measured with the tissue samples. Any variation in optical tissue properties such as absorption or scattering coefficients would impact the physical processes occurring during light propagation and cause results to deviate from the model's predictions. More thorough modelling is hence needed to develop this work.

Third, in response to claims of fetal preference for face-like stimuli in the womb [Reid et al., 2017], outputs from Monte Carlo (MC) simulations were used to demonstrate the apparent difficulty for the fetus in distinguishing the presented stimuli [Scheel et al., 2018]. This approach explicitly modelled the appearance of transdermal stimuli to the fetus; however, one drawback was the limited application and investigation of the work (though this was not the overall intention of the paper). The authors employed a single instance of a one-layer tissue model and the maternal abdominal tissue was assumed to be homogeneous. In reality, maternal tissue is composed of multiple constituent layers – each with different optical properties – and the assumption of a homogeneous medium may omit impacts due to the varying nature of the tissue across layers. The field would benefit from a deeper investigation of these impacts and the extent to which transdermal stimuli may be used in future fetal visual development studies.

Fourth, in transabdominal fetal monitoring (and similar fields), computational modelling has been employed to simulate light transport to the fetus for observation of fetal wellbeing. For example, various efforts have been made in fetal pulse oximetry to model light transport in maternal tissue; recently, MC simulations were used to determine the effect of amniotic fluid on recovering fetal signals through the maternal abdomen [Gunther et al., 2021]. In this work, researchers utilize a three-layer maternal tissue model and vary the subdermal layer, though their focus (and that of others in these fields) is on aspects not directly related to our interests. Such works also typically explore signals at wavelengths outside the range of those used in experimental fetal vision research, where studies focus on wavelengths that can be perceived by the fetal eye as estimated by newborn capacities.

Further, fetal visual development research currently focuses on the third trimester of pregnancy due to the late development of the fetal eye, with previous research showing the fetal brain responds to light during the third trimester [Donovan et al., 2020] and the fetus moves its eyes at 34 weeks in response to the introduction of transdermal light stimuli on the mother's abdomen [Dunn et al., 2015]. Hence, to further inform and develop these experimental applications, model parameters must be relevant to this stage of pregnancy. No previous research addresses this consideration when modelling how transdermal stimuli appear to the fetus or the levels of uterine illuminance provided.

Inspection of the basic component layers of maternal abdominal tissue (skin, adipose, muscle, and uterus) highlights the primary motivation of this study. From empirical studies [Kennedy et al., 2016; D'Ambrosi et al., 2017; Hwang, 2021], the layer that generally exhibits the greatest thickness and variation in thickness across individuals in their third trimester of pregnancy is adipose tissue. In addition, adipose is the layer which generally has the most profound impact on the propagation of light to the womb. This can be seen by inspection of the optical properties sourced from literature in Table 5.1. It is clear that adipose tissue is highly photon-absorbing relative to other tissue layers, thus more heavily diminishing the levels of light reaching the womb. Similarly, average layer thicknesses taken from empirical studies show adipose tissue thickness in pregnant women to typically vary from 1.0 cm to 2.0 cm

[Kennedy et al., 2016; D'Ambrosi et al., 2017; Hwang, 2021]. In combination with the highly photon-absorbing nature of this tissue, the implication is that adipose plays an important role in determining the levels of light reaching the fetus, and a large amount of uterine light variation across individuals is influenced by variations in adipose tissue.

In order to model the amount of light that reaches a human fetus from the application of monochromatic point source stimuli to the exterior maternal abdomen, we present a computational model developed in C17 standard C that implements a direct particle simulation MC approach to simulate light transport through dynamically dispersive tissue. The model incorporates five layers, with four representing the maternal tissues and one representing the amniotic fluid. All simulations have been run with at least 12 billion photon packets to reduce noise and generate appropriate statistical accuracy. We adjust the model's adipose layer by increasing its thickness, which addresses two aspects of pregnancy. First, across gestation, the structure of maternal abdomen tissue changes in response to the growing size of the fetus — i.e., there is a temporal aspect to consider when determining the illumination of the uterus. Adjusting the thickness of the adipose layer is a simple manner through which to initially explore this evolution. Second, this gives an insight into how body fat indicators may affect the illumination of the womb. For example, mothers with higher BMI values might be expected to have greater adipose tissue thickness, while the converse may be expected for mothers with lower BMI values. Consequently, these simulations highlight the extent to which uterine illumination levels from direct point source stimuli vary across the population with respect to such measures.

We also explore an application to a problem faced by developmental psychologists. As this field seeks to utilize light as a means of displaying distinct light sources to the fetus, such as moving two separate monochromatic point source light stimuli towards one another along the maternal abdomen exterior during presentation to the fetus, constraints require that the light sources as viewed by the fetus remain visibly distinct from one another — i.e., minimal stimuli merging visible to the fetal eye, and with a reduced concern for whether the original shape remains distinct (in contrast to earlier fetal visual work [Reid et al., 2017]). We are interested, then, in exploring the point at which two such stimuli cease to become notably distinct from each other, with conclusions from this work being used to inform experimental design in future research.

Thus, in this paper, we aim to answer the following questions: (a) To what extent does a transdermal monochromatic point light source catered toward fetal visual perceptual parameters illuminate the uterine environment? (b) How does such stimuli present to the fetus? (c) How are these quantities affected by variation in adipose tissue? (d) To what extent does the horizontal separation distance along the maternal abdomen of multiple transdermal monochromatic point source stimuli affect how readily discernible the images are for the fetus?

5.2 Methodology

We use MC computational modelling to simulate the propagation of light from directed transdermal monochromatic point source stimuli through the abdominal tissue of a pregnant woman. No human tissues or samples were involved in this study. Consideration was given to use of the diffusion approximation in modelling; however, its validity is typically limited to situations where the light has been highly scattered [Welch and van Gemert, 2011] or the probability of scattering events is much greater than that of absorption events [Duderstadt and Hamilton, 1976]. With the inclusion of amniotic fluid in our models, the diffusion approximation becomes relatively inaccurate when compared to methods such as MC modelling. Similarly, existing applications such as NIRFAST [Dehghani et al., 2009; Jermyn et al., 2013], which are dependent on diffusion approximations, may become less effective for our intended uses in modelling maternal tissue environments. This can be further reasoned due to our close source proximity to the region of interest and the potential for future use of wavelengths outside the near-infrared wavelength range.

All simulations are completed with model parameters relevant to the third trimester of pregnancy, as this is the optimum period for studying the development of the fetal eye via directed light stimuli [Donovan et al., 2020; Dunn et al., 2015]. To run the simulations, we developed a computational model written in C17 standard C that follows a similar algorithm to that employed by the prominent Monte Carlo for Multi-Layered media (MCML) [Wang et al., 1995] model to run direct particle MC simulations. The primary reason for developing our own model was to incorporate aspects for computational efficiency (such as MPI) and to allow for streamlined customization related to our research group's applications in future work.

Our environmental model for this work is split into five layers: four representing the maternal tissues and one representing the amniotic fluid. We have identified and incorporated relevant layer-dependent optical properties and thicknesses for our purposes. These are listed in Table 5.1. As our investigation involves exploring the attenuated stimuli for the third trimester of pregnancy, the layer thicknesses are taken from literature relevant to pregnant women in this stage.

To replicate the differences in tissue structure across individuals, we adjust the thickness of adipose tissue used in the model — the simulations use adipose thicknesses of 1.0 cm, 1.5 cm, 2.0 cm, and 2.5 cm. All other parameters are held constant. Future experimental investigations by our group will deliver laser diode lights direct to the mother's skin, and the wavelength to be employed is 650 nm. All simulations hence use optical parameters taken from literature for this value (see Table 5.1).

5.2.1 The Monte Carlo Model

The model follows a similar algorithm to that of MCML [Wang et al., 1995]. An input file describing the layers, their parameters, the beam, and several

Table 5.1: Layer properties of the tissue model used in Monte Carlo simulations. All values are sourced directly from literature for 650 nm where possible, and emphasis is placed on using values relevant to women in the third trimester of pregnancy (or those that most accurately represent this situation).

Layer	**Medium**	μ_a **[cm^{-1}]**	μ_s **[cm^{-1}]**	**g**	**n**	**t[cm]**
A	Skin	0.14[1]	90.08[1]	0.90†	1.40†	0.20[1,‡]
B	Adipose	0.70[3]	126.00[3,4]	0.90	1.40	1.00-2.50[5,6,7,§]
C	Muscle	1.20[4]	89.00[4]	0.90	1.40	0.48[8]
D	Uterus	0.35[9,10]	137.00[9,10]	0.90	1.40	0.60[11],¶
E	Amniotic fl.	0.003[2]	1.00[12]	0.99[2]	1.35[2]	25.00*

[1] Torricelli et al. [2001]

[2] Scheel et al. [2018]

[3] Bashkatov et al. [2005]

[4] Simpson et al. [1998]

[5] Kennedy et al. [2016]

[6] D'Ambrosi et al. [2017]

[7] Hwang [2021]

[8] Fukano et al. [2021]

[9] Marchesini et al. [1989]

[10] Ripley et al. [1999]

[11] Durnwald and Mercer [2008]

[12] Gunther et al. [2021]

† These values are used for all tissue layers — i.e., all except amniotic fluid. They are commonly found within ranges of those seen in literature [Scheel et al., 2018; Torricelli et al., 2001; Meglinski and Matcher, 2002; Bashkatov et al., 2005; Simpson et al., 1998].

‡ This value is increased from 0.18 to 0.20 in order to fit our voxel gridding.

§ This range also covers a large component of that seen in our experimental work.

¶ This value is decreased from 0.61 to 0.60 in order to fit our voxel gridding.

* Simply chosen to provide a large packet propagation area.

further simulation variables is read and a voxelated tissue region is generated to match the tissue's physical description. Though this is not a new approach to simulating light propagation in tissue, it allows for simple manipulation of the tissue to account for its heterogeneous nature. Hence, this voxelated approach is chosen to allow for future adaptation of the model to account for heterogeneity across the tissue of individuals. This will also enable the delivery of a consistent light source at the individual level for future experimental studies.

Photons are launched as packets with random, medium-specific path lengths and their propagation through to a tissue interaction site is simulated. The source is set as a single collimated photon beam launched orthogonally into the tissue at its surface. We use the Henyey-Greenstein [Henyey and Greenstein, 1941] phase function to model the distribution of deflection angles in scattering:

$$p(\theta) = \frac{1}{4\pi}\frac{1-g^2}{(1+g^2-2g\cos(\theta))^{\frac{3}{2}}}, \tag{5.1}$$

while the azimuthal angle is sampled from a uniform distribution across the interval 0 to 2π. If the step of a packet will cross a boundary between tissue sublayers, transmission is determined by comparing a random number to the internal reflectance as computed by the Fresnel equations [Smith, 2013]:

$$r_\perp = -\frac{\sin(\theta_i-\theta_t)}{\sin(\theta_i+\theta_t)} \tag{5.2}$$

$$t_\perp = +\frac{2\sin(\theta_t)\cos(\theta_i)}{\sin(\theta_i+\theta_t)} \tag{5.3}$$

$$r_\parallel = +\frac{\tan(\theta_i-\theta_t)}{\tan(\theta_i+\theta_t)} \tag{5.4}$$

$$t_\parallel = +\frac{2\sin(\theta_t)\cos(\theta_i)}{\sin(\theta_i+\theta_t)\cos(\theta_i-\theta_t)}. \tag{5.5}$$

This is a common method employed in MC models (for example, see MCML [Wang et al., 1995]). In short, the above equations can be manipulated to give the local reflectance [Hecht, 2001]:

$$R_i(\theta_i) = \frac{1}{2}\left(\frac{\sin^2(\theta_i-\theta_t)}{\sin^2(\theta_i+\theta_t)} + \frac{\tan^2(\theta_i-\theta_t)}{\tan^2(\theta_i+\theta_t)}\right), \tag{5.6}$$

where θ represents the angle of incidence or transmission depending on the subscript.

For the MC method, a pseudorandom number is generated and compared with $R_i(\theta_i)$ to decide whether the photon packet is reflected or transmitted. If the packet is internally reflected, its trajectory component perpendicular to the surface is reversed and it continues propagation in the current layer. If the packet is transmitted, its direction is updated according to the new layer's parameters and its propagation continues. This process repeats until the packet's weight reaches a predetermined lower bound and its termination is handled by a roulette process [Dunn and Shultis, 2012]:

$$W_1 = \begin{cases} kW_0 & \text{if} \quad \xi \leq \frac{1}{k} \\ 0 & \text{if} \quad \xi > \frac{1}{k}, \end{cases} \tag{5.7}$$

where k is typically chosen as 0.1 [Jacques, 2011], W_0 is the photon's current weight, W_1 is the updated weight, and ξ is a pseudorandom number in the interval $[0, 1]$.

The procedures are looped through until all packets have been simulated to their completion. At this stage, output data is written to a file which is read into Matlab scripts to generate images. For our later inspection of multiple beams, as the system used in these simulations is linear and invariant, we may simply shift the beam horizontally and sum the two response grids [Wang et al., 1997]. This component of the research is also handled by Matlab scripts before generating outputs.

To improve the model's computational efficiency, we incorporate parallel processing of photon trajectories. This is accomplished through use of the Message Passing Interface (MPI) standard, allowing faster processing of the 12 billion packages simulated per run. Data generated was benchmarked during model development against that produced by established models (such as MCML [Wang et al., 1995]) and found to be in good agreement. All simulations were conducted with 0.04 cm voxels.

5.2.2 Tissue Model

We employ a four-layer tissue model for our simulations, consisting of skin, adipose, muscle, and uterus. Below the uterus layer is amniotic fluid. A z-plane cross-section of the tissue model used in our simulations is shown in Figure 5.1. As the experimental stimuli to be used will have a wavelength of 650 nm, optical parameters are sourced for this value. These are shown in Table 5.1.

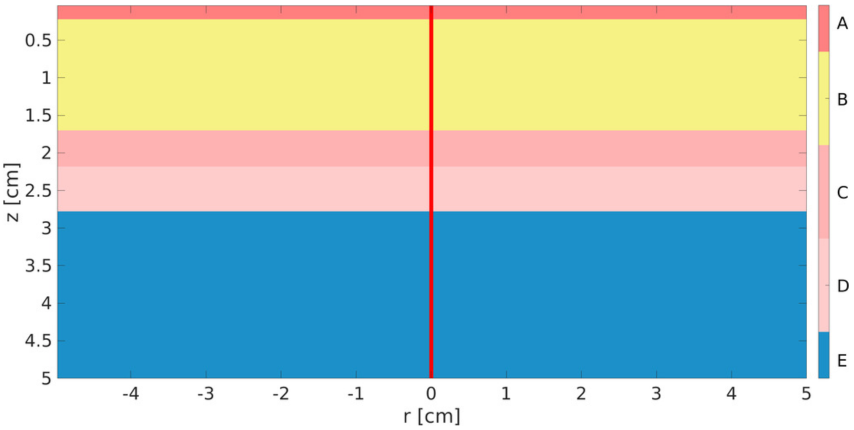

Figure 5.1: Geometry of the layered tissue model used in our Monte Carlo simulations. Layer A is skin, Layer B is adipose, Layer C is muscle, Layer D is uterus, and Layer E is amniotic fluid.

The experimental side of this research requires the stage of fetal visual development to be sufficiently advanced enough to detect stimuli. Therefore, presentation of the laser diodes occurs during the third trimester of pregnancy and this needs to be accounted for in the tissue layer geometry. We have taken layer thickness values from empirical studies, and these are also shown in Table 5.1.

5.3 Results

Initial MC simulations model a single beam's propagation through the tissue model. Figure 5.2 shows cross-sections in the r-z plane of the relative fluence rate (i.e., relative intensity, or watts of power incident per cm^2 per watt delivered) on a base-10 logarithmic scale for a single beam incident at the surface of the maternal abdominal skin, with each image displaying a different adipose thickness. The relationship evident from these images is that increased levels of adipose tissue thickness correspond to reduced levels of light intensity reaching the amniotic fluid. Note that the geometry is presented in cylindrical coordinates for these figures and axial symmetry is assumed.

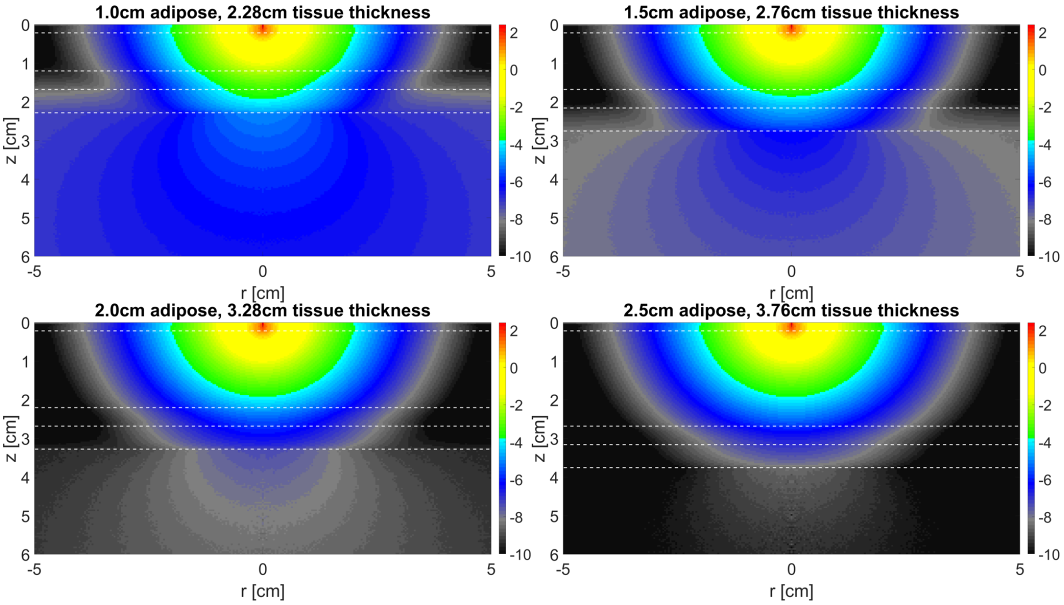

Figure 5.2: Cross-sections of relative fluence rate (i.e., relative intensity, or watts of power incident per cm^2 per watt delivered) in the r-z plane for a single beam incident at the surface of the maternal abdominal skin, for varying adipose thicknesses. Dashed white lines represent layer boundaries as outlined in Table 5.1. Note values are presented in base-10 logarithmic scale and the geometry is presented in cylindrical coordinates.

Since a key objective of our work is to determine the appearance of transdermal monochromatic point source stimuli delivered to the fetus in utero, we present in Figure 5.3 the cross-sections of the simulated single beams' relative fluence rates in the x-y plane for varying adipose thicknesses (note the change to Cartesian coordinates for subsequent images, with no transformation conducted as the model tracks data on both cylindrical and Cartesian grids). Due to the variety of fetal eye positions in utero, it is unclear what position (relative to the tissue-amniotic fluid interface) is the ideal point to consider the simulated light intensity. We present a single option for consideration here: each image shows the beam's simulated relative fluence rate at the tissue-fluid interface for tissues with differing adipose thicknesses (in line with the source stimuli). This decision is due to the low absorption coefficient [Scheel et al., 2018] and relatively low scattering coefficient [Gunther et al., 2021] in amniotic fluid for the wavelength considered. Hence, we propose that light which reaches this interface is likely to continue propagating to the fetus with minimal attenuation – especially when noting that the typical separation between the fetal eye and the uterus is on the order of 1-2 cm [Donovan et al., 2020].

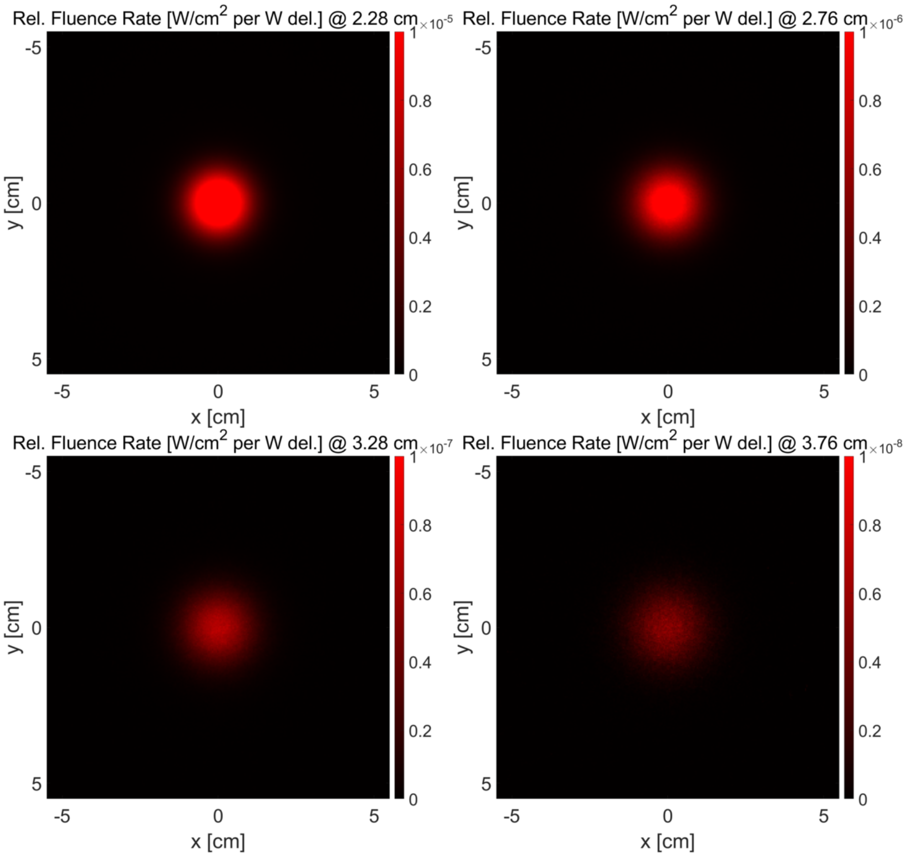

Figure 5.3: Relative fluence rates [W/cm^2 per W delivered] for a single delivered beam. Images show relative intensity at the interface between tissue and amniotic fluid for varying thicknesses of adipose. Note the change in scale between figures.

As expected, the maximum relative intensity declines as adipose tissue thickness is increased. Adipose tissue typically has relatively high levels of absorption and scattering (see Table 5.1) in comparison to other component layers represented in the model, such as skin and amniotic fluid, which leads to the large decline in relative intensity seen with increased adipose thickness. In contrast, amniotic fluid exhibits relatively low levels of absorption and scattering, leading to more noticeable diffusion of the photons that enter the uterine environment. The beam intensity is typically lower in the amniotic fluid than at the interface, with a broader geometric spread being evident. This is indicated by the widening of the intensity patterns shown in the amniotic fluid layers of Figure 5.2 (in particular, for the lesser adipose tissue thicknesses where more light is reaching the fluid), in contrast to the relatively narrow spreads within the tissue.

Figure 5.4 shows the intensity of the beam at the interface between tissue and amniotic fluid, relative to its maximum simulated intensity in the x-direction for $y = 0$ (i.e., the intensity simulated directly below the source delivery at this depth is normalized to 1.0). This plot gives an indication of the horizontal diffusion for a given transdermal monochromatic point stimuli after propagating through maternal tissue. Such information is useful for experimental applications where determining appropriate horizontal separation differences for transdermal stimuli on the maternal abdomen is required to ensure delivered stimuli remain visually distinct in the uterus. Note that larger adipose thicknesses result in visually similar beam profiles to that shown in Figure 5.4, so we simply present the first adipose thickness for consideration.

Figure 5.5 shows the decline in relative fluence rate along the z-axis for the four simulated adipose layer thicknesses. Due to the source location, the maximum values for intensity occur at the surface of the tissue ($z = 0$ cm). The fluence rates decrease with increasing z, as the beam propagates through more of the simulated tissue. Similar to previous studies [Gunther et al., 2021], our model shows exponential trends (linear when on a logarithmic scale) for

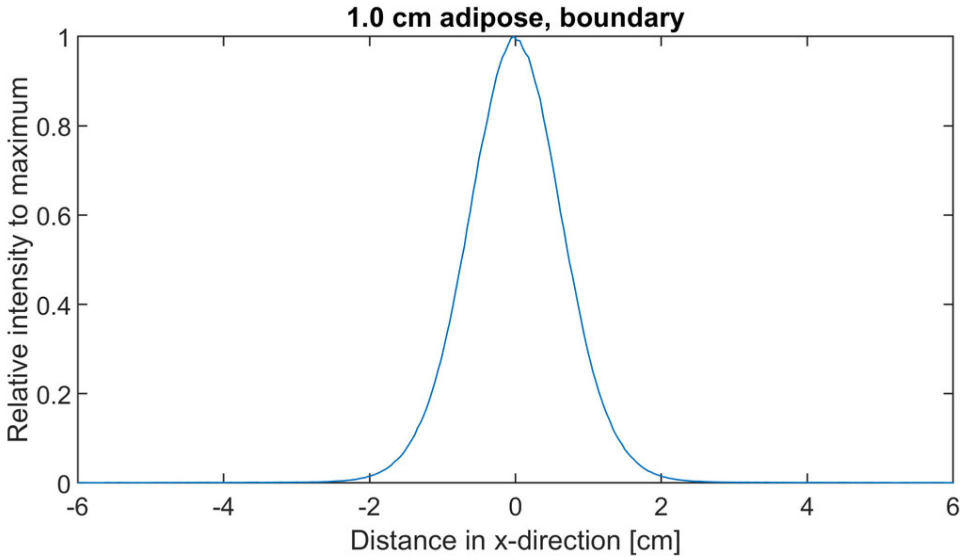

Figure 5.4: Relative intensity of the single beam to its maximum intensity along the x-direction at $y = 0$ for the tissue profile with 1.0 cm adipose thickness at the interface between tissue and amniotic fluid. This gives an indication of the horizontal diffusion for a given transdermal monochromatic point stimuli after propagating through maternal tissue. Only the profile with 1.0 cm adipose thickness is shown. Similar plots generated for tissue profiles with thicker adipose result in noisier images (due to increased absorption impacting statistics) that reflect similar underlying distributions.

the decline in fluence rate over the tissue and amniotic fluid. As adipose tissue thickness increases, the decline in relative fluence rate by the tissue-fluid boundary becomes increasingly apparent. Based solely on these figures, there appears to be a roughly 15-fold decline in the eventual relative fluence rate measured at the tissue-fluid interface when adipose tissue thickness is increased by 0.5 cm. Also plotted beneath each set of data are the estimated slopes from linear regression for the adipose and amniotic fluid components of the 1.5 cm case. The fitted slopes are -2.8556 and -0.3789, which offers a rudimentary manner through which to estimate the attenuation of beams for tissues that fall beyond these simulated scenarios.

In situ experimental designs motivating this modelling work will later involve moving two separate transdermal monochromatic light stimuli towards

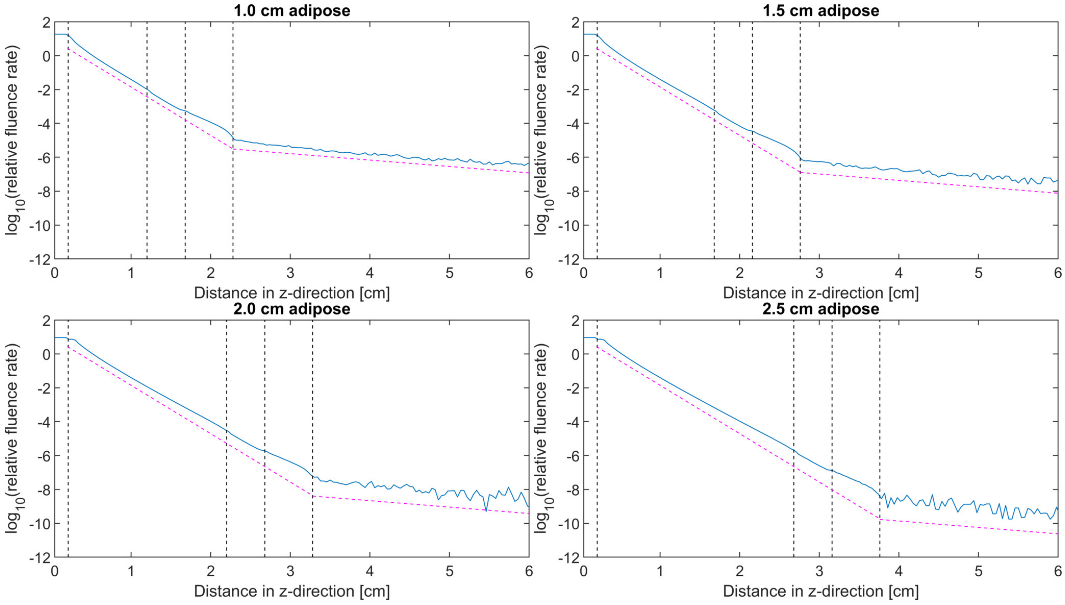

Figure 5.5: Relative fluence rate vs. z-depth for different adipose tissue thicknesses. Note the relative fluence rates are presented in logarithmic scale. Vertical dashed lines represent boundaries between tissue layers, as defined in Table 5.1. Also plotted beneath each set of data are the estimated slopes from linear regression for the adipose and amniotic fluid components of the 1.5 cm case. The fitted slopes are -2.8556 and -0.3789.

one another, without merging from the perspective of the fetus. We are interested, then, in knowing at what point two such stimuli cease to become notably distinct from each other. Consequently, we also model the appearance of two transdermal monochromatic stimuli presented to the fetus in utero, and the cross-sections of simulated x-y plane data for these are shown in Figures 5.6 and 5.7. Each row of images shows the relative fluence rates of two stimuli, as measured at the tissue-fluid interface. We present three separation distances of the light sources for comparison: 18 mm, 25 mm, and 35 mm. These are based on proposed measurements employed for in situ psychological experiments [Reid and Dunn, 2021]. In terms of intensity profiles, it is apparent that an 18 mm separation distance does not lead to noticeably distinct stimuli presentation for any tissue thickness simulated; however, there is reasonable distinction evident for simulations using the 25 mm separation distance, and the 35 mm separation distance appears to lead to noticeable intensity distinction for all simulated tissue thicknesses.

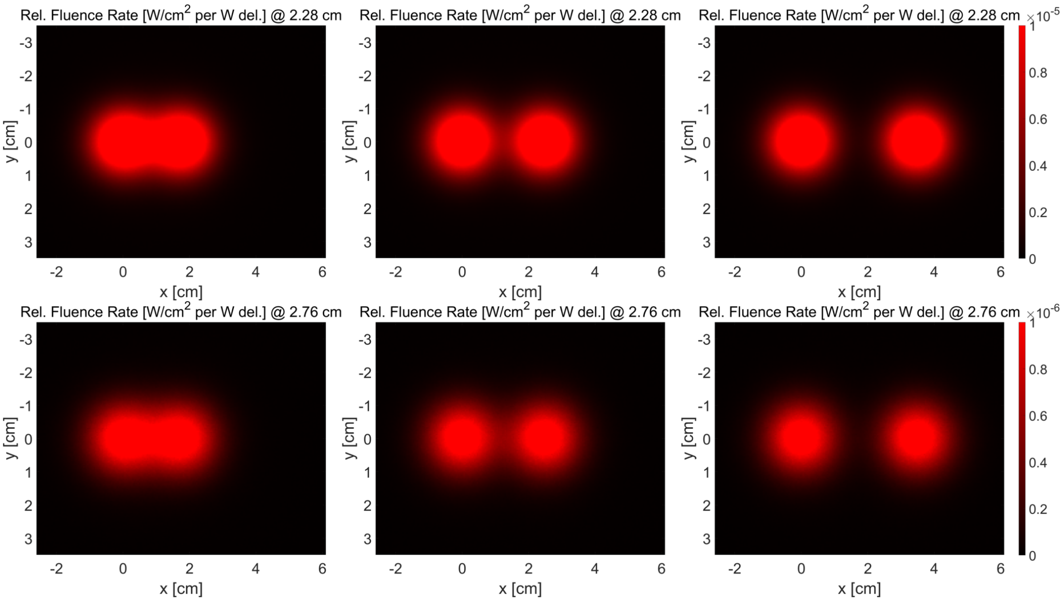

Figure 5.6: Relative fluence rates [W/cm^2 per W delivered] for two stimuli. Left images show 18 mm stimuli separation, centre images 25 mm, and right images 35 mm. The top row is the relative fluence rate at the interface between tissue and amniotic fluid for 1.0 cm adipose, and the bottom row 1.5 cm adipose.

Similar to Figure 5.4, the graphs presented in Figure 5.8 show the profiles of simulated intensity relative to maximum intensity for two beams. As in Figures 5.6 and 5.7, these are measured along the centre of the x-y plane at the tissue-fluid interface. Again, simulated separation distances of 18 mm, 25 mm, and 35 mm are applied at the sources.

As expected, moving the sources closer together causes the intensity distinction between the two beams to be reduced. As adipose tissue thickness is increased, the distinction between the beams at the tissue-fluid interface is steadily reduced, with the 18 mm source separation only showing minimal distinction in the peaks for the 1.0 cm adipose tissue (shown in Figure 5.8), while the 25 mm separation appears to maintain distinct intensity plots when measured at the interface until the adipose tissue is increased to 2.5 cm. The

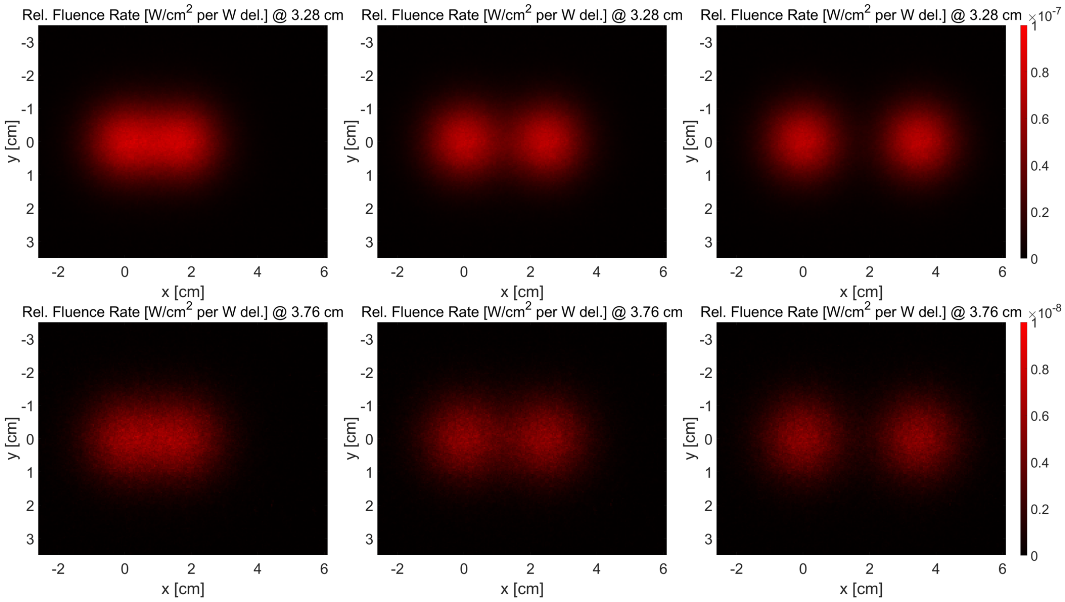

Figure 5.7: Relative fluence rates [W/cm^2 per W delivered] for two stimuli. Left images show 18 mm stimuli separation, centre images 25 mm, and right images 35 mm. The top row is the relative fluence rate at the interface between tissue and amniotic fluid for 2.0 cm adipose, and the bottom row 2.5 cm adipose.

35 mm separation consistently produces distinguishable images at the tissue-fluid interface across all thicknesses, demonstrated in Figures 5.7 and 5.8, with the relative intensity to maximum dropping below 0.2 between the simulated stimuli at the tissue-fluid interface. Note again that larger adipose thicknesses result in qualitatively similar beam profiles to those shown in Figure 5.8, so we simply present the first adipose thickness for consideration.

5.4 Discussion

We use MC simulations to demonstrate the relationship between increasing thicknesses of adipose tissue and the attenuation of transdermal monochromatic point source laser diode stimuli presented to the human fetus in utero. In general, the levels of light intensity reaching the fetus decrease with increasing adipose thickness. For example, comparing the results for the 1.0 cm

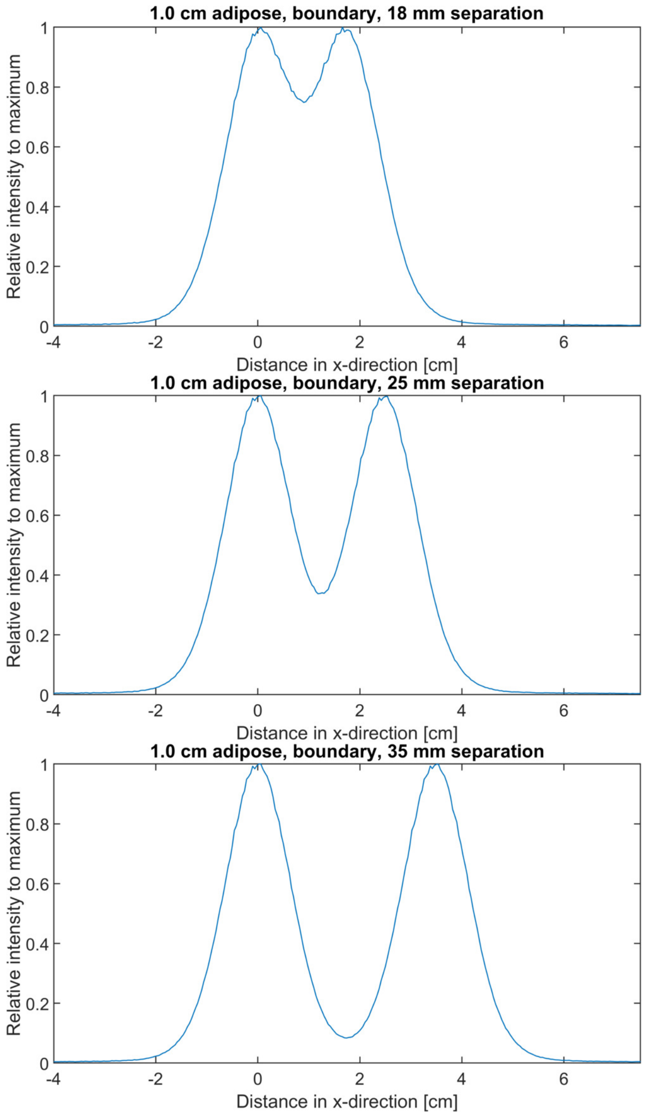

Figure 5.8: Relative intensity of the two beams to their maximum intensity along the x-direction at $y = 0$ for the tissue profile with 1.0 cm adipose thickness at the interface between tissue and amniotic fluid. The top image shows an 18 mm stimuli separation, the centre image a 25 mm separation, and the bottom image a 35 mm separation. Only the profile with 1.0 cm adipose thickness is shown. Similar plots generated for tissue profiles with thicker adipose result in noisier images (due to increased absorption impacting statistics) that reflect similar underlying distributions.

adipose thickness to those of the 2.5 cm adipose thickness in Figure 5.5 shows the former experiences relative fluence rates at the tissue-fluid interface approximately $3,500$ times larger than the latter. This is further demonstrated by the apparent decline in intensity exhibited by the beam profiles at the tissue-fluid interface in Figure 5.3 – the scale from the 1.0 cm adipose thickness to the 2.5 cm adipose thickness falls dramatically, and this is representative of the significant attenuation of simulated photon packets due to increased adipose influence on propagation.

It is important to note that most of the images provided thus far display measurements of relative light intensity. In other words, the incident power (in watts) per unit area (in cm^2) per unit power presented (in watts). For example, the log value shown in Figure 5.5 at the tissue-fluid interface along the z-axis is approximately -7.22 for the 2.0 cm adipose thickness, indicating a simulated relative fluence rate of 6.03×10^{-8} W/cm^2 per W delivered. Using the 5 mW power presented to the tissue, we find a simulated fluence rate of 3.01×10^{-10} W/cm^2 for this incident power. As noted, this is a measure of intensity; however, it does not give an intuitive indication of how "bright" these stimuli may appear to the fetus. To interpret the stimuli from this alternative perspective, we need to convert the simulated intensity to illuminance. This can be handled in a relatively simple manner to ascertain an approximate value that can be interpreted by way of comparison to more common sources of illuminance.

The conversion of intensity (irradiance) in units of watts/m^2 to illuminance in units of lux can be performed using the following formula [Johnsen, 2012]:

$$\text{lux} = 683.002 \cdot \int_0^\infty E(\lambda)\, \bar{y}(\lambda)\, \Delta\lambda, \tag{5.8}$$

where 683.002 is the constant representing the maximum spectral luminous efficacy and is measured in lm/W; $E(\lambda)$ is the intensity (irradiance) spectrum measured in W/m^2 per nm, which is taken from the simulation results; $\bar{y}(\lambda)$ represents either the photopic (light-adapted) or scotopic (dark-adapted) luminosity function of wavelength for humans; and the integral is taken over the spectrum of simulated wavelengths. For our single wavelength simulations, we integrate over a Dirac delta function. Hence, the conversion equation becomes simply

$$\mathrm{lux} = 683.002 \cdot E\left(\lambda\right)\bar{y}\left(\lambda\right). \tag{5.9}$$

The distinction between using the photopic or scotopic luminosity function involves the levels of light under consideration — for everyday light levels, the response of the human eye is most appropriately approximated by the photopic luminosity function, while the scotopic luminosity function is most applicable in low light conditions. Consequently, one might initially expect the uterine environment to correspond to one where the scotopic function is most relevant; however, it is unclear exactly what levels of light might already be present in the uterus due to natural light sources. Similarly, the development of the fetal eye (and its adaptation to the uterine environment) is presently not well known. Assuming low light levels would likely offer the safest and most reasonable starting estimate, and this indicates use of the scotopic function may be appropriate for our purposes.

Taking, for example, our previously mentioned value of 3.01×10^{-10} W/cm^2 at the tissue-fluid interface for 2.0 cm adipose thickness, converting this to W/m^2 to find $E\left(650\mathrm{nm}\right)$, and substituting this value into the equation with $\bar{y}\left(650\mathrm{nm}\right) = 0.107$ for the photopic function at 650nm or 0.000677 for the scotopic function at 650nm [Williamson et al., 1983], we calculate illuminances of 2.2×10^{-4} lx or 1.4×10^{-6} lx, respectively. The former is roughly between the illuminance levels of an overcast night sky and a clear, starry night sky [Rich and Longcore, 2006], while the latter is not immediately comparable to any common illuminance level. This suggests that illuminance levels provided to the uterine wall by the simulated stimuli are unlikely to offer a noticeable illuminance for the fetus when adipose tissue thickness is 2.0 cm or above.

In contrast, however, taking the simulated tissue-fluid interface relative fluence rate from Figure 5.5 for the 1.0 cm adipose thickness and applying the same calculation gives a result of approximately 0.05 lx for the photopic function, which is an illuminance approximately between a full moon in clear conditions or a quarter moon [Rich and Longcore, 2006]. Using the scotopic function as above results in a calculated illuminance of 3.27×10^{-4} lx, which is between the levels of illuminance exhibited by an overcast night sky and a clear, starry night sky [Rich and Longcore, 2006]. These values, and those as calculated for the simulations involving all other tissue thicknesses, are summarized in Table 5.2 alongside their counterpart values taken from simulating light propagation into the amniotic fluid. In general, the conclusion drawn from these simulations is that the uterine wall is reasonably illuminated under these conditions for adipose tissue thicknesses of 1.0 cm to 1.5 cm, but adipose thicknesses of 2.0 cm and above seem unlikely to offer noticeable uterine wall illumination. Similarly, due to the nature of amniotic fluid, levels of illuminance from the given transdermal stimuli with 1.0 cm or 1.5 cm adipose tissue thickness would seem likely to remain reasonably high upon reaching the fetus.

Table 5.2: Illuminances determined by simulations at the tissue-fluid interface for various adipose tissue thicknesses.

Adipose thickness [cm]	**Tissue thickness [cm]**	**Log at interface**	**Photopic [lx]**	**Scotopic [lx]**	**Photopic comparison (night sky)**
1.00	2.28	-4.85	5.16×10^{-2}	3.27×10^{-4}	$\frac{1}{4}$ moon — Full moon, clear
1.50	2.76	-6.03	3.41×10^{-3}	2.16×10^{-5}	Clear, starry — $\frac{1}{4}$ moon
2.00	3.28	-7.22	2.20×10^{-4}	1.39×10^{-6}	Overcast — Clear, starry
2.50	3.76	-8.41	1.42×10^{-5}	8.99×10^{-8}	Overcast

Note that the prior discussion does not counter the limited scope for fetal ability to individuate transdermal stimuli with smaller separation distances.

Though the illuminance offered by a single laser diode point light source may be evident to the fetus, the likelihood of the fetus being able to discern separate equivalent transdermal monochromatic light sources when presented in close proximity to one another – less than 25mm, for instance – is heavily impacted by attenuation in the maternal tissue (particularly from adipose tissue). Similarly, additional diffusion in the amniotic fluid would further complicate this aspect. Consequently, it is possible that fetuses developing in uterine environments with moderately thick adipose tissue layers are able to see such transdermal stimuli presented, yet they are unable to recognize the stimuli as distinct sources of light if their delivery separation distance is not sufficiently large on the maternal abdomen.

Despite the reasonable likelihood of transdermal monochromatic laser diode stimuli reaching the fetus and illuminating the womb, the argument of whether the fetal eye and brain are developed enough to recognize or respond to the stimuli is one which needs to be considered when applying these results. In general, experimental work in the field of fetal vision focuses on third trimester fetuses. It has been shown that the fetal eye develops late in pregnancy [Donovan et al., 2020], and the fetus is capable of responding to transdermal laser diode stimuli after 34 weeks of pregnancy [Dunn et al., 2015]. Hence, although it is not the focus of this paper, any interpretation of these results from the perspective of fetal recognition should consider only the third trimester of gestation — the applicability to fetal recognition in earlier stages of development is not yet well known.

An important conclusion that can be drawn from these simulations pertains directly to the experimental component of this wider research and the field of fetal visual development in general. Our group is interested in the visual capabilities of the human fetus, and this is most readily examinable through delivering laser diode stimuli to the uterus and recording fetal response via ultrasound or heart rate. Based on the results of our model, experiments of this nature clearly face constraints in the delivery of stimuli to the fetus, including low levels of illuminance delivered for some adipose tissue thicknesses and the poor uterine distinction of multiple stimuli presented to individuals with higher adipose thickness. Consequently, this knowledge can inform future experimental design in at least three ways.

First, the 5 mW incident power used in these experiments appears to be on the low end of what is capable of delivering stimuli to the average fetus. A stronger laser diode (within the range of safe power levels) would result in brighter stimuli presentation to the fetus; however, taking this approach too far may evidently pose potential danger to both the fetal eye and the mother's skin due to heat output from the light source.

Second, the poor propagation of simulated light through thicker adipose layers suggests an effective screening mechanism when identifying candidates for experimental participation. Such an approach could involve measuring abdominal tissue composition via ultrasound to exclude those with high adipose thicknesses. Alternatively, the measuring of a “no response” outcome during stimuli experiments might suggest that the mother was an inappropriate candidate for the utilized light source. This may be further verified by examining data taken from the ultrasound readings and categorising “no response” participants based on tissue composition.

Third, experimental applications involving multiple transdermal monochromatic light sources need to carefully consider placement along the maternal abdomen — stimuli with separation distances less than 25 mm evidently will face a large degree of “blurring” across the delivered stimuli, dependent on the exact fetal eye location (and its covering), and this can pose significant problems for experimental design and the conclusions drawn.

Future work should consider the influence of varying the muscle and uterus layers simulated. These layers also exhibit high absorbing and scattering properties, respectively, and though their significance in the overall tissue composition is not as prominent as that of adipose, their thicknesses do vary across individuals. Similarly, the thickness of these layers has a temporal aspect (like adipose tissue), with the stage of gestation also noticeably affecting their prominence. There is also an argument to be made for accounting for skin color in the model, as melanin is highly absorbing in this part of the spectrum. Consideration of these aspects with alterations made in a similar manner to those shown in this work would further illuminate their significance in determining the levels of light reaching the fetus.

Further, this work has assumed the fetal eye is open when determining transdermal stimuli appearances in utero (i.e., attenuation has not been simulated through an eyelid). Of course, the presence of an additional layer of skin would introduce further attenuation of the light source simulated. Due to the nature of the fetal sleep cycle and practical constraints, it is difficult to align experimental participants with times where the fetal eye is definitely open and exposed. Hence, the exact applicability of this present study to experimental situations where the fetal eye is closed needs to be considered carefully. Future work should introduce an additional layer to represent the eyelid in order to offer information on these situations. The presence of clothing (and similar additional layers) could also be considered in future simulations akin to this work; however, in situ studies exploring the development of fetal vision typically require direct skin contact for stimuli delivery, so similar applicability to the wider research field would be limited in comparison to that of this work.

Lastly, we have here simulated point sources in instances where the abdominal tissue is assumed to be locally flat (planar). In reality, the maternal abdomen exhibits curvature and this change in geometry would presumably have some impact on the results for situations where stimuli were not presented in such close proximity to one another. Future modelling work intends to account for this aspect alongside the points noted above.

5.5 Conclusion

The modelling presented in this paper offers quantitative data via MC simulations which further indicate that the human uterine environment can be at least partially illuminated via appropriate laser diode stimuli presented to the maternal abdomen. We have developed our own model of photon propagation through maternal abdominal tissue in line with common algorithms within the field and incorporated computational approaches that allow for efficient simulation of large numbers of photon packets (beyond 12 billion per run). The intensity of light and consequent illuminance delivered to the fetus is found to vary strongly with maternal abdominal adipose thickness, and our simulations show that point transdermal monochromatic stimuli delivery to the fetus can result in illuminance comparable to that of a full moon for lower adipose thicknesses.

Increased adipose thickness causes light to be heavily attenuated, and this strongly degrades the delivered stimuli; however, the simulations suggest consideration of stronger incident stimuli (within the realms of fetal and maternal safety) would improve uterine illuminance. Further, the work of this paper suggests an appropriate screening tool for participants in fetal visual stimuli experiments could involve measuring abdominal adipose thickness of the mother; if stimuli are unable to be adjusted to improve photon penetration, the results of this modelling support excluding results from these participants due to low levels of delivered uterine illuminance.

Lastly, we have explored the potential to deliver multiple distinct transdermal monochromatic stimuli to the fetus in line with our research group's experimental design. The results of our simulations suggest that a separation distance of at least 25 mm is likely to lead to distinct visual stimuli for the fetus under the current stimuli design. Again, usage of a more powerful laser diode light source would ensure the presented images are visible for fetal eyes resting further into the amniotic fluid; however, any increase in power would need to be handled with caution and strong regard for safety requirements due to potential danger imposed to both the fetal eye and maternal skin.

This work has focused on varying adipose thickness; however, future studies will also investigate the required stimuli separation distances (and attenuation of stimuli) under varying muscle and uterus thicknesses. In addition, there is scope to explore the extension of point light sources to a range of alternate stimuli.

References

A. N. Bashkatov, E. A. Genina, V. I. Kochubey, and V. V. Tuchin. Optical properties of the subcutaneous adipose tissue in the spectral range 400–2500 nm. *Optics and Spectroscopy*, 99:836–842, 2005.

R. M. Bradley and C. M. Mistretta. Fetal sensory receptors. *Physiological Reviews*, 55(3):352–382, 1975.

F. D'Ambrosi, F. Crovetto, E. Colosi, I. Fabietti, F. Carbone, B. Tassis, S. Motta, A. Bulfoni, L. Fedele, G. Rossi, and N. Persico. Maternal Subcutaneous and Visceral Adipose Ultrasound Thickness in Women with Gestational Diabetes Mellitus at 24-28 Weeks' Gestation. *Fetal Diagnosis and Therapy*, 43(2):143–147, 06 2017.

H. Dehghani, M. E. Eames, P. K. Yalavarthy, S. C. Davis, S. Srinivasan, C. M. Carpenter, B. W. Pogue, and K. D. Paulsen. Near infrared optical tomography using nirfast: Algorithm for numerical model and image reconstruction. *Communications in Numerical Methods in Engineering*, 25(6): 711–732, 2009.

M. Del Giudice. Alone in the Dark? Modeling the Conditions for Visual Experience in Human Fetuses. *Developmental Psychobiology*, 53:214–219, 2011.

T. Donovan, K. Dunn, A. Penman, R. J. Young, and V. M. Reid. Fetal eye movements in response to a visual stimulus. *Brain and Behavior*, 10(8): e01676, 2020.

J. J. Duderstadt and L. J. Hamilton. *Nuclear Reactor Analysis.* Wiley, 1976.

K. Dunn, N. Reissland, and V. M. Reid. The functional foetal brain: A systematic preview of methodological factors in reporting foetal visual and auditory capacity. *Developmental Cognitive Neuroscience*, 13:43–52, 2015.

W. L. Dunn and J. K. Shultis. 5 - variance reduction techniques. In W. L. Dunn and J. K. Shultis, editors, *Exploring Monte Carlo Methods*, pages 97–132. Elsevier, Amsterdam, 2012.

C. P. Durnwald and B. M. Mercer. Myometrial thickness according to uterine site, gestational age and prior cesarean delivery. *The Journal of Maternal-Fetal & Neonatal Medicine*, 21(4):247–250, 2008.

M. Fukano, Y. Tsukahara, S. Takei, S. Nose-Ogura, T. Fujii, and S. Torii. Recovery of abdominal muscle thickness and contractile function in women after childbirth. *International Journal of Environmental Research and Public Health*, 18(4):1–9, February 2021.

J. Gunther, B. Jayet, A. Jacobs, R. Burke, J. Kainerstorfer, and S. Andersson-Engels. Effect of the presence of amniotic fluid for optical transabdominal fetal monitoring using Monte Carlo simulations. *Journal of Biophotonics*, 14, 06 2021.

E. Hecht. *Optics, 4th Edition.* Pearson plc, 2001.

L. G. Henyey and J. L. Greenstein. Diffuse radiation in the Galaxy. *The Astrophysical Journal*, 93:70–83, January 1941.

M. S. Hwang. Abdominal skin subcutaneous fat thickness over the gestational period in korean pregnant women: a descriptive observational study. *Korean Journal of Women Health Nursing*, 27(4):318–325, 2021.

S. Jacques, D. Weaver, and S. Reppert. Penetration of Light Into the Uterus of Pregnant Mammals. *Photochemistry and Photobiology*, 45:637 – 641, 01 1987.

S. Jacques, N. Ramanujam, G. Vishnoi, R. Choe, and B. Chance. Modeling photon transport in transabdominal fetal oximetry. *Journal of Biomedical Optics*, 5:277–82, 08 2000.

S. L. Jacques. Monte Carlo Modeling of Light Transport in Tissue (Steady State and Time of Flight). In A. J. Welch and M. J. C. van Gemert, editors, *Optical-Thermal Response of Laser-Irradiated Tissue*, pages 109–144. Springer Netherlands, 2011.

M. Jermyn, H. R. Ghadyani, M. A. Mastanduno, W. D. Turner, S. C. Davis, H. Dehghani, and B. W. Pogue. Fast segmentation and high-quality three-dimensional volume mesh creation from medical images for diffuse optical tomography. *Journal of Biomedical Optics*, 18(8), 2013.

S. Johnsen. *The optics of life: A biologist's guide to light in nature*. Princeton University Press, 01 2012.

N. J. Kennedy, M. J. Peek, A. E. Quinton, V. Lanzarone, A. Martin, R. Benzie, and R. Nanan. Maternal abdominal subcutaneous fat thickness as a predictor for adverse pregnancy outcome: a longitudinal cohort study. *BJOG: An International Journal of Obstetrics & Gynaecology*, 123(2):225–232, 2016.

J. Lecanuet and B. Schaal. Fetal sensory competencies. *European Journal of Obstetrics & Gynecology and Reproductive Biology*, 68(1):1–23, 1996.

A. W. Liley. The foetus as a personality. *Australian & New Zealand Journal of Psychiatry*, 6(2):99–105, 1972.

R. Marchesini, A. Bertoni, S. A. Andreola, E. Melloni, and A. E. Sichirollo. Extinction and absorption coefficients and scattering phase functions of human tissues in vitro. *Applied optics*, 28(12):2318–24, 1989.

I. V. Meglinski and S. J. Matcher. Quantitative assessment of skin layers absorption and skin reflectance spectra simulation in the visible and near-infrared spectral regions. *Physiological Measurement*, 23(4):741, oct 2002.

M. Myowa-Yamakoshi and H. Takeshita. Do Human Fetuses Anticipate Self-Oriented Actions? A Study by Four-Dimensional (4D) Ultrasonography. *Infancy*, 10(3):289–301, 2006.

S. Rao, C. Chun, J. Fan, J. M. Kofron, M. B. Yang, R. S. Hegde, N. Ferrara, D. R. Copenhagen, and R. A. Lang. A direct and melanopsin-dependent fetal light response regulates mouse eye development. *Nature*, 494:243–246, 2013.

V. M. Reid and K. Dunn. The fetal origins of human psychological development. *Current Directions in Psychological Science*, 30(2):144–150, 2021.

V. M. Reid, K. Dunn, R. J. Young, J. Amu, T. Donovan, and N. Reissland. The Human Fetus Preferentially Engages with Face-like Visual Stimuli. *Current Biology*, 27:1825–1828, 03 2017.

C. Rich and T. Longcore. *Ecological Consequences of Artificial Night Lighting*. Island Press, 01 2006.

P. M. Ripley, J. G. Laufer, A. D. Gordon, R. J. Connell, and S. G. Bown. Near-infrared optical properties of ex vivo human uterus determined by the Monte Carlo inversion technique. *Physics in Medicine & Biology*, 44(10): 2451–62, oct 1999.

A. M. Scheel, S. J. Ritchie, N. J. L. Brown, and S. L. Jacques. Methodological problems in a study of fetal visual perception. *Current Biology*, 28(10): R594–R596, 2018.

C. R. Simpson, M. Kohl, M. Essenpreis, and M. Cope. Near-infrared optical properties of ex vivo human skin and subcutaneous tissues measured using the Monte Carlo inversion technique. *Physics in Medicine & Biology*, 43(9): 2465–78, sep 1998.

D. G. Smith. *Field Guide to Physical Optics*, pages 30–31. Field Guides. SPIE Press, 2013.

A. Torricelli, A. Pifferi, P. Taroni, E. Giambattistelli, and R. Cubeddu. In vivo optical characterization of human tissues from 610 to 1010 nm by time-resolved reflectance spectroscopy. *Physics in Medicine & Biology*, 46(8): 2227–37, jul 2001.

L. Wang, S. L. Jacques, and L. Zheng. MCML — Monte Carlo modeling of light transport in multi-layered tissues. *Computer Methods and Programs in Biomedicine*, 47(2):131–146, 1995.

L. Wang, S. L. Jacques, and L. Zheng. Conv—convolution for responses to a finite diameter photon beam incident on multi-layered tissues. *Computer Methods and Programs in Biomedicine*, 54(3):141–150, 1997.

A. J. Welch and M. J. C. van Gemert. *Optical-Thermal Response of Laser-Irradiated Tissue*. Springer Netherlands, 2011.

S. Williamson, H. Z. Cummins, and J. N. Kidder. *Light and Color in Nature and Art*. John Wiley & Sons, 1983.

M. B. Yang, S. Rao, D. R. Copenhagen, and R. A. Lang. Length of day during early gestation as a predictor of risk for severe retinopathy of prematurity. *Ophthalmology*, 120(12):2706–2713, 2013.

Chapter 6

Second Paper Motivation

The results of the previous chapter are useful in determining the illuminance of the uterine environment from point sources of transdermal monochromatic light; however, this is a highly specific situation that is essentially limited in application to experimental scenarios — a potentially more common scenario to consider is that of the maternal abdomen exposed to natural light. Consequently, the exploration of how natural light, particularly sunlight, illuminates the human womb represents a continuation of the previous chapter driven by several motivations.

Firstly, understanding the interplay between natural light and the fetal environment is integral to elucidating its potential impacts on fetal development. Light serves as a fundamental environmental cue, regulating circadian rhythms and influencing various physiological processes within the developing fetus [Lunshof et al., 1998; Serón-Ferré et al., 2001]. Thus, delving into the mechanisms by which natural light penetrates the uterine environment offers insights into the intricate relationship between external stimuli and intrauterine development, potentially unraveling novel pathways through which light exposure may shape fetal health outcomes.

Moreover, investigating the dynamics of natural light within the womb holds implications for obstetric care, maternal well-being, and future work on artificial wombs. Evidently, an understanding of the variations at play for uterine illumination across a range of lighting, environmental, temporal, and gestational conditions can be used to improve prenatal care with the goal of improving fetal visual outcomes. In a similar manner, this understanding can be used in work on artificial wombs — such as the BioBag product, for example [Partridge et al., 2017] — with the goal of accurately mimicking the optical properties of maternal tissue and its interplay with natural light.

To understand the interactions between natural light and maternal tissue, we extend our Monte Carlo model in the following chapter. The simulated stimulus was first expanded from a point source to a broader illumination of the maternal abdomen. Monochromatic sources were simulated from across the visible spectrum and combined, resulting in a simulated natural light source that was scaled to the strength of direct sunlight at sea level. From this, we estimated the upper bound for uterine illumination in the case of no skin coverings. This modelling was then further extended to account for a layer of typical shirt fabric.

References

S. Lunshof, K. Boer, H. Wolf, G. van Hoffen, N. Bayram, and M. Mirmiran. Fetal and maternal diurnal rhythms during the third trimester of normal pregnancy: Outcomes of computerized analysis of continuous twenty-four—hour fetal heart rate recordings. *American Journal of Obstetrics and Gynecology*, 178(2):247–254, 1998.

E. Partridge, M. Davey, M. Hornick, P. McGovern, A. Mejaddam, J. Vrecenak, C. Burgos, A. Olive, R. Caskey, T. Weiland, J. Han, A. Schupper, J. Connelly, K. Dysart, J. Rychik, H. Hedrick, W. Peranteau, and A. Flake. An extra-uterine system to physiologically support the extreme premature lamb. *Nature Communications*, 8:15112, 05 2017.

M. Serón-Ferré, C. Torres-Farfán, M. Forcelledo, and G. Valenzuela. The development of circadian rhythms in the fetus and neonate. *Seminars in*

Perinatology, 25(6):363–370, 2001. Hormonal Therapy of the Fetus and Neonate.

Chapter 7

Modeling the propagation of natural light to the human womb using Monte Carlo simulations

7.1 Introduction

Investigations into the sensory development of the human fetus have traditionally focused on the auditory and olfactory systems [Bradley and Mistretta, 1975; Lecanuet and Schaal, 1996]. This is due to a prevailing assumption that sensory stimulation from visual sources is either absent from the womb or negligible [Myowa-Yamakoshi and Takeshita, 2006] unless there is direct exposure of the maternal abdomen to a powerful light source [Liley, 1972].

Recent studies, however, have suggested that the human womb may provide an environment that is sufficiently illuminated by attenuated exterior lighting to allow for visual experience by the fetus [Del Giudice, 2011]. Prior work into the delivery of visual stimuli to the uterus of pregnant rats and guinea pigs has shown significant transmission of light in the visible spectrum [Jacques et al., 1987]. Experimental research into human fetal visual development has demonstrated that delivering transdermal visual stimuli to the human fetus is feasible and that fetuses will behaviourally respond to such stimuli [Reid et al., 2017].

Even though later computational simulations suggest significant attenuation may have removed details of the presented stimuli prior to arrival at the fetal eye [Scheel et al., 2018], the experimental results nonetheless demonstrate the feasibility of delivering visual stimuli to the human fetus via the application of transdermal laser diodes [Reid et al., 2018].

Further research into human visual development has explicitly incorporated computational modelling to determine the attenuation of transdermal monochromatic stimuli presented to the fetus [Isaac et al., accepted, 2024]. This prior work was undertaken to inform experimental applications and provide estimates of the uterine illumination delivered by a 5 mW laser diode at the 650 nm wavelength. Isaac et al. [accepted, 2024] show that adipose tissue clearly has significant implications for illumination, with estimates ranging from uterine illumination akin to an overcast night sky with adipose thickness of 2.0 cm to that of a full moon in clear conditions with adipose thickness of 1.0 cm. This quantification of uterine illumination nonetheless raises several further questions relating to the uterine visual environment.

Foremost, to our knowledge, the day-to-day illumination of the uterus by natural light has not yet been explored. This is despite evidence from animal research that uterine light plays a prominent role in the development of the fetal mouse eye [Rao et al., 2013], and further work finding a link between average day length during early gestation and visual outcomes for human infants [Yang et al., 2013]. The sole previous effort aimed at estimating the illuminance of the human uterus by natural light incorporated linear regression to determine the light transmission through biological tissue samples in estimating an equation to understand the effect of maternal tissue and skin coverings [Del Giudice, 2011]. Though this work suggested that the uterine cavity was not a dark environment as previously assumed, the approach was limited to those conditions provided by deceased avian tissue samples – hence, not appropriately representing the attenuating properties of living human tissue – and also lacked the required model flexibility to allow for alterations to, for example, tissue composition.

There are two primary reasons behind why a more sophisticated approach to modelling uterine illumination by natural light is beneficial to the wider field of human development. First, there are clear implications for the field of fetal visual development that stem from understanding the uterine illumination provided by natural light. Across gestation, the thickness of the maternal wall varies with the growth of the fetus. Due to the increasing levels of light attenuation offered by thicker tissue [Isaac et al., accepted, 2024], this implies a temporal variation in the levels of uterine illuminance provided to the fetus across gestation. Nearer to birth, maternal tissue is diminished across the abdomen when contrasted with earlier in gestation, due to tissue displacement associated with an enlarged uterus and a larger fetus. Similarly, there is scope to explore the impact to these illumination levels from additional clothing layers, lower exposure to light from geographical restrictions, and seasonal variations in light. Modelling the effect of natural light on the illumination of the uterus provides a quantified understanding of the degree to which these aspects may begin to impact the development of the fetal eye, as well as allowing us to explore the extent of its impact on other development (such as that of the fetal brain).

Second, though work has been conducted in exploring the eventual image delivered to the human fetus by transdermal monochromatic stimuli [Scheel et al., 2018; Isaac et al., accepted, 2024], one clear limitation to the conclusions was the assumption of a dark uterine wall. The simulations implicitly assume the uterus is only illuminated by the transdermal stimuli presented; however, in practice, experimental efforts applicable to these simulations are not undertaken in a completely dark environment – there is some non-zero level of background environmental lighting incident to the maternal abdomen. The presence of this lighting may offer some unmodelled baseline uterine illumination which would call into question the precise appearance of the stimuli to the fetus. If the image provided less of a contrast against the uterine wall due to background lighting, the fetus may not see the stimuli. Hence, understanding the effect of natural light on the uterine environment allows for a more precise understanding of the visual effect provided by transdermal monochromatic stimuli in experimental applications.

In this paper, we therefore explore the extent to which the human uterine environment is illuminated by natural light. We use a direct particle simulation approach through a computational model developed in C17 standard C to simulate light transport through dynamically dispersive tissue. This model was initially developed to model light reaching the human fetus from transdermal monochromatic point source stimuli applied to the maternal abdomen [Isaac et al., accepted, 2024]. As in our initial implementation, the model simulates five layers: four represent different maternal abdominal tissue structures and one represents the amniotic fluid where the fetus resides. To reduce noise and produce appropriate statistical accuracy, each simulation run completed for this paper has employed billions of photon packets.

We begin by separately simulating and demonstrating the attenuation of transdermal monochromatic point light source stimuli at 50 nm intervals across the visible light spectrum. This shows the extent to which differing wavelengths of light interface with maternal tissue. Next, we combine these simulations in line with the distribution of the visible component of sunlight. This produces a simulated natural light point source for inspection. In practice, this is a purely hypothetical instance with the consequence that the model is extended to demonstrate the effect on the uterine cavity when illuminating the tissue with simulated natural light from an expanded source region. This is interpreted in the context of several typical lighting scenarios, and the influence of a clothing layer on the consequential illumination is also examined.

Overall, in this paper, we aim to explore the following questions: (a) How can the interaction of natural light with maternal tissue be simulated via the combination of individual monochromatic simulations? (b) To what (if any) extent does natural light under everyday conditions illuminate the uterine cavity, as a function of tissue thickness?

7.2 Methodology

Previously, we have used a purpose-built MC computational model [Isaac et al., accepted, 2024] to simulate the propagation of light from monochromatic point source stimuli through a maternal abdomen model. As we are here interested in the spectrum of visible light, we first simulate light propagation from individual wavelengths distributed across this spectrum. Typically, detection of light by the human eye occurs in the range of 380 to 750 nanometers [Starr, 2005]. Hence, we sought tissue parameters in this range for use within our model; however, data from the literature is sparse with regard to the specific properties exhibited by maternal tissue. As a result, we elected to initially simulate seven individual monochromatic point sources at the following wavelengths: 400 nm, 450 nm, 500 nm, 550 nm, 600 nm, 650 nm, and 700 nm.

As a first attempt to replicate the visual impact of natural light on the womb, we combine the seven chosen wavelengths to generate a "natural light point source". Across the visible spectrum, it can be seen that the irradiance of sunlight at the earth's surface is approximately evenly distributed per wavelength (see, for example, Wang and Yu [2023]). This serves as a starting point for our modelling, and we have hence combined the data with equal weighting on each wavelength to replicate a uniform distribution across the visible spectrum. This gives an initial estimate of the extent to which natural light penetrates the maternal abdomen; however, it explicitly assumes a point source due to the incidence site. We consequently repeated the simulations with the point sources widened to replicate a broad natural light source incident across the simulated tissue. Combining these simulations gives our first estimates of the extent to which natural light penetrates the womb.

As we are interested in understanding the extent to which natural light illuminates the womb and its consequent influence on the developing human visual system, we have attempted to utilise only parameters found from maternal tissue. Particularly, there is evidence to suggest that the fetal visual system is developed enough to recognize and respond to visual stimuli by the third trimester of gestation — the fetal eye develops late in pregnancy [Donovan et al., 2020], and the fetus has been shown to be capable of responding to transdermal laser diode stimuli after 34 weeks of pregnancy [Dunn et al., 2015]. Hence, we aim to restrict our parameters to those relevant to this stage of pregnancy. For certain wavelengths, however, the literature is not yet detailed enough to enable a definitive restriction of our model parameters to any specific temporal stage of pregnancy. Consequently, though we attempt to limit used parameters to those found from third trimester pregnancies, some values are taken from the general population where appropriate data is unavailable. In cases where general population data is unavailable, values have been approximated from those available in the literature. In any case, all parameter sources are identified as necessary and listed in Tables 7.1, 7.2, and 7.3.

All simulations were performed via a purpose-built computational model written in C17 standard C [Isaac et al., accepted, 2024]. This model treats photon propagation modelling as direct particle simulation and follows a similar algorithm to the prominent Monte Carlo for Multi-Layered media (MCML) model [Wang et al., 1995]. Using our own model allowed simpler incorporation of aspects related to improved computational efficiency (MPI, for example) and also enables easier customization for our future research goals.

When considering the simulated medium, we elected to split the model into six layers: the skin, adipose, muscle, and uterus layers represent the maternal tissue, followed by an amniotic fluid layer and a pseudo-fetal layer (see Section 7.2.1) to represent the uterine environment and fetus.

As an extension to the model described above, we also investigate the inclusion of a clothing layer. To examine the impact of clothing, we have introduced an additional layer above the tissue. Optical parameters for the clothing were

Table 7.1: Absorption coefficients [cm^{-1}] used in Monte Carlo simulations for each wavelength (listed as, and measured in, nm) and medium. All values are sourced directly from literature where possible, though it is noted when an approximation has been made.

nm	**Skin**[1]	**Adipose**[2]	**Muscle**[3]	**Uterus**[4]	**Am. Fluid**[5]
400	3.76	3.90	8.00	1.64	0.0002
450	2.50	2.00	5.67	1.26	0.0004
500	1.19	1.30	4.00	0.95	0.0005
550	1.25	1.40	2.65	0.70	0.0008
600	0.69	0.90	1.70	0.50	0.003
650	0.50	0.70	1.00	0.32	0.003
700	0.48	0.60	0.48	0.20	0.006

[1] Estimated through data from Bashkatov et al. [2005]

[2] Estimated through data from Bashkatov et al. [2005] and Shimojo et al. [2020]

[3] Estimated through data from Simpson et al. [1998]

[4] Estimated through data from Ripley et al. [1999]

[5] Calculated from Buiteveld et al. [1994], with temperature set to 37.9°C.

sourced from existing literature where possible, though some required approximation where literature values were unable to be found. Hence, for these simulations, we approximate for the clothing layer that its thickness is 0.12 cm (roughly equivalent to a t-shirt), its scattering coefficient μ_s is 25 cm^{-1}, and its optical anisotropy g is 0.5. We further set its absorption coefficient μ_a to be 38 cm^{-1} [El-Amoudy and El-Ebissy, 2014] and its refractive index n to be 1.5 [Fox, 1939]. These values are assumed equivalent across all simulated wavelengths due to limited values found in the literature from which to base approximations.

When interpreting the simulated outputs, a greater understanding of the visual impact to the uterine environment from natural light can be gained from converting to illumination in lux, which gives a more intuitive indication

Table 7.2: Scattering coefficients [cm^{-1}] used in Monte Carlo simulations for each wavelength (listed as, and measured in, nm) and medium. All values are sourced directly from literature where possible, though it is noted when an approximation has been made.

nm	**Skin**[1]	**Adipose**[2]	**Muscle**[3]	**Uterus**[4]	**Am. Fluid**[5]
400	626.94	178.66	146.43	180.00	1.00
450	460.46	165.00	129.48	171.40	1.00
500	363.80	153.51	115.98	163.00	1.00
550	304.11	144.00	104.98	152.60	1.00
600	265.29	135.61	95.86	141.00	1.00
650	238.89	128.43	88.17	137.00	1.00
700	220.21	122.00	81.60	113.00	1.00

[1] Estimated via equation from Bashkatov et al. [2005]

[2] Estimated through data from Bashkatov et al. [2005]

[3] Estimated via equation from Bashkatov et al. [2011]

[4] Estimated through data from Ripley et al. [1999]

[5] Set to this value to improve simulation speed with low impact to results.

of how “bright” the stimuli may appear to the fetus. As discussed by Isaac et al. [accepted, 2024], this interpretation is particularly useful for biologists and psychologists. To interpret the results from this perspective, we convert simulated intensities to illuminance. This can be handled in a relatively simple manner to ascertain approximate values that can be interpreted in comparison to common sources of illuminance.

Where necessary, we perform the conversion of intensity (irradiance) in units of watts/m^2 to illuminance in units of lux via the following formula [Johnsen, 2012]:

$$\text{lux} = 683.002 \cdot \int_0^\infty E\left(\lambda\right) \bar{y}\left(\lambda\right) \Delta\lambda, \tag{7.1}$$

where 683.002 is the constant representing the maximum spectral luminous efficacy and is measured in lm/W; $E\left(\lambda\right)$ is the intensity (irradiance) spectrum

Table 7.3: Optical anisotropies (g), refractive indices (n), and tissue thicknesses (t) used in Monte Carlo simulations for each medium across every wavelength, as well as the absorption [cm^{-1}] and scattering coefficients [cm^{-1}] used for the shirt medium. Note that null values are displayed for some cells because these are shown in specific separate tables. All values are sourced directly from literature where possible, though it is noted when an approximation has been made.

nm	**Shirt**	**Skin**	**Adipose**	**Muscle**	**Uterus**	**Am. Fluid**[6]
g	0.50[1]	0.90[2]	0.90[2]	0.90[2]	0.90[2]	0.99[3]
n	1.50[4]	1.40[2]	1.40[2]	1.40[2]	1.40[2]	1.35[3]
t	0.12[1]	0.20[5]	1.00[6]	0.48[7]	0.60[8]	25.00[9]
μ_a	38.00[10]	-	-	-	-	-
μ_s	25.00[1]	-	-	-	-	-

[1] Approximated.

[2] These values are used for all tissue layers. They are commonly found within ranges of those seen in literature [Scheel et al., 2018; Torricelli et al., 2001; Meglinski and Matcher, 2002; Bashkatov et al., 2005; Simpson et al., 1998].

[3] Scheel et al. [2018]

[4] Fox [1939]

[5] Torricelli et al. [2001]

[6] Commonly found within literature [Kennedy et al., 2016; D'Ambrosi et al., 2017; Hwang, 2021].

[7] Fukano et al. [2021]

[8] Durnwald and Mercer [2008]

[9] Simply chosen to provide a large packet propagation area.

[10] El-Amoudy and El-Ebissy [2014]

measured in W/m^2 per nm, which is taken from the simulation results; $\bar{y}(\lambda)$ represents either the photopic (light-adapted) or scotopic (dark-adapted) luminosity function of wavelength for humans; and the integral is taken over the spectrum of simulated wavelengths. For our single wavelength simulations, we integrate over a Dirac delta function. For the joint simulations representing natural light, we integrate across the seven simulated wavelengths. In the single wavelength scenarios, the conversion equation becomes simply

$$\mathrm{lux} = 683.002 \cdot E\left(\lambda\right) \bar{y}\left(\lambda\right). \tag{7.2}$$

7.2.1 Tissue model

All simulations conducted use a baseline model consisting of four tissue layers for the maternal tissue, a layer for amniotic fluid, and a pseudo-fetal layer. The maternal tissue is comprised of skin, adipose, muscle, and uterus. Below the uterus layer is the amniotic fluid, followed by the pseudo-fetal layer. In practice, the pseudo-fetal layer is not actually part of the tissue model — rather, it essentially acts as a detector layer to capture the residual energy carried by any photon packets which reach the simulated fetal depth, and this serves to provide an estimate on the energy reaching the fetus from light sources. Hence, the model consists of five layers and a detector layer.

A z-plane cross-section of the tissue model used in our simulations is shown in Figure 5.1. As this research focuses on exploring the impact of the visible spectrum of natural light on the uterine environment and the ability to simulate this via a discrete number of monochromatic sources, optical parameters are sourced for seven wavelengths uniformly distributed across the visible spectrum. These are shown in Tables 7.1, 7.2, and 7.3. An additional layer for clothing is later used to provide further results — these parameters are also listed in Table 7.3 and later described where necessary.

The experimental side of this research requires the stage of fetal visual development to be sufficiently advanced to detect stimuli. Therefore, presentation of the natural light is assumed to occur during the third trimester of pregnancy when the fetal brain and eye are developed enough to recognise and respond to stimuli [Donovan et al., 2020], with this being accounted for in the tissue layer geometry. We have taken layer thickness values from empirical studies, and these are also shown in Table 7.3.

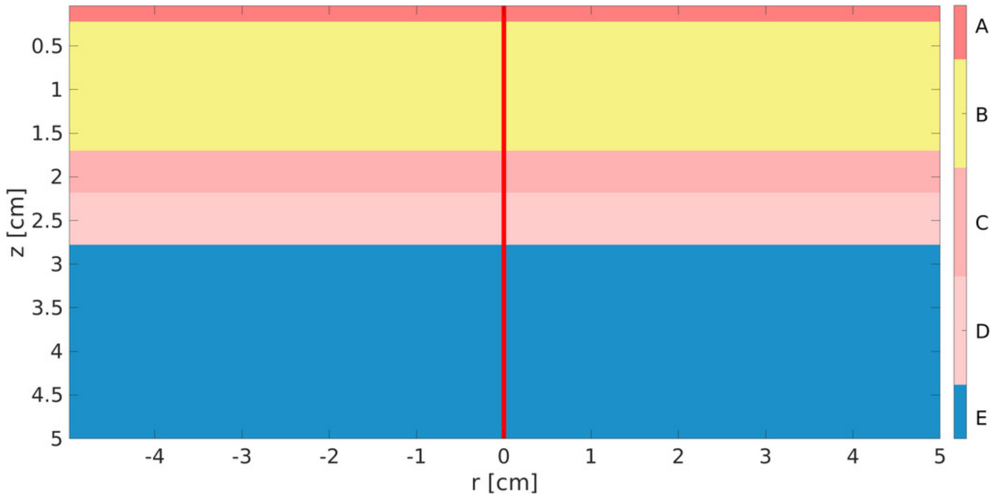

Figure 7.1: Geometry of the layered tissue model used in our Monte Carlo simulations. Layer A is skin, Layer B is adipose, Layer C is muscle, Layer D is uterus, and Layer E is amniotic fluid.

7.3 Results

We first simulate individual monochromatic point sources at uniformly distributed wavelengths across the visible spectrum. Figure 7.2 shows cross-sections in the r-z plane of the relative fluence rate (i.e., relative intensity, or watts of power incident per cm^2 per watt delivered) on a base-10 logarithmic scale for three select single beams in the range of 400 nm to 700 nm. All wavelengths were incident perpendicular to the surface of the maternal abdominal skin. Note that the geometry is presented in cylindrical coordinates for these figures and axial symmetry is assumed.

From inspection of Figure 7.2, it is evident that the wavelengths with greatest influence on light penetrating the uterus are those with higher magnitudes. One would expect the 650 nm wavelength to have the largest presence at the fetal detection layer, while the 450 nm wavelength is minimally represented.

In practice, a significant region of the tissue might be expected to receive exposure to a broader natural light source. We consequently next expand the geometric launch area for the photon packets in our simulation from that of a point source to one which encompasses the entire simulated tissue surface (a

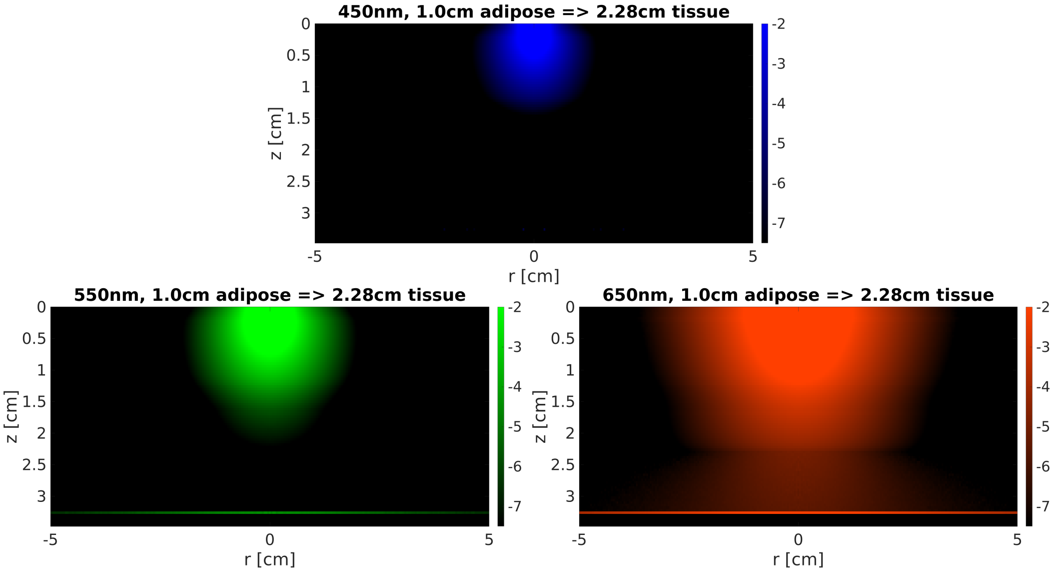

Figure 7.2: Cross-sections of relative fluence rate (i.e., relative intensity, or watts of power incident per cm^2 per watt delivered) in the r-z plane for three select single beams of differing wavelength incident at the surface of the maternal abdominal skin. Note values are presented in base-10 logarithmic scale and the geometry is here presented in cylindrical coordinates.

square region of width 10 cm). In doing so, we assume a random distribution of photon locations across the tissue surface in order to first replicate a source of natural light that is approximately uniformly distributed across the tissue. The results of this alteration can be seen via the three select wavelengths in Figure 7.3.

We next inspect the combination of these broad distributions to understand the attenuation of uniformly distributed natural light in maternal abdominal tissue. By combining data from the individual simulations shown in Figure 7.3 with those from the remaining wavelengths, we simulate the attenuation of a uniform distribution of natural light through tissue. This is shown in Figure 7.4, where the intensity of each wavelength is plotted against penetration depth. As outlined in the Discussion section, intensities have been scaled to account for a sunlight source. The intensity recorded by the fetal detector layer for each wavelength is shown in Figure 7.5. Note that the 400 nm wavelength did not reach the fetal detector layer, so it is not shown here.

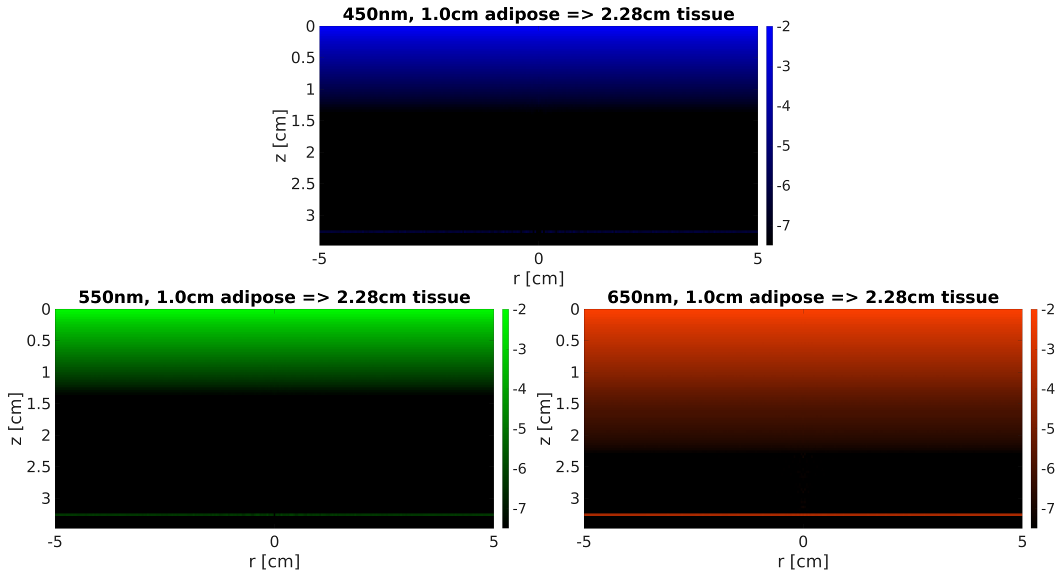

Figure 7.3: Cross-sections of relative fluence rate (i.e., relative intensity, or watts of power incident per cm^2 per watt delivered) in the r-z plane for three select broad sources of differing wavelength incident at the surface of the maternal abdominal skin. Note values are presented in base-10 logarithmic scale and the geometry is here presented in cylindrical coordinates.

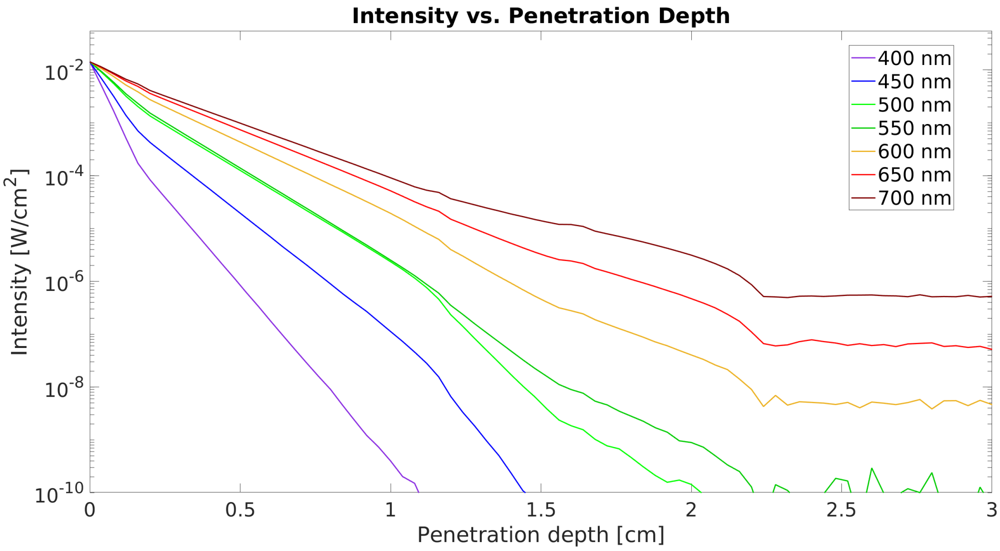

Figure 7.4: Fluence rate (i.e., intensity, or watts of power incident per cm^2) against penetration depth for the seven wavelengths simulated. As the visible spectrum is assumed to have uniform intensity, each wavelength starts from the same point before declining in intensity with penetration depth.

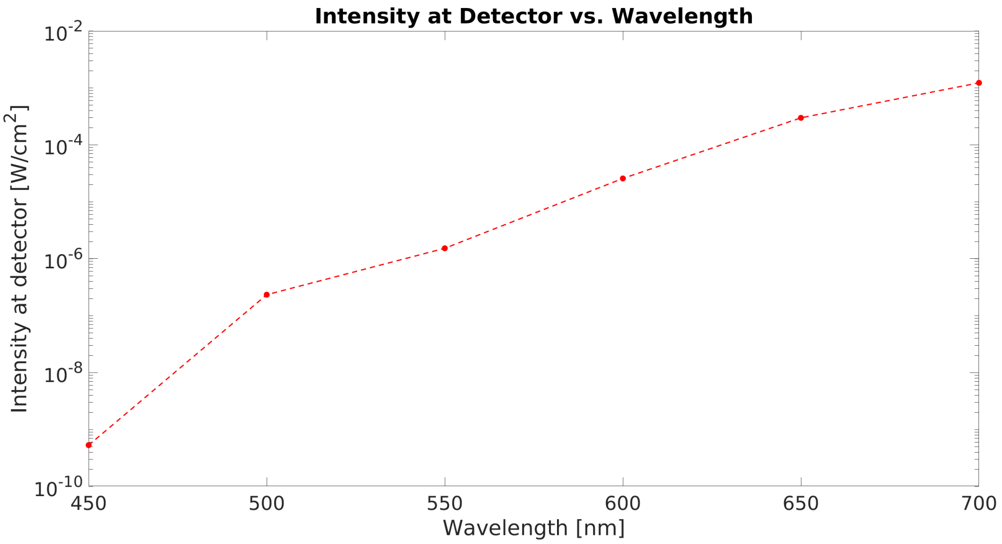

Figure 7.5: Fluence rate (i.e., intensity, or watts of power incident per cm^2) at the fetal detection layer for the seven wavelengths simulated. The 400 nm wavelength did not reach the fetal detector layer, so it is not shown in this figure.

As a final extension to our simulations, we consider the influence of a layer of fabric when placed above the tissue model. This represents a clothing layer, and its inclusion is handled by adjusting the model to include an additional layer directly above the skin layer shown in Figure 7.1. An updated visual representation of the geometry is shown in Figure 7.6. For these simulations, we approximate for the clothing layer the parameter values shown in Table 7.3. Due to the limited values found in the literature from which to base our approximations, these values are assumed equivalent across all simulated wavelengths.

Repeating the simulations for the broad light sources with such a layer of clothing above the tissue results in the output shown in Figure 7.7. Again, as further discussed in the Discussion section, these intensities have been scaled to account for the fact that the source is incident sunlight. The intensity recorded by the fetal detector layer for each wavelength is shown in Figure 7.8. Note here that wavelengths below 500 nm did not reach the fetal detector layer, so these are not shown in this figure.

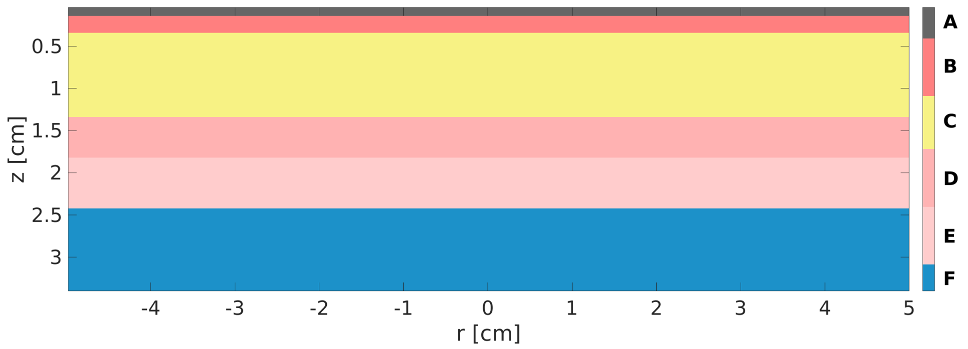

Figure 7.6: Geometry of the layered shirt and tissue model used in our Monte Carlo simulations. Layer A is shirt, Layer B is skin, Layer C is adipose, Layer D is muscle, Layer E is uterus, and Layer F is amniotic fluid.

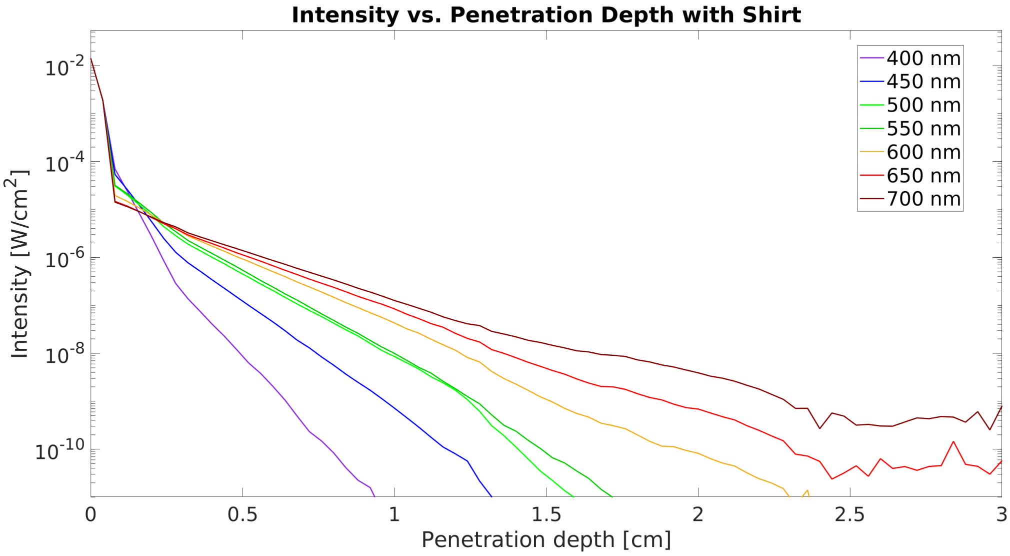

Figure 7.7: Fluence rate (i.e., intensity, or watts of power incident per cm^2) against penetration depth for the seven wavelengths simulated with a shirt above the skin. As the visible spectrum is assumed to have uniform intensity, each wavelength starts from the same point before declining in intensity with penetration depth.

7.4 Discussion

We first use MC simulations to demonstrate the relationship between increasing wavelength (across the visible spectrum of light) and the propagation of monochromatic point source laser diode stimuli presented to the maternal

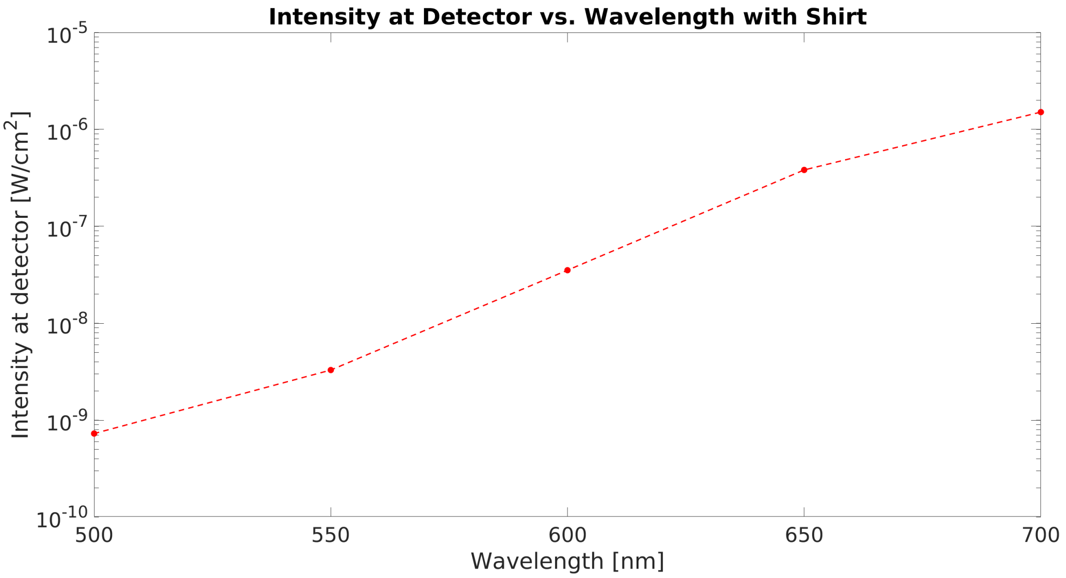

Figure 7.8: Fluence rate (i.e., intensity, or watts of power incident per cm^2) at the fetal detection layer for the seven wavelengths simulated. Wavelengths below 500 nm did not reach the fetal detector layer, so these are not shown in this figure.

abdomen and, consequently, the fetus in utero. As the wavelength of light simulated increases across the visible spectrum, light intensity levels reaching the fetus typically increase. For example, comparing the results for the 450 nm wavelength to those of the 650 nm wavelength in Figure 7.2 shows a clear increase in light intensity at increasingly greater penetration depths of the maternal tissue and amniotic fluid. Simply comparing the relative fluence rates for $r = 0$ at the fetal detection layer for the 450 nm and 650 nm point source simulations shows the latter's intensity at this point is approximately 500,000 times larger than the former. Typically, for biological tissue, one would expect penetration depth to increase with wavelength across the visible spectrum [Finlayson et al., 2022], and these results are in line with this expectation.

When considering natural light to be an approximately uniform distribution of wavelengths across the visible spectrum, one would expect a natural light point source generated from the combination of individual wavelength point sources to reflect the results of Figure 7.2. Though not demonstrated here, this concept was evident in previous work involving the delivery of monochromatic stimuli to the human fetus, with experimental applications focusing on using stimuli at the 650 nm wavelength [Isaac et al., accepted, 2024].

To more accurately simulate natural light sources, we expanded the region of photon delivery in the simulations from a point source to instead encompass the entire simulated tissue surface (i.e., a square region of width 10 cm). This provides a more realistic simulation of maternal tissue exposed to natural light, and as might be expected, the results as shown in Figure 7.3 are qualitatively similar to those in Figure 7.2. Simulations of wavelengths towards the longer end of the visible spectrum of light, when broadcast across the tissue region, result in greater tissue penetration than those of shorter wavelengths. This is to be expected as a natural continuation from the point source simulations and is evident, for example, by noting that the greatest intensity of light in Figure 7.3 reaches the fetal detection layer in the 650 nm simulation, whereas the fetal detection layer in the 450 nm simulation is relatively untouched. Similarly, the combination of individual broad simulations shown in Figure 7.4, as expected, shows the clear significance of the “redder” wavelengths at greater tissue and fluid depths. When combined with Figure 7.5, two outcomes from this work are clear: a portion of the simulated natural light reaches the fetal detection layer, and the light detected is largely dominated by the “redder” wavelengths towards the upper end of the visible spectrum.

Within each set of simulations, we implement the fetal detection layer by recording the fluence of all photon packets which propagate to a depth of 1 cm beyond the tissue-fluid interface. In essence, these photons are assumed to have reached the fetus. This represents a total penetration depth (through the tissue and fluid mediums) of 3.28 cm for these simulations. As shown by Figures 7.2 and 7.3, the detection layer is assumed, for simplicity, to be horizontal. Even though this is not an entirely realistic representation of the typical fetal orientation with respect to the uterine wall, this method has been chosen to represent the possibility of the fetal eye lying anywhere along a line at a 1 cm depth within the amniotic fluid. This method also implicitly assumes that the fetal eye is oriented directly towards the uterine wall — hence, these simulations assume the optimum orientation of the fetal eye for detection of natural light upon direct delivery to the maternal abdominal tissue. Nonetheless, this approach enables an approximate upper bound for the light which reaches the fetal eye to be determined. The fetal detection layer here, in practice, provides an estimate of the amount of light that would be processed by the fetal eye if oriented towards a source at the location where the layers of maternal abdominal tissue are thinnest (directly beneath where light is delivered orthogonally to the maternal abdomen) at an amniotic fluid depth of 1 cm.

Results thus far have explored relative light intensity through maternal tissue and amniotic fluid with an assessment of light reaching the fetus. In other words, Figures 7.2 and 7.3 display the log of incident power (in watts) per unit area (in cm^2) per unit power presented (in watts) at any given point within the simulated region, while Figures 7.4 and 7.5 display the incident power (in watts) per unit area (in cm^2). As an example, inspecting the values from Figure 7.3 at the fetal detector layer, we can find the log value for W/cm^2 per watt delivered for a given wavelength; however, as this figure represents the attenuation of natural light through maternal tissue after direct exposure to sunlight, it must be scaled accordingly. This process, which led to Figures 7.4 and 7.5, is detailed next.

A typical approximation for the intensity of solar radiation across the visible spectrum for natural light at the earth's surface is $1,000$ W/m^2 [da Rosa and Ordóñez, 2022]. Assuming this light is uniformly distributed across the seven wavelengths we have simulated, each wavelength hence has an approximate individual intensity at the earth's surface of 142.86 W/m^2 [da Rosa and Ordóñez, 2022]. We assumed direct exposure of sunlight to the abdominal region, delivered orthogonal to the exposed maternal tissue plane. Our simulated incident region was a square of width 10 cm, giving an area of 0.01 m^2 exposed to this radiation. We therefore estimate a total incident power from our visible light of 10 W across this region, with each wavelength contributing approximately 1.43 W. Combining this with the simulated data above, we may determine the simulated light intensities at the fetal detection layer, and these are shown for each wavelength in Figure 7.5. For example, the simulated fluence at the fetal layer for sunlight at the 700 nm wavelength is approximately 1.2×10^{-3} W/cm^2.

This value is a wavelength-specific measure of the intensity of natural light reaching the fetus after propagation through multi-layered maternal abdominal tissue and 1 cm of amniotic fluid; however, for our purposes, an understanding of how "bright" this attenuated natural light might appear from the perspective of the fetus is of interest. We therefore convert the simulated intensities to a measure of illuminance to interpret the overall post-attenuation brightness of natural light from this perspective. This is handled through Equation 7.1 (repeated below) to determine an approximate uterine illuminance which can then be interpreted by way of comparison to more common sources of illuminance.

$$\text{lux} = 683.002 \cdot \int_0^\infty E(\lambda)\, \bar{y}(\lambda)\, \Delta\lambda, \tag{7.1}$$

Integrating across our simulated wavelengths in this manner results in a value of approximately 1.90 lx for the unclothed simulations, which is an illuminance that falls approximately between that observed during a full moon on a clear night [Rich and Longcore, 2006] and civil twilight — the period when the geometric centre of the sun is, at most, 6° below the horizon [Elion and Elion, 1979].

Typically, the maternal abdomen is not directly exposed to sunlight. More commonly, one might expect a layer of clothing (such as a shirt) to be present. If we next consider this instance, by inspecting the values from Figure 7.8 at the fetal detector layer, we find that only the wavelengths from 500 nm and above reach this depth. Intensities range from approximately 7.28×10^{-10} W/cm^2 for the 500 nm wavelength to approximately 1.51×10^{-6} W/cm^2 for the 700 nm wavelength. Again, these values have been scaled accordingly. Hence, it can be seen that the introduction of such a clothing layer reduces the intensity of light reaching the fetal detection layer by a wavelength-dependent multiple that lies approximately between 300 and 850.

Again, these values are measures of the intensity of natural light reaching the fetus after propagation through a layer of clothing, maternal abdominal tissue, and amniotic fluid. As before, we are interested in understanding how "bright" this attenuated natural light might appear from the perspective of the fetus. After converting the simulated intensities to a single measure of illuminance, we find a value of approximately 0.0025 lx for the clothed simulations. This is approximately between the illumination provided by a clear, starry night sky and that of a quarter moon [Rich and Longcore, 2006].

Hence, our simulations suggest that the maternal abdomen (by measure of light reaching the fetal eye when oriented directly toward the uterine wall and below the orthogonal light source) may be illuminated due to incidental natural light to levels comparable to that of a clear starry sky or a quarter moon for instances where a clothing layer of 0.12 cm is present. Removing the clothing layer results in illuminances approximately between a full moon on a clear night and that of civil twilight. These results suggest that the uterine visual environment is typically not as dark as once assumed. Under optimum conditions (as simulated within), a typical fetus may undergo late-stage development within the womb in an environment that ranges from being completely dark (at night, for instance) to being relatively well-lit (for instance, if the mother was in direct sunlight with an exposed abdomen).

Beyond offering a greater understanding of the uterine visual environment, these results have relevance to future applications. In particular, ongoing work in the field of ectogenesis explores the gestation of a fetus outside the human body. Trials in recent years have shown that, for animals, it is feasible to bring an extremely premature fetus to term outside of the maternal abdomen [Partridge et al., 2017], with fetal lambs at the equivalent developmental stage to extremely premature human fetuses supported for a period of 4 weeks. With the recent FDA revision of approvals for human testing of similar products [Kozlov, 2023], the suitability of proposed products in replicating the human uterine environment may be determined as a function of the simulations reported in this work. It is clear from these results that the presence of human tissue (and thin layers of clothing) does not cause the human fetus to be restricted to development in a completely dark environment. Similarly, it does not appear to be the case that the human fetus is likely to develop in an environment that is as illuminated as, for instance, a typical indoor room under artificial lighting. Hence, the production of such proposed artificial wombs should account for the implication of this work when designing products for trial. One might conclude from these simulations that an artificial womb need not be made from material that is overly light restricting, nor material that enables a large amount of light to penetrate the artificial uterine environment — as has been previously used in animal trials [Partridge et al., 2017].

In performing these simulations, several simplifying assumptions have been made. For example, the simulations of natural light directly incident upon the maternal abdomen (and incident upon the clothed abdomen) may not accurately reflect the typical exposure of the fetus to natural light. More commonly, the fetal eye would be directed roughly perpendicular to the main natural light source. Any light that is directed toward the fetal eye may instead predominantly come from reflected light off environmental structures. In these cases, the illumination of the uterus would vary, and the consequent light reaching the fetal eye would likely be different to that approximated in this work. There is room for future studies to explore this variation in environmental conditions in order to construct a range of potential lighting conditions for the human fetus. This would further serve to grow our understanding of the uterine environment and its interface with the early stages of human visual development.

7.5 Conclusion

In this paper, we have used Monte Carlo simulations to generate quantitative data to explore the extent to which the human uterine environment is illuminated by exposure to natural light. We utilise our own model for photon propagation through maternal abdominal tissue, developed in line with common algorithms within the field. Results suggest that the uterus is illuminated to a noticeable degree from direct exposure of the maternal abdomen to such lighting, and the introduction of clothing layers may still result in a partial illumination of the womb. In combination with previous results [Isaac et al., accepted, 2024], it can be surmised that the intensity of natural light (and consequent illuminance) eventually delivered to the fetus would vary strongly with maternal abdominal adipose thickness. For the assumed tissue thicknesses employed within this paper, our simulations show that direct maternal abdominal exposure to natural light can result in a uterine illuminance comparable to a level between that of a full moon on a clear night and civil twilight. Introducing a layer of clothing akin to a typical shirt reduces simulated illuminance to levels more comparable to that of a quarter moon.

These results have strong implications for future work in ectogenesis, where the feasibility of an artificial uterus for the human fetus is currently being explored and has been found to be possible for live lamb infants [Partridge et al., 2017]. Any such work will need to carefully consider the material and structure of the artificial uterine system, particularly to accurately replicate the potential range of uterine visual conditions that the third trimester human fetus likely experiences during gestation. The work performed within this paper provides an initial starting point for research in this field.

References

A. N. Bashkatov, E. A. Genina, V. I. Kochubey, and V. V. Tuchin. Optical properties of the subcutaneous adipose tissue in the spectral range 400–2500 nm. *Optics and Spectroscopy*, 99:836–842, 2005.

A. N. Bashkatov, E. A. Genina, and V. V. Tuchin. Optical properties of skin, subcutaneous, and muscle tissues: a review. *Journal of Innovative Optical Health Sciences*, 04(01):9–38, 2011.

R. M. Bradley and C. M. Mistretta. Fetal sensory receptors. *Physiological Reviews*, 55(3):352–382, 1975.

H. Buiteveld, J. Hakvoort, and M. Donze. Optical properties of pure water. *Proc. SPIE 2258, Ocean Optics*, XII, 01 1994.

A. V. da Rosa and J. C. Ordóñez. Chapter 12 - Solar Radiation. In A. V. da Rosa and J. C. Ordóñez, editors, *Fundamentals of Renewable Energy Processes (Fourth Edition)*, pages 519–576. Academic Press, Oxford, fourth edition edition, 2022.

F. D'Ambrosi, F. Crovetto, E. Colosi, I. Fabietti, F. Carbone, B. Tassis, S. Motta, A. Bulfoni, L. Fedele, G. Rossi, and N. Persico. Maternal Subcutaneous and Visceral Adipose Ultrasound Thickness in Women with Gestational Diabetes Mellitus at 24-28 Weeks' Gestation. *Fetal Diagnosis and Therapy*, 43(2):143–147, 06 2017.

M. Del Giudice. Alone in the Dark? Modeling the Conditions for Visual Experience in Human Fetuses. *Developmental Psychobiology*, 53:214–219, 2011.

T. Donovan, K. Dunn, A. Penman, R. J. Young, and V. M. Reid. Fetal eye movements in response to a visual stimulus. *Brain and Behavior*, 10(8): e01676, 2020.

K. Dunn, N. Reissland, and V. M. Reid. The functional foetal brain: A systematic preview of methodological factors in reporting foetal visual and auditory capacity. *Developmental Cognitive Neuroscience*, 13:43–52, 2015.

C. P. Durnwald and B. M. Mercer. Myometrial thickness according to uterine site, gestational age and prior cesarean delivery. *The Journal of Maternal-Fetal & Neonatal Medicine*, 21(4):247–250, 2008.

E. S. El-Amoudy and A. A. El-Ebissy. Comparison between the optical properties of cotton and wool fabrics dyed with a natural dye using different mordents. *Materials Science: An Indian Journal*, 10, 2014.

G. R. Elion and H. A. Elion. Electro-optics handbook. 1979.

L. Finlayson, I. R. M. Barnard, L. McMillan, S. H. Ibbotson, C. T. A. Brown, E. Eadie, and K. Wood. Depth penetration of light into skin as a function of wavelength from 200 to 1000 nm. *Photochemistry and Photobiology*, 98 (4):974–981, 2022.

K. R. Fox. Refractive indices of textile fibres: Double variation method for the determination of. *Textile Research*, 10(2):79–93, 1939.

M. Fukano, Y. Tsukahara, S. Takei, S. Nose-Ogura, T. Fujii, and S. Torii. Recovery of abdominal muscle thickness and contractile function in women after childbirth. *International Journal of Environmental Research and Public Health*, 18(4):1–9, February 2021.

M. S. Hwang. Abdominal skin subcutaneous fat thickness over the gestational period in korean pregnant women: a descriptive observational study. *Korean Journal of Women Health Nursing*, 27(4):318–325, 2021.

Z. Isaac, J. Heerikhuisen, and V. Reid. The effect of adipose tissue on transdermal monochromatic light presented to the human fetus using Monte Carlo simulations. *Scientific Reports - Nature*, accepted, 2024.

S. Jacques, D. Weaver, and S. Reppert. Penetration of Light Into the Uterus of Pregnant Mammals. *Photochemistry and Photobiology*, 45:637 – 641, 01 1987.

S. Johnsen. *The optics of life: A biologist's guide to light in nature*. Princeton University Press, 01 2012.

N. J. Kennedy, M. J. Peek, A. E. Quinton, V. Lanzarone, A. Martin, R. Benzie, and R. Nanan. Maternal abdominal subcutaneous fat thickness as a predictor for adverse pregnancy outcome: a longitudinal cohort study. *BJOG: An International Journal of Obstetrics & Gynaecology*, 123(2):225–232, 2016.

M. Kozlov. Human trials of artificial wombs could start soon. Here's what you need to know. *Nature*, 621:458–460, 09 2023.

J. Lecanuet and B. Schaal. Fetal sensory competencies. *European Journal of Obstetrics & Gynecology and Reproductive Biology*, 68(1):1–23, 1996.

A. W. Liley. The foetus as a personality. *Australian & New Zealand Journal of Psychiatry*, 6(2):99–105, 1972.

I. V. Meglinski and S. J. Matcher. Quantitative assessment of skin layers absorption and skin reflectance spectra simulation in the visible and near-infrared spectral regions. *Physiological Measurement*, 23(4):741, oct 2002.

M. Myowa-Yamakoshi and H. Takeshita. Do Human Fetuses Anticipate Self-Oriented Actions? A Study by Four-Dimensional (4D) Ultrasonography. *Infancy*, 10(3):289–301, 2006.

E. Partridge, M. Davey, M. Hornick, P. McGovern, A. Mejaddam, J. Vrecenak, C. Burgos, A. Olive, R. Caskey, T. Weiland, J. Han, A. Schupper, J. Connelly, K. Dysart, J. Rychik, H. Hedrick, W. Peranteau, and A. Flake. An extra-uterine system to physiologically support the extreme premature lamb. *Nature Communications*, 8:15112, 05 2017.

S. Rao, C. Chun, J. Fan, J. M. Kofron, M. B. Yang, R. S. Hegde, N. Ferrara, D. R. Copenhagen, and R. A. Lang. A direct and melanopsin-dependent fetal light response regulates mouse eye development. *Nature*, 494:243–246, 2013.

V. M. Reid, K. Dunn, R. J. Young, J. Amu, T. Donovan, and N. Reissland. The Human Fetus Preferentially Engages with Face-like Visual Stimuli. *Current Biology*, 27:1825–1828, 03 2017.

V. M. Reid, K. Dunn, T. Donovan, and R. J. Young. Response to Scheel et al. *Current Biology*, 28(10):R596–R597, 2018.

C. Rich and T. Longcore. *Ecological Consequences of Artificial Night Lighting*. 01 2006.

P. M. Ripley, J. G. Laufer, A. D. Gordon, R. J. Connell, and S. G. Bown. Near-infrared optical properties of ex vivo human uterus determined by the Monte Carlo inversion technique. *Physics in Medicine & Biology*, 44(10): 2451–62, oct 1999.

A. M. Scheel, S. J. Ritchie, N. J. L. Brown, and S. L. Jacques. Methodological problems in a study of fetal visual perception. *Current Biology*, 28(10): R594–R596, 2018.

Y. Shimojo, T. Nishimura, H. Hazama, T. Ozawa, and K. Awazu. Measurement of absorption and reduced scattering coefficients in Asian human epidermis, dermis, and subcutaneous fat tissues in the 400- to 1100-nm wavelength range for optical penetration depth and energy deposition analysis. *Journal of Biomedical Optics*, 25, 2020. URL `https://api.semanticscholar.org/CorpusID:217531532`.

C. R. Simpson, M. Kohl, M. Essenpreis, and M. Cope. Near-infrared optical properties of ex vivo human skin and subcutaneous tissues measured using the Monte Carlo inversion technique. *Physics in Medicine & Biology*, 43(9): 2465–78, sep 1998.

C. Starr. *Biology: Concepts and Applications.* Thomson, Brooks/Cole, 2005.

A. Torricelli, A. Pifferi, P. Taroni, E. Giambattistelli, and R. Cubeddu. In vivo optical characterization of human tissues from 610 to 1010 nm by time-resolved reflectance spectroscopy. *Physics in Medicine & Biology*, 46(8): 2227–37, jul 2001.

L. Wang and J. Yu. Chapter 1 - Principles of photocatalysis. In J. Yu, L. Zhang, L. Wang, and B. Zhu, editors, *S-scheme Heterojunction Photocatalysts*, volume 35 of *Interface Science and Technology*, pages 1–52. Elsevier, 2023.

L. Wang, S. L. Jacques, and L. Zheng. MCML — Monte Carlo modeling of light transport in multi-layered tissues. *Computer Methods and Programs in Biomedicine*, 47(2):131–146, 1995.

M. B. Yang, S. Rao, D. R. Copenhagen, and R. A. Lang. Length of day during early gestation as a predictor of risk for severe retinopathy of prematurity. *Ophthalmology*, 120(12):2706–2713, 2013.

Chapter 8

Third Paper Motivation

In the previous chapter, we explored the interactions of natural light with maternal abdominal tissue both with and without a typical skin covering [Isaac et al., under review, 2024]. As an extension from our original model in Chapter 5, this work still assumed a simple planar, homogeneous tissue environment with a layered tissue system. Clearly, there are practical limitations to this approach — primarily, the absence of curvature in the model ignores potential impacts to uterine illumination from light entering the maternal abdomen from all angles, as well as limiting the insight derived from the model's outputs. We know, for instance, that the thicknesses of layers such as adipose tissue are not consistent across the maternal abdomen — for example, one might typically expect a thinner layer of adipose near the anterior abdominal wall, with the layer thickening with increasing distance from this point. Similarly, this geometric variation in thickness would itself be expected to change over the course of gestation, yet our previous model does not include variation in the uterine environment due to maternal factors.

Hence, the transition from a Monte Carlo model of light propagation through simple, homogeneous maternal abdominal tissue to a more complex Monte Carlo model of the human womb, encompassing multiple non-planar layers of tissue with light entering from various directions, is motivated by the imperative to more accurately capture the intricacies of the intrauterine environment. While initial Monte Carlo simulations provided valuable insights into light-tissue interactions within the maternal abdomen [Isaac et al., accepted, 2024], they inherently oversimplified the structural and optical complexities of the womb [Isaac et al., under review, 2024]. By extending the model to encompass the heterogeneous nature of uterine tissue and the non-planar geometry of the womb, we seek to bridge the gap between theoretical simulations and the anatomical reality of intrauterine conditions.

Moreover, this expansion is motivated by the pivotal role played by light in moderating various physiological processes within the womb. Uterine illumination may serve as a potent environmental factor in fetal visual development; however, our previous models did not account for the many entry points across the curved abdomen for light to penetrate the womb, thereby limiting our understanding of its nuanced effects on the uterine visual environment. By incorporating the complexities of non-planar tissue layers and multidirectional light sources from all regions surrounding the womb into Monte Carlo simulations, we may begin to unravel the intricate interplay between light exposure and the uterine environment — as well as accounting for the temporal evolution of this interplay across gestation by, for instance, adjusting the layer thickness ratios across the abdomen.

As our previous work presents, to our knowledge, the first such computational modelling focused entirely on understanding the relationship between external light sources and the maternal abdomen to determine the consequent illumination of the womb and potential fetal visual experience, the subsequent chapter shall continue to explore new areas within this field through its extensions. This will be fundamental in laying the foundational work for our future research in this area, as well as providing a platform for other researchers, practitioners, and experimentalists to build from in their own work towards understanding the interplay between light, the human womb, and the fetal visual system.

Hence, in Chapter 9, we outline a further extension to the model that introduces curvature to the simulated womb. In doing so, we allow for the variation of layer thicknesses across the abdomen (and temporally, across gestation), as well as modifying our simulations to account for light entering the curved uterus from across the womb to more accurately simulate typical levels of uterine illumination.

References

Z. Isaac, J. Heerikhuisen, and V. Reid. The effect of adipose tissue on transdermal monochromatic light presented to the human fetus using Monte Carlo simulations. *Scientific Reports - Nature*, accepted, 2024.

Z. Isaac, J. Heerikhuisen, and V. Reid. Modeling the propagation of natural light to the human womb using Monte Carlo simulations. *Proceedings of the Royal Society B*, under review, 2024.

Chapter 9

Modeling the full human uterine visual environment with curvature

9.1 Introduction

The human fetus develops within a uterine environment exposed to many sensory stimuli. Much research has previously been devoted to outlining the extent to which the fetus can be stimulated through auditory and olfactory means [Bradley and Mistretta, 1975; Lecanuet and Schaal, 1996]. Despite previous assumptions of darkness during gestation [Myowa-Yamakoshi and Takeshita, 2006] indicating that the fetal visual environment is typically devoid of the necessary stimuli to facilitate visual experience [Liley, 1972], suggesting that fetal visual experiences are non-existent within the womb, recent research has shown that the fetal brain is capable of responding to light by the third trimester of pregnancy [Donovan et al., 2020]. Similarly, the fetus itself will respond with eye motion when presented with transdermal light stimuli via the maternal abdomen [Dunn et al., 2015] and exhibits a preference for face-like stimuli [Reid et al., 2017].

Despite growing evidence to support notions that the fetal visual environment is not as dark as previously assumed, research into the precise appearance of the uterine interior when exposed to exterior light sources is limited. To our knowledge, from the sparse literature on this topic, the work of Del Giudice [2011] provides the only quantitative modelling (apart from our own - e.g., Isaac et al. [accepted, 2024]) that assesses the visual environment for the human fetus — and under a range of everyday conditions, with results suggesting that many fetuses may develop in an environment providing sufficient illumination of the uterine cavity for visual experience.

More recently, researchers have modeled the appearance of laser diode stimuli after delivery to the exterior maternal abdomen and propagation through maternal tissue to the fetus. In response to the experimental work of Reid et al. [2017], wherein point source stimuli were determined to "fan out" in a uniform manner before reaching the fetus, Scheel et al. [2018] presented results from a Monte Carlo model of photon propagation through tissue to demonstrate the more likely resultant photon attenuation. In a similar manner, the work of Isaac et al. [accepted, 2024] introduced a bespoke Monte Carlo model designed for simulation of light propagation through maternal tissue, with a specific focus on exploring the image and uterine illumination eventually delivered to the fetus after maternal exposure to a transdermal monochromatic laser diode point source. This work also outlined the relationship between eventual intensity delivered to the fetus and maternal abdominal adipose tissue thickness, with simulations showing that the human fetus may observe the illumination from laser diode stimuli to be comparable to that of a full moon in clear skies (when simulated with 1 cm of adipose tissue).

Continuing their prior work, Isaac et al. [under review, 2024] expanded their model to allow for simulation of natural light incident on the maternal abdomen and irradiation of the maternal abdomen via a wide natural light source. This work was the first to estimate the illuminance of the uterine environment under direct sunlight, with simulated uterine illumination being comparable to that of civil twilight for abdominal exposure without a shirt and to a quarter moon for exposure with a shirt.

Although the body of research exploring the illumination of the uterine environment is expanding, previous efforts to estimate the impact of external light sources have each had notable drawbacks.

The work of Del Giudice [2011] utilised multiple regression methods based on avian tissue samples to determine coefficients for light transmission. This approach provided a static snapshot of a particular set of tissue parameters that are not directly comparable to living human tissue, resulting in limited potential for application of the work. In a similar manner, extensions of the findings were made difficult due to the model's inability to account for variations in tissue type and composition across individuals.

The work of Scheel et al. [2018], though more accurately implemented than that of Del Giudice [2011], was limited to a single application. Also, the authors employed a one-layer tissue model with the maternal abdominal tissue assumed to be homogeneous; however, this is not the case in reality. Rather, tissue is composed of several constituent layers, and each layer has its own optical parameters that govern the propagation of light through the medium. Assuming the maternal tissue to be a homogeneous medium may provide a good initial approximation of light reaching the fetus, but it will omit physically accurate effects due to constituent tissue layers having differing optical parameters. It also does not allow for variations in layer thicknesses, restricting applicability across individuals.

Isaac et al. [accepted, 2024] and Isaac et al. [under review, 2024] sought to improve on previous modelling efforts in determining uterine illumination under exposure from monochromatic stimuli and natural light. Though these works offered new insights into the uterine visual environment, two clear aspects were missing from the models. First, the maternal abdomen is not a flat surface as assumed by both models. Although an approximation of tissue as being locally flat allows for simple simulation of specific sources, this ignores the effects of abdominal curvature on, for instance, reflection and refraction of incident light. Second, a planar tissue layer environment is only applicable to the maternal abdomen in limited instances. In practice, aspects of maternal abdominal tissue (such as thickness) vary both geometrically as one moves across the abdomen and temporally as fetal growth throughout pregnancy causes the abdomen to expand.

The human womb serves as the cradle for fetal development during pregnancy, and understanding the distribution of light within this region is crucial for various biomedical applications. For instance, in obstetrics, accurate assessment of fetal and uterine oxygenation levels via light penetration is vital for monitoring fetal health and predicting pregnancy outcomes (as an example, see Wang et al. [2022]). Similarly, in phototherapy treatments for conditions such as intrauterine growth restriction (IUGR) or preeclampsia (for instance, see Charan Digal et al. [2021]), precise knowledge of light distribution within the maternal abdomen is essential for optimizing treatment efficacy while minimizing potential risks to the mother and developing fetus. Further, current work in ectogenesis explores the feasibility of artificial wombs [Partridge et al., 2017], yet the extent to which light penetrates the uterine wall and how the resultant illumination evolves over the course of gestation is not fully known. This is important for understanding the development of the fetal visual system, amongst other issues (such as determining the appropriate level of light to expose a fetus to within an artificial womb).

Hence, to more accurately model the uterine illumination of the pregnant human and the consequent visual experience of the human fetus, in this paper, we present an updated three-dimensional Monte Carlo model tailored for investigating light propagation to the uterus. Our model represents a significant advancement over previous planar works in this area by incorporating the inherent curvature of the maternal abdomen, thus providing a more anatomically accurate representation of the environment. Additionally, our model introduces the capability to vary tissue thicknesses across the maternal abdomen, allowing for a more comprehensive exploration of light-tissue interactions in this dynamic environment. This enables, for example, a variation of adipose thickness across both time and space to model the dynamics of gestation.

In the following sections, we first outline the algorithm of our Monte Carlo model, highlighting its novel features and demonstrating its utility in investigating various aspects of light transport in the pregnant human body. Through comprehensive simulations, we then showcase the initial capabilities of our model in advancing our understanding of maternal-fetal physiology and its potential applications in clinical practice and biomedical research.

9.2 Methodology

The model builds on the algorithm employed by Isaac et al. [accepted, 2024] and Isaac et al. [under review, 2024], which itself was inspired by that of MCML [Wang et al., 1995]. The program first reads in an input file describing the tissue layers, their optical parameters, the light source, and several further simulation variables. A voxelated tissue region is then generated to model a three-dimensional womb with curvature, and photons are launched into this medium.

Though there have been many approaches to modelling curvature in tissue geometries (see, for example, Margallo-Balbás and French [2007], Shen and Wang [2010], or Ren et al. [2013]), we instead here choose to continue with using a voxelated approach. Use of the voxelated approach requires less reworking of our existing model to achieve desired results, as well as being more readily flexible in terms of customization of the model's physical and optical characteristics. Due to the difficulties associated with defining curved surfaces with cubes, this method may encounter issues with accurately mapping specific tissue boundaries. Adjusting the resolution by reducing the voxel dimensions, however, begins to account for this inadequacy. In any case, we generate a region of cube-shaped voxels before overlaying several ellipsoidal shapes atop the voxels. These ellipsoids represent an initial approximation of the shape of the maternal abdomen and its constituent tissue layers, with the general equation used as follows:

$$\frac{(x+x_c)^2}{(a+x_w)^2}+\frac{(y+y_c)^2}{(b+y_w)^2}+\frac{(z+z_c)^2}{(c+z_w)^2}=1. \tag{9.1}$$

Within this equation, the parameters x_c, y_c, and z_c allow for movement of the ellipsoid's center. The parameters a, b, and c represent the semi-axis lengths (in practice, these serve as initial "widths" of the ellipsoids in the x, y, and z directions, respectively). The parameters x_w, y_w, and z_w are not necessarily a requirement for the ellipsoids to serve their purpose; however, they are included within the equation to allow for variation in widths between the concentric ellipsoids away from the designated abdominal size defined by a, b, and c.

Hence, through careful manipulation of this ellipsoid equation, we can approximate the shape of curved tissue regions of the maternal abdomen. An example cross-section in the z-x plane is shown in Figure 9.1, where the values used for the outer ellipse (for instance) are $x_c = 0$, $y_c = 0$, $z_c = -15$, $a = 15$, $b = 14$, $c = 13$, and $x_w = y_w = z_w = 0$. These values have been chosen to model the dimensions of a late-stage pregnancy (perhaps third trimester) and are approximately based on maternal abdominal measurements taken during our research group's experimental work, where these tissue thicknesses were measured via ultrasound.

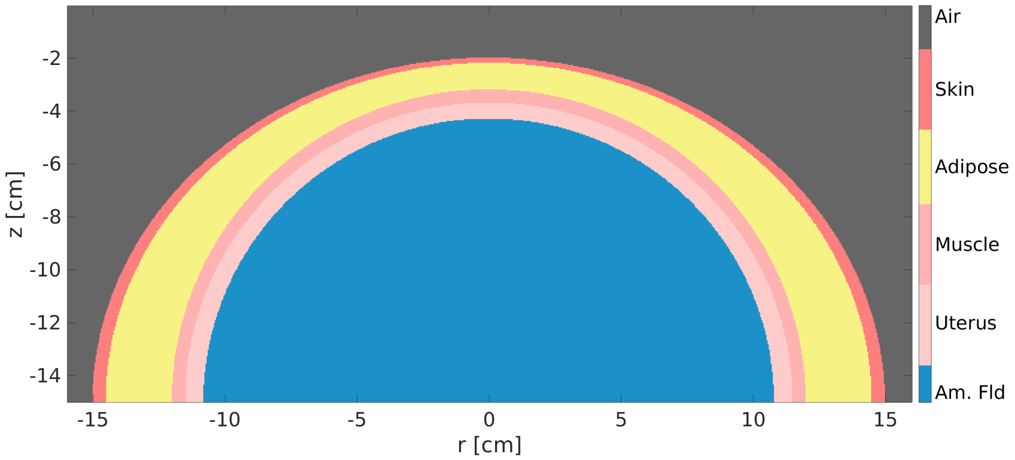

Figure 9.1: Geometry of the curved tissue model used in our Monte Carlo simulations.

By defining ellipsoids to serve as boundaries between tissue layers, we introduce a simple way to map the designated layers onto the voxelated tissue region. Each ellipsoid defines a boundary and the location of a voxel with respect to each ellipsoid defines its tissue medium, which in turn allows the ellipsoids to be assigned differing optical parameters.

The model then proceeds in a similar manner to that described by Isaac et al. [accepted, 2024]. Photons are launched with a random (but approximately uniform) distribution across the simulated abdomen as packets with random, medium-specific path lengths. Each packet is assigned a direction, and the model simulates its propagation through to a tissue interaction site. As outlined by Isaac et al. [accepted, 2024] and Isaac et al. [under review, 2024], we make use of the Henyey-Greenstein phase function [Henyey and Greenstein, 1941] in modelling the distribution of photon scattering angles:

$$p(\theta) = \frac{1}{4\pi}\frac{1-g^2}{\left(1+g^2-2g\cos(\theta)\right)^{\frac{3}{2}}}. \tag{9.2}$$

The azimuthal angle is sampled from a uniform distribution across the interval 0 to 2π.

With each step of a photon packet, the model determines whether the movement will cause the packet to interact with a boundary, and if so, which boundary. This is determined by calculating the nearest intersection point of the packet's current trajectory (modelled as a straight line) with the abdominal ellipsoids. Once the appropriate ellipsoid is determined, the packet steps to the boundary and transmission and reflection is determined via the Fresnel equations (for example, see [Smith, 2013]):

$$\begin{aligned}
r_\perp &= -\frac{\sin(\theta_i-\theta_t)}{\sin(\theta_i+\theta_t)} && (9.3)\\
t_\perp &= +\frac{2\sin(\theta_t)\cos(\theta_i)}{\sin(\theta_i+\theta_t)} && (9.4)\\
r_\parallel &= +\frac{\tan(\theta_i-\theta_t)}{\tan(\theta_i+\theta_t)} && (9.5)\\
t_\parallel &= +\frac{2\sin(\theta_t)\cos(\theta_i)}{\sin(\theta_i+\theta_t)\cos(\theta_i-\theta_t)}. && (9.6)
\end{aligned}$$

Packets are then removed from the simulation via a roulette method, as described by Isaac et al. [accepted, 2024]. All procedures loop until the designated number of packets have been simulated to completion. As with our previous work, we again implement parallel processing of photon trajectories via Message Passing Interface (MPI). In contrast to the work of Isaac et al. [under review, 2024a,b], all simulations are here conducted with 0.10 cm voxels (as opposed to the previous 0.04 cm). This value has been chosen to balance reduced computation time with marginal impacts to resolution.

9.2.1 Tissue Model

Following Isaac et al. [under review, 2024a,b], we again utilise a four-layer tissue model for our simulations of the curved womb, with the tissue layers comprising of skin, adipose, muscle, and uterus, followed by an inner region of amniotic fluid. An example cross-section in the z-r plane of our curved tissue geometry is presented in Figure 9.1.

Each tissue layer has a variable thickness dependent on abdominal position, as described by ellipsoids produced via Equation 9.1. The minimum thickness for each layer is assumed to be located at the front of the abdomen (i.e., $r = 0$ in Figure 9.1), while the maximum layer thicknesses are assumed to be at the sides of the abdomen (i.e., $r = 15$ in Figure 9.1). This information, as well as the specific values used for each ellipsoidal layer, is listed in Table 9.1. The optical properties of each tissue layer for each wavelength are presented in Tables 9.2, 9.3, and 9.4.

For the purposes of this work, we are interested in understanding how the uterine environment, with curvature, is impacted by external sources of light that are incident across the exterior of the maternal abdomen. We present three initial monochromatic cases from across the visible spectrum of light to demonstrate the effects: 450 nm, 550 nm, and 650 nm incident broad light sources. We also replicate the work of Isaac et al. [accepted, 2024] from an alternative perspective by simulating a point source delivered to the maternal abdomen. Lastly, we investigate the differences in simulated fluence between a late-stage gestation womb and an early-stage gestation womb.

Table 9.1: Parameters used for each ellipsoidal surface, as given by Equation 9.1. The values t_a and t_s represent the consequent layer thicknesses (in cm) at the womb's apex and at its sides, respectively. All t_a values have been approximated in line with results from our research group's experimental work, while all t_s values are estimated.

x	**Skin**	**Adipose**	**Muscle**	**Uterus**	**Am. Fluid**
$x_c = y_c$	0.00	0.00	0.00	0.00	0.00
z_c	15.00	15.00	15.00	15.00	15.00
$a = b$	15.00	15.00	15.00	15.00	15.00
c	13.00	13.00	13.00	13.00	13.00
$x_w = y_w$	0.00	-0.50	-3.00	-3.50	-4.20
z_w	0.00	-0.20	-1.20	-1.70	-2.30
t_a	0.20	1.00	0.50	0.60	-
t_s	0.50	2.50	0.50	0.70	-

9.3 Results

We inspect first the situation where the maternal abdomen is directly exposed to a broad, monochromatic light source. Three such instances are modeled (450 nm, 550 nm, and 650 nm), and each source is directed along the z-axis so that photons are oriented perpendicular to the line running tangent to the womb's apex (i.e., they are oriented such that $u_z = -1$). The outputs are shown in Figure 9.2 — note that these are cross-sections in the x-z plane along the y axis, which is assumed to run vertically down the centre of the body. In principle, we may view similar cross-sections along any line from the generated womb simulation; however, the central plane is of primary interest

Table 9.2: Absorption coefficients [cm^{-1}] used in simulations for each wavelength (listed as, and measured in, nm) and medium. All values are sourced directly from literature where possible, though estimations are noted where made.

nm	**Skin**[1]	**Adipose**[2]	**Muscle**[3]	**Uterus**[4]	**Am. Fluid**[5]
450	2.50	2.00	5.67	1.26	0.0004
550	1.25	1.40	2.65	0.70	0.0008
650	0.50	0.70	1.00	0.32	0.003

[1] Estimated through data from Bashkatov et al. [2005]

[2] Estimated through data from Bashkatov et al. [2005] and Shimojo et al. [2020]

[3] Estimated through data from Simpson et al. [1998]

[4] Estimated through data from Ripley et al. [1999]

[5] Calculated from Buiteveld et al. [1994], with temperature set to $37.9°C$.

and illustrates the overall outcomes of the model. Note also that a cross-section in the y-z plane would look qualitatively similar due to the symmetry assumed in the ellipsoids. Following results by Isaac et al. [under review, 2024], we find a notable difference in penetration depth and resultant light reaching the uterine cavity. This, in turn, follows a known physical effect [Finlayson et al., 2022].

We have previously presented monochromatic point source stimuli to a planar tissue region to understand the resultant illumination of the uterine cavity and the potential visual experience for the fetus [Isaac et al., accepted, 2024]. Here, we replicate this work in the simulated womb with curvature, with the result for a 650 nm point source delivered directly downwards at the maternal abdomen shown in Figure 9.3. Again, this figure represents a cross-section of the womb, taken at $y = 0$.

In addition to extending the womb to a full environment with curvature, we also inspect our results from an alternative perspective. In particular, recording the direction of photons upon entry to the womb allows for external

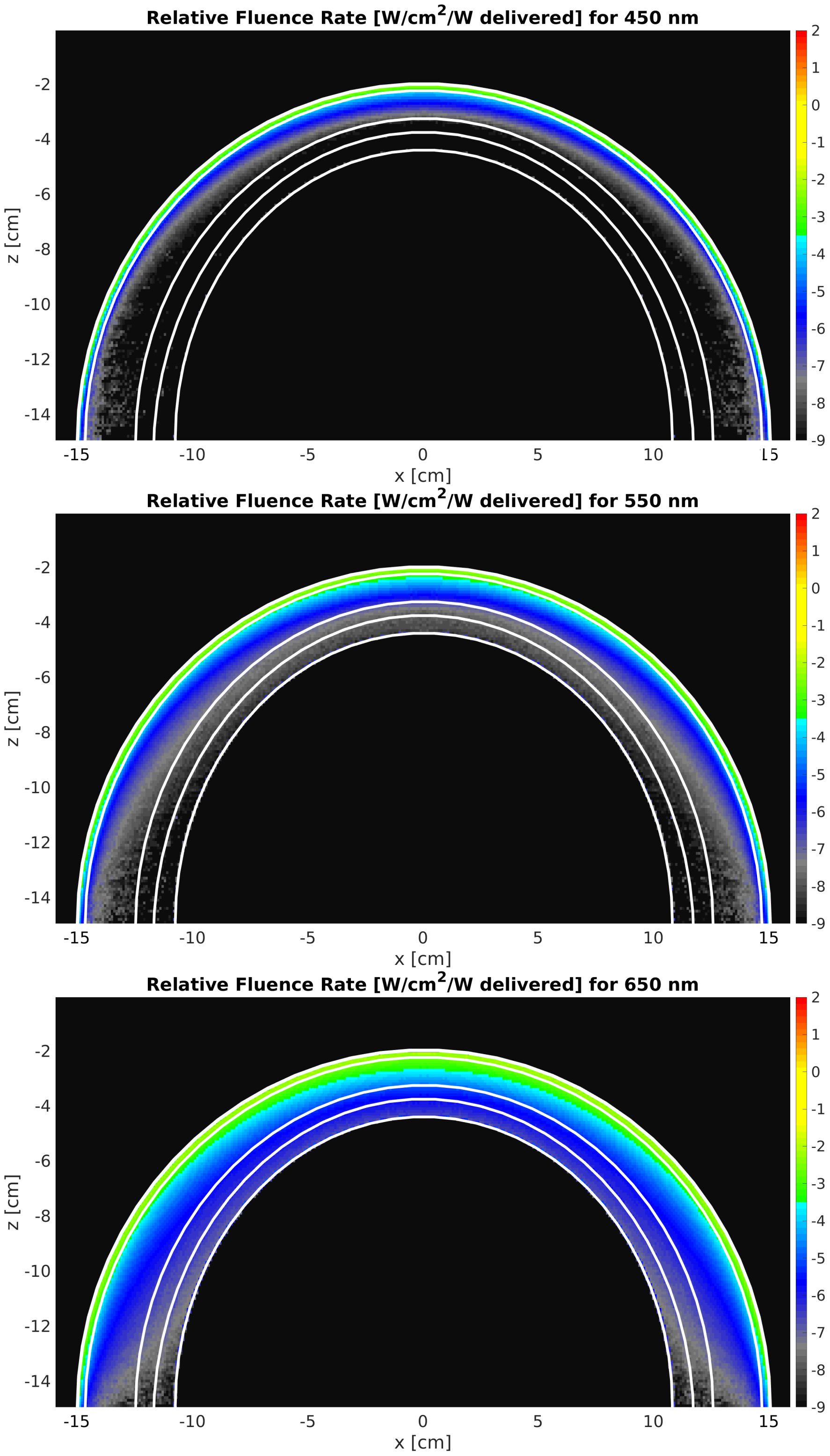

Relative Fluence Rate [W/cm^2/W delivered] for 450 nm

Relative Fluence Rate [W/cm^2/W delivered] for 550 nm

Relative Fluence Rate [W/cm^2/W delivered] for 650 nm

Figure 9.2: Cross sections of the curved womb environment, showing relative fluence (i.e., watts of power incident per cm^2 per W delivered) for 450 nm, 550 nm, and 650 nm light incident perpendicular to the womb's apex, distributed across the womb. Values are presented in base-10 logarithmic scale and white lines represent the boundaries between layers as described in Table 9.1.

Table 9.3: Scattering coefficients [cm^{-1}] used in simulations for each wavelength (listed as, and measured in, nm) and medium. All values are sourced directly from literature where possible, though estimations are noted where made.

nm	**Skin**[1]	**Adipose**[2]	**Muscle**[3]	**Uterus**[4]	**Am. Fluid**[5]
450	460.46	165.00	129.48	171.40	1.00
550	304.11	144.00	104.98	152.60	1.00
650	238.89	128.43	88.17	137.00	1.00

[1] Estimated via equation from Bashkatov et al. [2005]

[2] Estimated through data from Bashkatov et al. [2005]

[3] Estimated via equation from Bashkatov et al. [2011]

[4] Estimated through data from Ripley et al. [1999]

[5] Set to this value to improve simulation speed with observed low impact to results. Also taken from Gunther et al. [2021].

Table 9.4: Optical anisotropies (g) and refractive indices (n) used in simulations for each medium and wavelength. All values are sourced directly from literature where possible, though estimations are noted where made.

x	**Skin**[1]	**Adipose**[1]	**Muscle**[1]	**Uterus**[1]	**Am. Fluid**[2]
g	0.90	0.90	0.90	0.90	0.99
n	1.40	1.40	1.40	1.40	1.35

[1] These values are used for all tissue layers. They are commonly found within ranges of those seen in literature [Scheel et al., 2018; Torricelli et al., 2001; Meglinski and Matcher, 2002; Bashkatov et al., 2005; Simpson et al., 1998].

[2] Scheel et al. [2018]

light sources to be interpreted in a manner that more effectively describes the eventual light reaching the fetal eye. In previous work, we have simply recorded

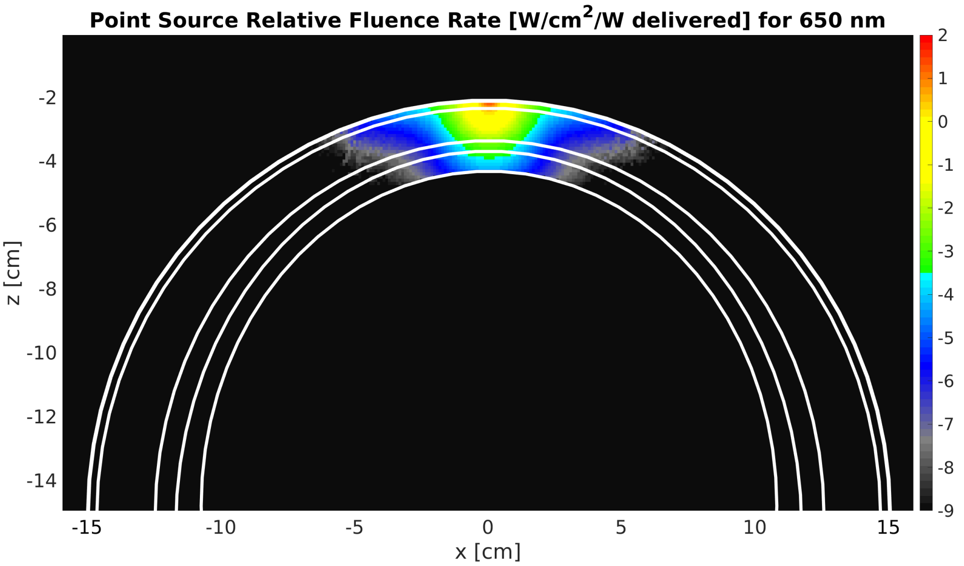

Figure 9.3: A cross section of the curved womb environment, showing the relative fluence (i.e., relative intensity, or watts of power incident per cm^2 per W delivered) for 650 nm light incident perpendicular to the womb's apex, simulated as a point source delivered at the origin. Note values are presented in base-10 logarithmic scale and white lines displayed represent the boundaries between layers as described in Table 9.1.

any photons reaching a "detector layer" as a proxy for photons reaching the fetal eye [Isaac et al., under review, 2024]; however, this omits the possibility of photons reaching the eye's depth but being oriented in a manner that does not result in direct incidence upon the fetal eye. By recording the direction of each photon packet upon entry to the uterus, and through acknowledging that amniotic fluid's high anisotropy (0.99 [Scheel et al., 2018]) and low interaction coefficient (~1.003 for 650 nm light, from Table 9.4) results in photons typically propagating onwards in their direction of entry, we are able to present an additional perspective.

In Figure 9.4, we present a plot of photon packet directions upon entry to the uterus, binned by θ and ϕ for the instance where a 650 nm point source is delivered to the abdominal apex. Directions are binned in terms of θ and ϕ, where θ is measured from the x-axis running across the womb's greatest depth and ϕ is measured from the y-axis running down the body. Consequently, a binning of $(\theta, \phi) = (90, 90)$ indicates a photon packet travelling parallel to the z-axis, and this corresponds to the simulated peak values in this environment. The combination of any two coordinates (such as a grid cell on Figure 9.4) thus indicates a direction of light upon reaching the uterine wall's interior, and the value shown at that point indicates the level of light travelling in that direction upon reaching the uterus.

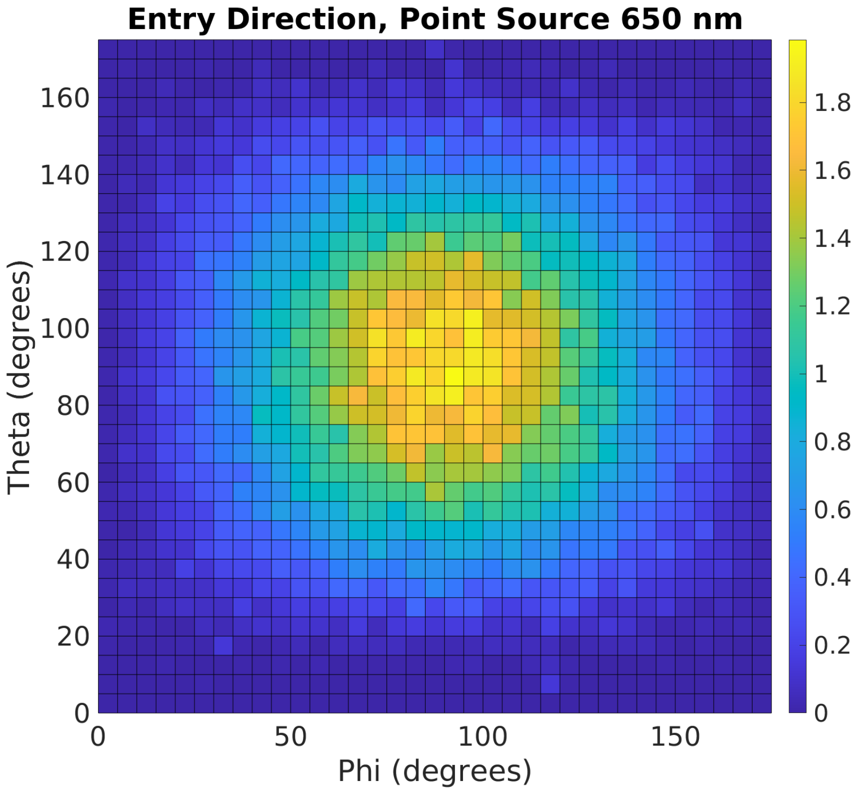

Figure 9.4: Relative fluence (i.e., relative intensity, or watts of power incident per cm^2 per W delivered) of photon packet directions upon entry to the womb for a 650 nm point source incident perpendicular to the tissue at the womb's apex. Theta is the angle measured from the positive x-axis, while phi is the angle measured from the positive y-axis. Any pairing thus specifies a direction of entry.

Lastly, to better understand the temporal relationship between uterine illumination and the maternal abdomen, we adjust our ellipsoids to represent a pregnancy in an earlier stage of gestation (perhaps second or early-third trimester). The updated geometry for this environment is shown in Figure 9.5,

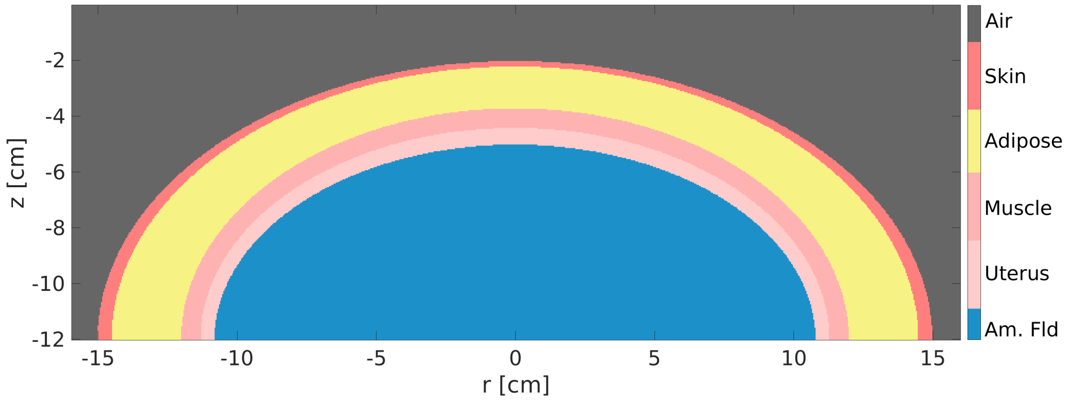

Figure 9.5: Geometry of the early-gestation curved tissue model used in our Monte Carlo simulations.

and the precise parameter values and variable layer thicknesses are described in Table 9.5. These have been assumed, with the only enforced requirements being that abdominal size reduces in the z-direction (compared to the previous geometry) and layer thicknesses are larger at the apex than those used in the late-gestation simulation to represent reduced tissue thinning.

We again simulate both a broad distribution of 650 nm light across the abdominal region and a point source of 650 nm light presented to the abdominal apex. Results are presented in Figures 9.6 and 9.7, respectively, alongside equivalent outputs from the late-gestation simulations.

9.4 Discussion

We have extended our previous work from a planar tissue environment capable of simulating monochromatic point source stimuli [Isaac et al., accepted, 2024] or broad sources of natural light [Isaac et al., under review, 2024] to one where the curvature of the womb is accounted for across all tissue layers and the influence of stimuli may be inspected in a more physically accurate manner. Light may reach the uterus both from source regions perpendicular to the maternal abdomen (such as the apex of the womb) and from areas where the incidence of light against the outer layers of tissue is approximately parallel to the surface tissue (such as on the far edges of the womb). In practice, simula-

Table 9.5: Parameters used for each early-gestation ellipsoidal surface, as given by Equation 9.1. The values t_a and t_s represent the consequent layer thicknesses (in cm) at the womb's apex and at its sides, respectively. All t_a and t_s values have been estimated.

x	**Skin**	**Adipose**	**Muscle**	**Uterus**	**Am. Fluid**
$x_c = y_c$	0.00	0.00	0.00	0.00	0.00
z_c	12.00	12.00	12.00	12.00	12.00
$a = b$	15.00	15.00	15.00	15.00	15.00
c	10.00	10.00	10.00	10.00	10.00
$x_w = y_w$	0.00	-0.50	-3.00	-3.70	-4.30
z_w	0.00	-0.20	-1.70	-2.40	-3.00
t_a	0.20	1.50	0.70	0.60	-
t_s	0.50	2.50	0.70	0.60	-

tions such as those performed for this work are essentially approximations of how light interfaces with the maternal abdomen in situations such as a person sunbathing.

Further, however, the extension of our model to this more physically accurate environment offers an insight into the geometric variation of illumination across the uterine cavity. For instance, nearer to the front of the simulated womb, we have designated tissue layers with reduced thickness to replicate the "thinning" of tissue in these regions. Similarly, in areas to the side of the uterine cavity, we have accounted for increased tissue thickness. This can be observed in our results — for example, Figure 9.2 clearly demonstrates from a macroscopic viewpoint the greater intensities of light penetrating to larger depths towards the front of the uterine cavity (though some of this effect is also due to the differing incident angles of photon packets at the tissue surface). This aligns with our expectations of reality, based upon observations of tissue

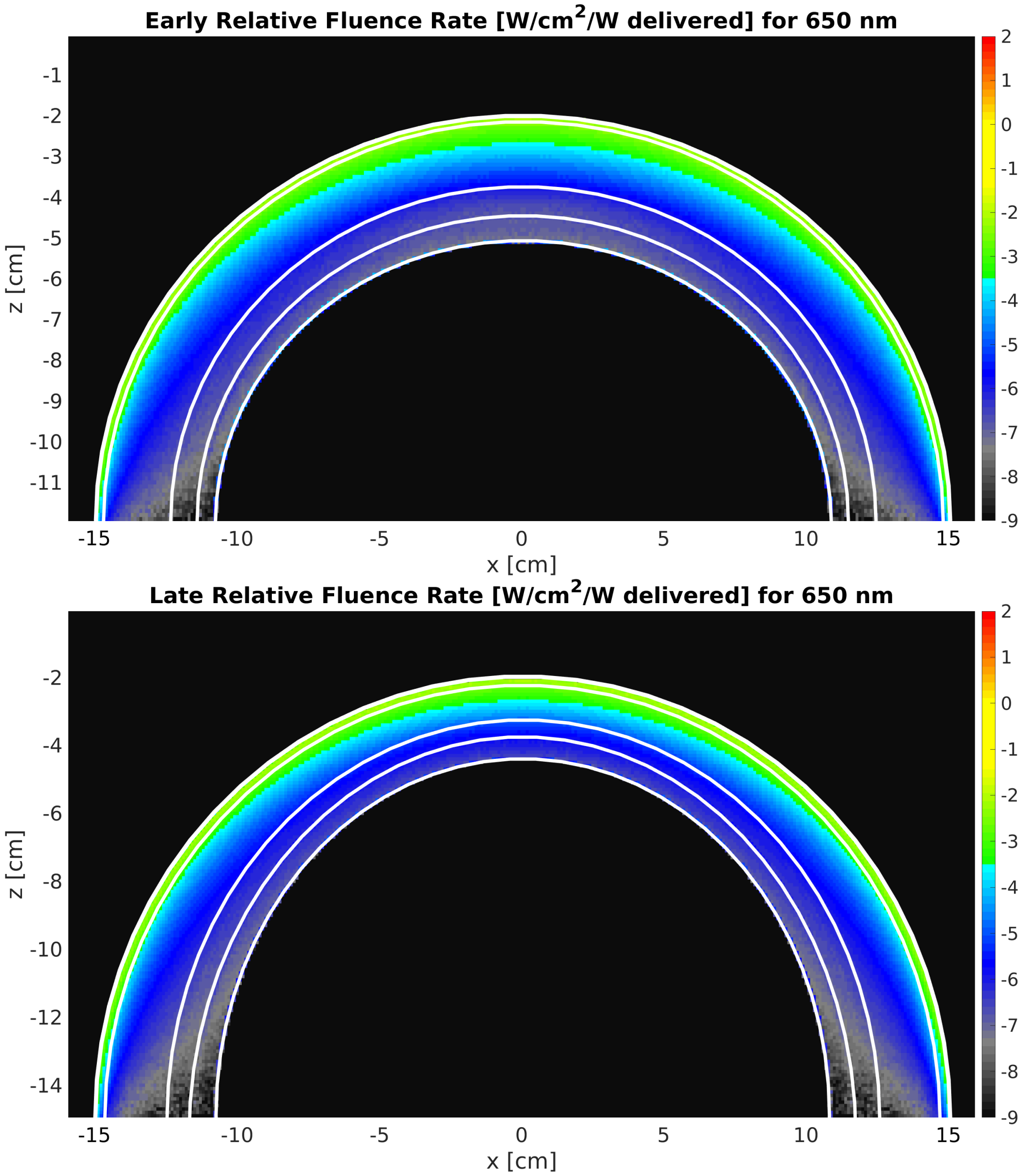

Figure 9.6: Comparison between an assumed early-gestation womb and late-gestation womb over cross sections of the curved womb environment. Each plot shows the simulated relative fluence (i.e., relative intensity, or watts of power incident per cm^2 per W delivered) for 650 nm light incident perpendicular to the womb's apex, distributed across the womb. Note values are presented in base-10 logarithmic scale and white lines displayed here represent the boundaries between layers as described in Tables 9.1 and 9.5.

density variations across the abdomen.

The introduction of an "interior" fetal perspective wherein we are able to in-

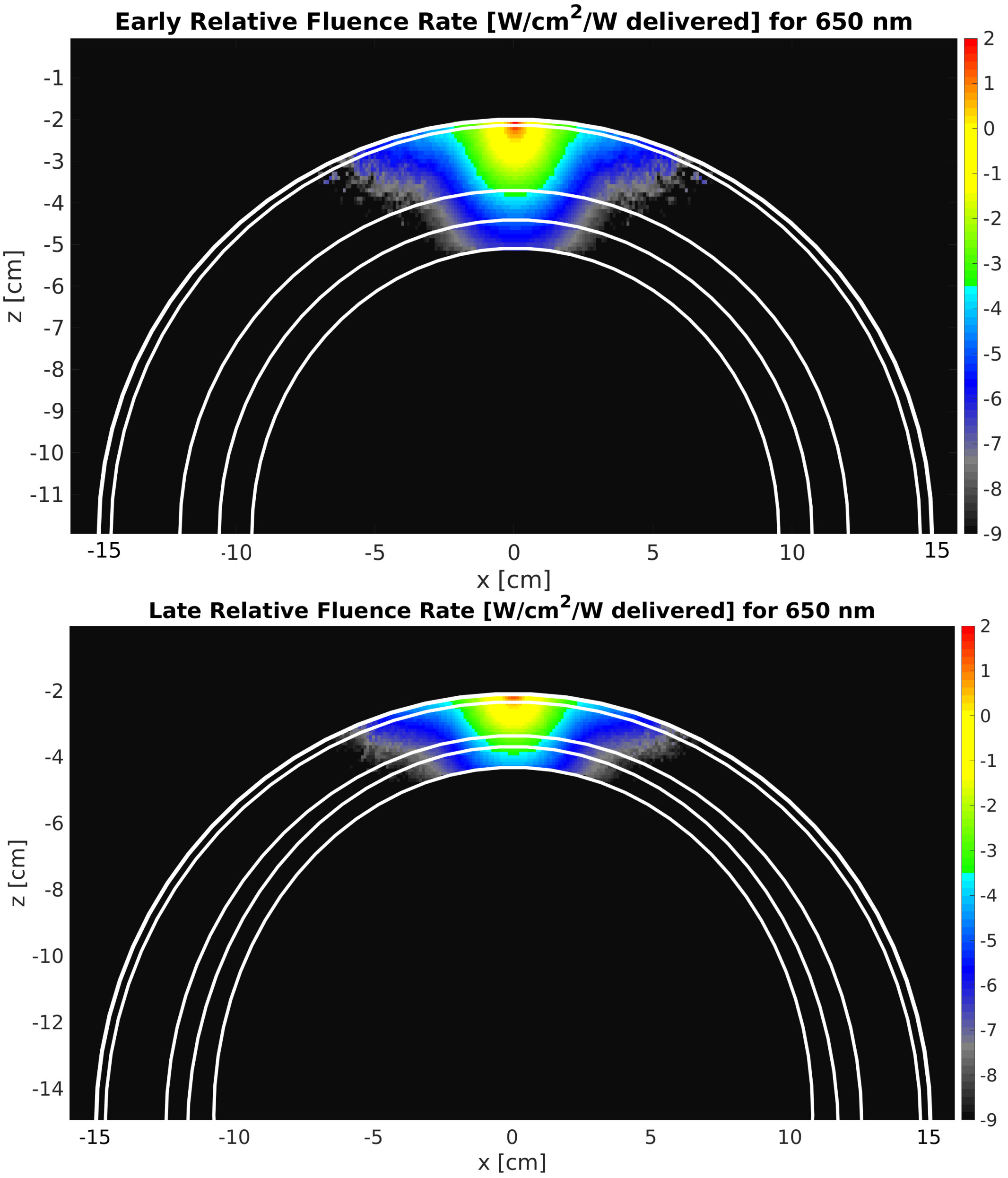
Early Relative Fluence Rate [W/cm^2/W delivered] for 650 nm

Late Relative Fluence Rate [W/cm^2/W delivered] for 650 nm

Figure 9.7: Comparison between an assumed early-gestation womb and late-gestation womb over cross sections of the curved womb environment. Each plot shows the simulated relative fluence (i.e., relative intensity, or watts of power incident per cm^2 per W delivered) for 650 nm point source light incident perpendicular to the womb's apex. Note values are presented in base-10 logarithmic scale and white lines displayed here represent the boundaries between layers as described in Tables 9.1 and 9.5.

spect the directions of photons entering the uterus provides an additional frame of analysis. Figure 9.4 showed this for a point source delivered perpendicular to the apex of the womb's exterior. Due, in part, to the initial orientation of the simulated source, most of the photons consequently enter the uterus approximately parallel to the z-axis; however, a relatively smooth decline can be seen as one moves away from the z-axis, representing the decreased numbers of photons entering at angles more perpendicular to the z-axis. This is both due to the initial orientation of the stimuli and the highly forward-scattering nature of biological tissue [Tuchin, 2007]. The value of the anisotropy of all simulated tissue layers was 0.9 here, which results in scattering events not causing the photon packets to significantly deviate from their initial orientation. Hence, we can conclude that, although a stimulus directed perpendicular to the maternal abdomen's surface is likely to experience intensity diffusion radially outwards from its point of incidence, a reasonably large proportion of the light will still enter the uterus in the direction of delivery.

This information is particularly useful for researchers in the field of fetal vision, as it indicates the degree to which fetal eyes can reasonably be directed away from the stimuli delivery point while still having light enter the uterus in a direction that will reach their eye. For a stimulus delivered perpendicular to the womb's apex, for example, fetuses whose eyes are oriented more than 30° away from this point are predicted by this model to receive less than approximately 70% of the light intensity transmitted along the axis of delivery. Increasing the orientation to 60° from the axis of delivery reduces delivered intensity to less than approximately 25% of the transmitted light intensity.

It is worth noting that the choice of ellipsoids to simulate the multi-layered environment of the maternal abdomen holds an additional benefit for our purposes. In practice, the temporal evolution of the uterine environment over the course of gestation is an aspect that our modelling to date has been incapable of broadly accounting for without running multiple simulations across different regions of the womb. We know, for instance, that in the early stages of gestation, tissue thickness across the abdomen may typically be larger due to the smaller size of the fetus. In contrast, later stages of gestation where the fetus has grown and reoriented itself will typically exhibit markedly different tissue variation across the womb, with certain regions featuring reduced tissue. With our model as demonstrated, we may alter the precise layer thicknesses both at the apex of the womb (via adjusting, for example, the values of a, b, and c to manipulate the fixed semi-axis lengths of ellipsoids) and toward the edges of the region (via adjusting, for example, the values of the x_t and y_t parameters to account for greater tissue thicknesses in these directions). Geometric asymmetries may also be modeled via disproportional adjustments of the x_c, y_c, and z_c parameters if so desired.

Inspecting the results of Figure 9.6 demonstrates the benefit of this work, with a clear difference in delivered intensity evident. Following intuition (and the results of Isaac et al. [accepted, 2024]), the increased tissue thickness in the early stages of gestation largely reduces the levels of light reaching the uterus. Using the parameters employed for this work, the shift from an early-stage gestation's abdomen to a late-stage gestation's abdomen (such as that shown in Figure 9.6) results in approximately 10 times the light intensity reaching the uterus at the apex. Though this does not necessarily lead to a significant increase in uterine illumination due to the nature of light intensity's relationship with illuminance, as noted by Isaac et al. [accepted, 2024], such differences can result in shifts comparable to moving from the illumination of a clear, starry night sky to that of a full moon under clear conditions. Further work is required to ascertain exactly what differences in uterine illumination are present across gestation; however, these results provide a strong foundation from which to continue to build.

Indeed, it is possible within this new environment to introduce additional parameters to account explicitly for the temporal aspect of pregnancy. For example, if we were to alter the general ellipsoid equation shown in Equation 9.1 via the introduction of a parameter W which ranges from 0 to 40 to represent the number of weeks pregnant, we may allow the possibility to define fixed tissue thicknesses (through our other parameters) at varying points across the abdomen that remain consistent despite expansion of the womb as W increases. An example of such a possible extension is shown in Equation 9.7. This may thus be a method to simply represent the temporal nature of pregnancy, with the possibility to explore the range of environmental conditions presented to the fetus from external lighting as W varies.

$$\frac{(x+x_c)^2}{\frac{W}{40}(a+x_w)^2}+\frac{(y+y_c)^2}{\frac{W}{40}(b+y_w)^2}+\frac{(z+z_c)^2}{\frac{W}{40}(c+z_w)^2}=1. \tag{9.7}$$

Overall, this simple approach to modelling the maternal abdomen via a series of roughly concentric ellipsoids provides an elementary starting point for modelling the curved womb, yet it introduces the possibility for many future research applications. Within this chapter, we have explored and compared the exposure of the entire womb to high and low wavelength monochromatic light sources, we have introduced an additional interior perspective of optical stimuli, and we have compared the results of late-stage gestation to a proposed early-stage gestation. However, there are many future avenues through which we can extend this research and improve on its accuracy and applicability.

Firstly, the temporal aspects of pregnancy and the resultant variations in tissue density across the abdomen warrant further exploration. This would primarily serve to improve our understanding of how this environmental evolution affects the interplay between light and tissue and the resultant uterine illumination experienced by the human fetus.

In a similar manner, further extension of the model to account for natural light is a clear next step. In Chapter 7, we combined monochromatic stimuli from across the visible spectrum of light to simulate the interactions between natural light and maternal abdominal tissue and the resultant uterine illumination; however, this was for a planar tissue medium [Isaac et al., under review, 2024]. Here, we explored the interplay between monochromatic stimuli and the curved womb; however, we have not yet explored the overall influence of natural light from across the visible spectrum as approximated by a summation over individual wavelengths. This would be a fitting extension to our previous exploration of the influence of natural light on the uterine environment — especially when coupled with the introduction of curved clothing layers to the model to represent the impact of a typical item of clothing.

In contrast to the proposed future extensions, there are also several limitations to the model as it is currently presented, each of which requires future research to explore and improve further. One such example is the absence of any interior anatomical structures beyond the tissue layers included. In reality, light does not simply enter the womb through tissue alone. Rather, there will be some light which, for instance, enters the uterine cavity toward the sides of the abdomen where it is partially obscured by the ribcage and other such structures. Additionally, the model as it is currently presented does not explicitly account for heterogeneities such as blood vessels within the tissue medium — in practice, the individually homogeneous tissue layers are assumed to implicitly replicate the presence of these structures on average.

A further extension in a similar vein to those discussed above concerns maternal anatomical variation during gestation. In particular, changes in pregnancy during the third trimester of pregnancy lead to the layer of muscle precisely at the abdominal apex reducing to the point where there is little (or even no) muscle present. As discussed further by, for example, Gilleard and Brown [1996], the maternal muscle structure stretches and separates during the late stages of pregnancy due to the growth of the fetus. Consequently, models that include a layer of muscle at the abdominal apex may overestimate the attenuation of light from this direction. As a result, future developments of the model may consider a more physically accurate iteration of the modelled uterus. This model would necessarily then feature no muscle for a region along the line mapped upon the womb's exterior by the midsagittal (or median) plane of the maternal abdomen (in late-stage gestation simulations).

In principle, these considerations could be included within future expansions of our voxelated tissue environment; however, their exact implementation will require careful analysis, research, and simulation to accurately account for physical shapes and structures, appropriate medium-specific optical parameters, and anatomically correct locations. Similarly, there is scope to explore whether the uterine cavity is influenced in any way by light entering the body from the posterior half of the abdomen, though this is likely to be minimal due to the large abundance of anatomical structures obscuring the womb from this angle.

9.5 Conclusion

In this chapter, we have introduced a large-scale expansion to our previous planar model of multi-layer maternal tissue. Due to the entirely new direction of modelling being explored by both this extension and its application, this represents a large shift forward in our work — from both the sense of novelty and physical accuracy, but also from the future research scope introduced by these changes.

Clearly, the introduction of curvature to the model results in variations in light intensity reaching the uterus from incident light across the abdomen, with more light entering the front of the womb than at the sides. Further, modelling different stages of gestation can be undertaken both simply and in a physically accurate manner via this expansion. Future work intends to more deeply explore such environments, alongside modelling the effects of introducing isolated heterogeneities within the tissue medium (such as the ribcage).

Additionally, analysing the direction of light upon entry to the uterus allows for a greater understanding of how light interfaces with maternal tissue in order to reach the fetus. This is valuable for future experimental purposes and further opens research avenues in modelling specific experimental stimuli. An understanding of the degree to which the fetal eye's orientation with respect to the delivered stimuli affects the delivered intensity is crucial for experimental design and data interpretation — both of which are areas wherein this model can provide useful insights.

References

A. N. Bashkatov, E. A. Genina, V. I. Kochubey, and V. V. Tuchin. Optical properties of the subcutaneous adipose tissue in the spectral range 400–2500 nm. *Optics and Spectroscopy*, 99:836–842, 2005.

A. N. Bashkatov, E. A. Genina, and V. V. Tuchin. Optical properties of skin, subcutaneous, and muscle tissues: a review. *Journal of Innovative Optical Health Sciences*, 04(01):9–38, 2011.

R. M. Bradley and C. M. Mistretta. Fetal sensory receptors. *Physiological Reviews*, 55(3):352–382, 1975.

H. Buiteveld, J. Hakvoort, and M. Donze. Optical properties of pure water. *Proc. SPIE 2258, Ocean Optics*, XII, 01 1994.

K. Charan Digal, P. Singh, Y. Shrivastava, J. Chaturvedi, A. Kumar Tyagi, and S. Basu. Effects of delayed cord clamping in intrauterine growth–restricted neonates: a randomized controlled trial. *European Journal of Pediatrics*, 180, 06 2021.

M. Del Giudice. Alone in the Dark? Modeling the Conditions for Visual Experience in Human Fetuses. *Developmental Psychobiology*, 53:214–219, 2011.

T. Donovan, K. Dunn, A. Penman, R. J. Young, and V. M. Reid. Fetal eye movements in response to a visual stimulus. *Brain and Behavior*, 10(8): e01676, 2020.

K. Dunn, N. Reissland, and V. M. Reid. The functional foetal brain: A systematic preview of methodological factors in reporting foetal visual and auditory capacity. *Developmental Cognitive Neuroscience*, 13:43–52, 2015.

L. Finlayson, I. R. M. Barnard, L. McMillan, S. H. Ibbotson, C. T. A. Brown, E. Eadie, and K. Wood. Depth penetration of light into skin as a function of wavelength from 200 to 1000 nm. *Photochemistry and Photobiology*, 98 (4):974–981, 2022.

W. L. Gilleard and J. M. M. Brown. Structure and Function of the Abdominal Muscles in Primigravid Subjects During Pregnancy and the Immediate Postbirth Period. *Physical Therapy*, 76(7):750–762, 07 1996.

J. Gunther, B. Jayet, A. Jacobs, R. Burke, J. Kainerstorfer, and S. Andersson-Engels. Effect of the presence of amniotic fluid for optical transabdominal fetal monitoring using Monte Carlo simulations. *Journal of Biophotonics*, 14, 06 2021.

L. G. Henyey and J. L. Greenstein. Diffuse radiation in the Galaxy. *The Astrophysical Journal*, 93:70–83, January 1941.

Z. Isaac, J. Heerikhuisen, and V. Reid. The effect of adipose tissue on transdermal monochromatic light presented to the human fetus using Monte Carlo simulations. *Scientific Reports - Nature*, accepted, 2024.

Z. Isaac, J. Heerikhuisen, and V. Reid. Modeling the propagation of natural light to the human womb using Monte Carlo simulations. *Proceedings of the Royal Society B*, under review, 2024.

J. Lecanuet and B. Schaal. Fetal sensory competencies. *European Journal of Obstetrics & Gynecology and Reproductive Biology*, 68(1):1–23, 1996.

A. W. Liley. The foetus as a personality. *Australian & New Zealand Journal of Psychiatry*, 6(2):99–105, 1972.

E. Margallo-Balbás and P. J. French. Shape based Monte Carlo code for light transport in complex heterogeneous tissues. *Opt. Express*, 15(21):14086–14098, Oct 2007.

I. V. Meglinski and S. J. Matcher. Quantitative assessment of skin layers absorption and skin reflectance spectra simulation in the visible and near-infrared spectral regions. *Physiological Measurement*, 23(4):741, oct 2002.

M. Myowa-Yamakoshi and H. Takeshita. Do Human Fetuses Anticipate Self-Oriented Actions? A Study by Four-Dimensional (4D) Ultrasonography. *Infancy*, 10(3):289–301, 2006.

E. Partridge, M. Davey, M. Hornick, P. McGovern, A. Mejaddam, J. Vrecenak, C. Burgos, A. Olive, R. Caskey, T. Weiland, J. Han, A. Schupper, J. Connelly, K. Dysart, J. Rychik, H. Hedrick, W. Peranteau, and A. Flake. An extra-uterine system to physiologically support the extreme premature lamb. *Nature Communications*, 8:15112, 05 2017.

V. M. Reid, K. Dunn, R. J. Young, J. Amu, T. Donovan, and N. Reissland. The Human Fetus Preferentially Engages with Face-like Visual Stimuli. *Current Biology*, 27:1825–1828, 03 2017.

S. Ren, X. Chen, H. Wang, X. Qu, G. Wang, J. Liang, and J. Tian. Molecular Optical Simulation Environment (MOSE): A Platform for the Simulation of Light Propagation in Turbid Media. *PLOS ONE*, 8:e61304, 04 2013.

P. M. Ripley, J. G. Laufer, A. D. Gordon, R. J. Connell, and S. G. Bown. Near-infrared optical properties of ex vivo human uterus determined by the Monte Carlo inversion technique. *Physics in Medicine & Biology*, 44(10): 2451–62, oct 1999.

A. M. Scheel, S. J. Ritchie, N. J. L. Brown, and S. L. Jacques. Methodological problems in a study of fetal visual perception. *Current Biology*, 28(10): R594–R596, 2018.

H. Shen and G. Wang. A tetrahedron-based inhomogeneous Monte Carlo optical simulator. *Physics in Medicine and Biology*, 55(4):947–962, jan 2010.

Y. Shimojo, T. Nishimura, H. Hazama, T. Ozawa, and K. Awazu. Measurement of absorption and reduced scattering coefficients in asian human epidermis, dermis, and subcutaneous fat tissues in the 400- to 1100-nm wavelength range for optical penetration depth and energy deposition analysis. *Journal of Biomedical Optics*, 25, 2020. URL `https://api.semanticscholar.org/CorpusID:217531532`.

C. R. Simpson, M. Kohl, M. Essenpreis, and M. Cope. Near-infrared optical properties of ex vivo human skin and subcutaneous tissues measured using the Monte Carlo inversion technique. *Physics in Medicine & Biology*, 43(9): 2465–78, sep 1998.

D. G. Smith. *Field Guide to Physical Optics*, pages 30–31. Field Guides. SPIE Press, 2013.

A. Torricelli, A. Pifferi, P. Taroni, E. Giambattistelli, and R. Cubeddu. In vivo optical characterization of human tissues from 610 to 1010 nm by time-resolved reflectance spectroscopy. *Physics in Medicine & Biology*, 46(8): 2227–37, jul 2001.

V. V. Tuchin. *Tissue Optics*, pages 132–142. SPIE, 2007.

L. Wang, S. L. Jacques, and L. Zheng. MCML — Monte Carlo modeling of light transport in multi-layered tissues. *Computer Methods and Programs in Biomedicine*, 47(2):131–146, 1995.

L. Wang, J. Cochran, T. Ko, W. Baker, K. Abramson, L. He, D. Busch, V. Kavuri, R. Linn, S. Parry, A. Yodh, and N. Schwartz. Non-invasive monitoring of blood oxygenation in human placentas via concurrent diffuse optical spectroscopy and ultrasound imaging. *Nature Biomedical Engineering*, 6(9):1017–1030, September 2022.

Chapter 10

Conclusion

10.1 Introduction

In this final chapter, we assess the overall contributions and results of this thesis. We begin with an initial discussion of the primary findings and their contributions to the field, before then analysing the limitations present in the work alongside improvements yet to be incorporated within the model. Finally, we conclude this thesis with a discussion on possible directions and pathways for future work and extensions to the modelling performed within.

10.2 Discussion and Contributions

The field of tissue optics is vast, with abundant research and literature existing on topics ranging from work exploring the distribution of light incident on arteries [Keijzer et al., 1989] to investigations into the optimum number of tissue layers to include when modelling [Das et al., 2020] to experimental research on animals with connections to humans [Jacques et al., 2008]. Many topics have been explored within this field, yet there is a clear gap in the literature when considering the interplay between light and maternal abdominal tissue, the illumination of the uterus, and the potential visual experiences perceived by the human fetus during gestation.

Our limited understanding of the visual environment in which the human fetus resides is problematic for several reasons. The womb is the starting point for human life, yet our understanding of its environment has traditionally been summarised by notions of a constantly dark or negligibly illuminated place [Myowa-Yamakoshi and Takeshita, 2006] or one which is only illuminated by bright external light sources [Liley, 1972]. In part due to this limited understanding of the womb's illumination, research into fetal vision lags that of other sensory experiences. It has long been known, for example, that the fetus can be stimulated by and respond to olfactory and auditory stimuli [Bradley and Mistretta, 1975; Lecanuet and Schaal, 1996].

Consequently, there has been limited research into the extent of visual capabilities for the human fetus until recent times. The work of Reid et al. [2017], for example, has demonstrated that the fetus can be engaged by transdermal stimuli delivered to the maternal abdomen, and research by Dunn et al. [2015] has shown the fetal brain responds to external light stimuli. Similarly, research focusing on understanding the illumination of the womb was highly limited prior to this thesis, with the primary contribution to the subject being the work of Del Giudice [2011], who used multiple regression modelling to estimate the potential for uterine illumination. This work had several limitations, as discussed in Chapter 2, which resulted in minimal applicability and extension to further research.

This thesis has approached the problem of quantifying uterine illumination and exploring the uterine visual environment in an entirely new and novel way when compared to previous work in the field. In Chapter 3, we outlined the typical algorithm employed in tissue optics modelling before introducing a custom-built mathematical model utilising Monte Carlo methods in Chapter 5 with application to a planar, multi-layered maternal tissue environment to simulate experimental stimuli [Isaac et al., accepted, 2024]. This work is, to our knowledge, the first instance where the uterine illumination from external point source stimuli has been quantified via Monte Carlo methods. Alongside an exploration of the impacts to this illumination from adipose tissue variation, this work suggests that a 5 mW point source laser diode stimuli delivered to the maternal abdomen at a 650 nm wavelength may provide illumination of the immediate uterine environment in the range between that of an overcast night sky and a full moon in clear conditions (depending on the thickness of adipose tissue). Hence, this provides the field's first quantified estimate from mathematical modelling of the visual experience provided to the human fetus by experimental light sources.

The field of fetal vision research is growing, and the implications of this work are significant for several areas. Primarily, the research was conducted to assist experimental practitioners in determining the appropriate intensity of stimuli delivered to the maternal abdomen to achieve specific experimental design outcomes. A component of the work explored the potential images seen by the fetus from such stimuli under varying adipose tissue thicknesses, with direct applicability to such experimental research. Further, however, this research may find use in fields such as photoacoustics, where internal imaging based on heat emission resulting from external stimuli depends heavily on the interplay between light and tissue.

In Chapter 7, we extended this work to assess the relationship between delivered intensity to the fetus and varying stimuli wavelengths. From these simulations, we generated an approximation for a natural light source and extended the source region to cover a large region of the maternal abdomen. This allowed for an estimation of the upper limit of uterine illumination provided by sunlight incident upon the maternal abdomen, with initial estimates suggesting it is comparable to that of a full moon under clear conditions or civil twilight [Isaac et al., under review, 2024]. Further extensions to the model allowed for an estimate of the impact to uterine illumination from a typical layer of clothing (such as a shirt), with simulations suggesting that the presence of clothing reduces the potential illumination from direct sunlight to roughly the level of a clear, starry night or that of a quarter moon. Following our previous work, this research offers the first exploration of uterine illumination under everyday lighting from sunlight.

The applicability of this work spans beyond simply being interesting and novel. In an age where ectogenesis moves ever closer to reality for humans, an understanding of the illumination of the uterus as a function of everyday lighting is increasingly important. Experimental research into artificial wombs has seen success with animal trials [Partridge et al., 2017], paving the way for future work on applying similar concepts to human fetuses [Kozlov, 2023]. The development of such products requires explicit consideration of the material's optical properties to accurately replicate the human uterus. Allowing too much, or not enough, light to penetrate the artificial womb may lead to detrimental visual outcomes for neonates due to over- (or under-) exposure to light during gestation.

Similarly, there is research that suggests environmental lighting conditions may impact visual outcomes for the human fetus. Rao et al. [2013], for example, found that the formation of mouse eyes has an essential dependence on levels of uterine light, while work by Yang et al. [2013] concluded that higher average day length during early gestation for human fetuses was associated with reduced likelihood of developing severe retinopathy of prematurity. Evidently, the human visual system may be impacted by the number of daylight hours experienced during gestation. Through initiating the conversation for further exploration of the human uterine illumination under daylight conditions, the work of Chapter 7 holds clear implications for the field of tissue optics and human development.

In Chapter 9, we made the final contributions of this thesis. By extending our previously planar tissue model to account for curvature of the womb, we introduce the field's first exploration of the interplay between light and the entire human womb [Isaac et al., forthcoming, 2024]. Previously, our models did not include the full uterine environment, due to their assumption of maternal abdominal tissue being locally flat — obviously ignoring effects due to tissue curvature. Similarly, this planar assumption introduced aspects of tissue homogeneity, with constituent layers (such as adipose or muscle) required to be consistent thicknesses across the region. The work of Chapter 9 eases these assumptions and allows for a more accurate representation of the uterine environment, with results consequently modelling illumination of the womb in a more physically accurate manner.

The initial implications from the work in Chapter 9 are substantial, with several obvious potential applications to the fields of fetal vision, human development, and ectogenesis in line with those mentioned in the above discussion. Further, however, this expanded model opens the door for many future expansions, pathways, and improvements. These are discussed in the following section.

10.3 Limitations and Potential Improvements

Despite this thesis presenting a detailed progression of increasingly sophisticated contributions to the field, building from a relatively simple exploration of experimental situations to a full model of the human womb, there are several limitations evident within the work. Here, we discuss a selection of these points and suggest possibilities for improvements in the future.

Though the work of Chapter 9 was fundamental in opening the door for broader investigations of the uterine visual environment [Isaac et al., forthcoming, 2024], there are two primary limitations of the model from a practical sense. Firstly, despite the assumption of the maternal abdomen as ellipsoidal in shape being crucial in allowing a simple initial inspection of the problem, its applicability to the womb in reality is tentative. The use of concentric ellipsoids to model the womb and its preceding layers of tissue offers an initial estimate of the relationship between light and the uterus; however, it is not particularly relevant to the shape of many pregnant abdomens across the population, nor does it accurately reflect the shape of this region of the body across gestation. There is room for a more detailed examination of the best manner in which to approximate this region, and it may be the case that using ellipsoids is overly simplistic. In particular, as discussed in Section 2.6 of Chapter 2, it may be worthwhile modifying the model to allow for a more flexible approach to modelling curved surfaces. The use of cubic voxels requires increased resolution to more accurately model curved boundaries, as cubes will never correctly follow curves, and the tradeoff from a user perspective is computational time. By using, for example, triangles to create a mesh of the surfaces involved, one may more accurately model the precise curvature of the womb. An important point to consider, however, is the extent to which one desires to trade time spent adjusting the model's details for accuracy in individual simulations. Depending on this tradeoff, it may yet be the case that the use of cubic voxels (combined with surfaces that can be described analytically) is ultimately the best approach to delivering a generalised model.

Second, a feature that is lacking both from this final model and the works presented in the preceding chapters is the ability to quickly produce outputs relevant to different parameters and environmental conditions. Presently, any change of optical parameters or tissue conditions requires an entirely new simulation to be run within the model. Given that simulations typically require the simulation of over 10 billion photon packets, the loss of time to model computation is significant when simulating a range of scenarios. An extension to the model that remedies this aspect may be as simple as running many simulations once and building a database of key results and outputs. From there, interpolation and extrapolation and/or machine learning from previous results could be explored to speed up the processing for an end user. This is especially pertinent when considering that work such as that conducted within the thesis has clear applications in medical environments where practitioners are not necessarily able to wait hours for results — or, indeed, may not have access to appropriate optical parameters for specific tissues and wavelengths, nor readily available usage of high performance computer systems.

A significant limiting factor in using this type of model for simulating the interactions of light with tissue comes from its reliance on optical parameters for each constituent tissue medium. As detailed in Chapters 5 and 7, much time was invested in exploring existing literature to source wavelength-specific parameters, such as absorption and scattering coefficients, for the various tissue sub-layers built into the models. In Chapter 7, we employed an element of simple interpolation to generate some parameters for wavelengths where these values were not readily available [Isaac et al., under review, 2024]; however, this is not necessarily simple to do in practice, as it requires a library of values to base predictions on, which in turn typically requires literature research. This is an unfortunate limitation inherent in this type of modelling in tissue optics; however, one key improvement to consider would be an alteration of the model so that it is able to generate values itself. This may come via interpolation and extrapolation from a built-in library of parameters. Alternatively, there may potentially be scope to consider an upgrade to the mathematical aspects of the model so that it is able to generate its own parameters from, for instance, assumed water and oxygen composition of tissue mediums — both of which are examples of properties that typically determine the necessary coefficients for simulations [Jacques, 2013].

In Chapter 5, we explored the potential appearance of stimuli to the fetus after propagation and attenuation through maternal tissue [Isaac et al., accepted, 2024]. As noted in the paper, the precise determination of such aspects is inherently difficult due to individual variations in eye development and sensitivity, a present lack of understanding of the sophistication of the fetal eye, and uncertainties around the influence of background illumination provided by, for example, interior lighting. In practice, experimental practitioners may wish to utilise the results of this thesis in determining the appearance to the fetus of proposed stimuli; however, the model does not readily facilitate this feature. It is difficult to accurately describe precisely how a separate viewer may interpret and “see” visual stimuli. In Chapter 5, we have attempted to provide a suggestion of how experimental stimuli may appear to the fetus, but it is limited. Improvements related to this limitation are difficult to consider; however, there may be scope for a comparison between how the model performs in simulating light through a tissue phantom and how the light appears in reality after propagation. In this manner, it may be possible to “tune” the model’s estimation of stimuli appearances, though this is not an approach that has been thoroughly considered at this stage.

One final limitation present throughout this thesis has been the absence of any explicit consideration of anatomical structures such as vascular networks, skin heterogeneities (e.g., lesions or moles), and bone structures (in the case of [Isaac et al., forthcoming, 2024]). Early in the development of this thesis, consideration was given to the inclusion of a vascular network within a tissue layer via use of mathematical equations to generate repeating network structures that may replicate blood vessels; however, its implementation was not followed to conclusion due to its deviation from the research focus with potentially limited benefits. One primary benefit of having utilised a voxelated approach to generating tissue mediums comes in the form of a relatively simple approach to addressing this limitation. By altering the optical properties of specific voxels in a careful manner, we may introduce alternative mediums to the model with relative ease; however, we need accurate surfaces to account for aspects such as reflection and refraction. Hence, a future improvement may involve explicitly incorporating such structures into the simulated environment of the maternal abdomen via voxel manipulation or the introduction of iso-surfaces to generate the desired components.

10.4 Future Research

Within this thesis, we have explored a range of situations, scenarios, and problems relevant to uterine illumination and the delivery of light stimuli to the human fetus. Despite this, there are many avenues we wish to explore through future research via adjustments to, and applications of, this model. Several of these have been described in the preceding section; however, below, we outline three further directions.

The first relates to an application of the model to a field not considered in this thesis. Functional near-infrared spectroscopy (fNIRS) involves the delivery of near-infrared lasers (typically in the range of 650-950 nm) to the brain, the measurement and processing of consequent reflected light, and the determination of brain activity via the nature of the reflected light (see, for instance, the work of Chen et al. [2020]). Though this thesis is not necessarily concerned with the practicalities of experimental research, the work conducted within demonstrates the applicability of this model to practitioners. In particular, as an extension from the work of our wider research group, we intend to soon expand the model to allow for fNIRS studies to be simulated. This will allow for future studies in that field to be advised via computational modelling in a similar manner to the experimental studies involved with the work in Chapter 5.

Second, in our analysis thus far, we have not mentioned the effects due to skin tone. This comes down to the nature of the model, as it depends specifically on several key optical parameters (absorption and scattering coefficients, for example) that are sourced from literature where possible. These parameters typically relate directly to the tissue composition that informs aspects such as skin tone; however, a typical question one might ask when viewing the results of this thesis is: “How do these results change when we consider individuals of different skin tone?” With the current implementation of the model, we are limited to using optical parameters that may not necessarily relate to individuals of a specific background or race. Hence, one might imagine that our model essentially delivers an estimate of the average relationship between light and tissue — regardless of skin tone. Future work aims to more accurately describe the variations across individuals with respect to aspects such as skin tone, and this would provide individual value to users of the results.

Finally, the work presented in Chapter 9 presents an initial overview of how the interaction of light with the curved maternal abdomen differs from prior assessments based on a planar tissue model. In future research, we plan to provide a more comprehensive analysis of the variations in uterine illumination across a range of environmental and lighting conditions. For instance, we intend to explore comparisons between direct illumination from sunlight, incidental illumination from diffuse lighting indoors, and the range of uterine conditions presented from varying levels of sunlight. Similarly, we aim to relate these outcomes directly to a range of scenarios across the temporal aspect of gestation. In doing so, we will comprehensively assess the range of conditions and possibilities involved with uterine illumination and provide foundational approximations from which future researchers are able to build on in their own research endeavours.

10.5 Final Remarks

We wish to conclude by acknowledging two academic papers which much of this thesis has continued from. First, Reid et al. [2017] explored the stimulation of the fetal eye via point source laser diodes applied to the maternal abdomen. In their work, they assumed a presentation of three such stimuli arranged in an approximate face-like structure would attenuate to eventually present to the fetus as displayed in Figure 10.1.

Following this paper, Scheel et al. [2018] later explored the appearance of a similar set of stimuli via use of a computational model with similarities to the one employed within this thesis. After simulation, they found that the stimuli were perhaps better approximated as shown in Figure 10.2.

The discussion of differences between the simple approximation made by Reid et al. [2017] and the more comprehensive estimate provided by Scheel et al. [2018] has, to a large degree, spurred the production of this thesis and its associated research. Hence, to conclude, we offer an additional approximation of these stimuli, though this time through use of the model developed for

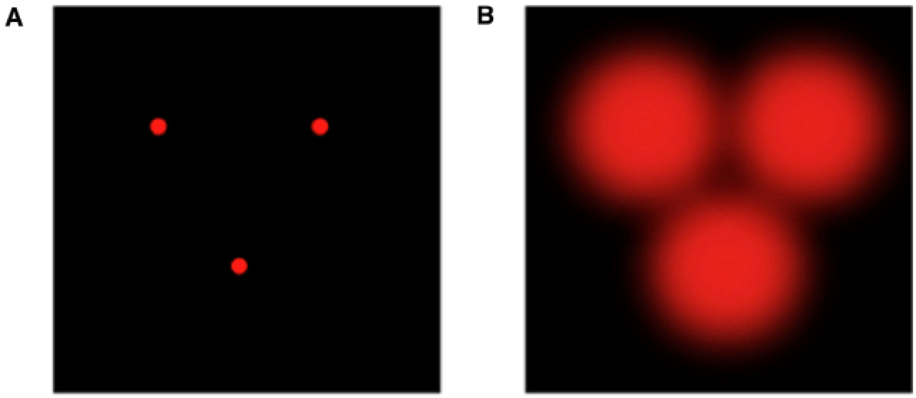

Figure 10.1: A: laser diodes as presented to the fetus by Reid et al. [2017]. B: image viewed by the fetus as estimated by Reid et al. [2017].

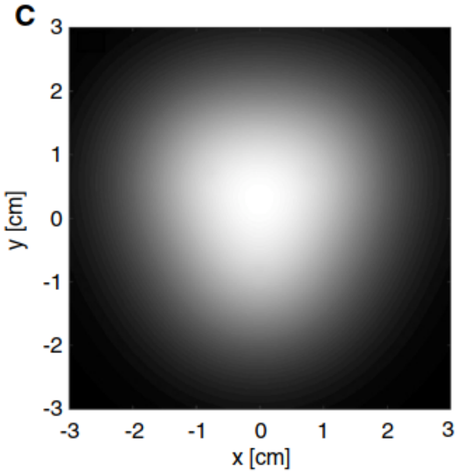

Figure 10.2: Image viewed by the fetus as estimated by Scheel et al. [2018].

Chapter 9. This is presented in Figure 10.3, mapped to a grid of θ and ϕ values to represent the precise stimuli location. The top image shows the relative fluence at skin delivery for three 650 nm point sources incident perpendicular to the tissue at approximate locations used by Reid et al. [2017], while the bottom image shows this upon entry to the womb. Note that some minor distortion is evident due to the projection of a curved, three-dimensional output onto a flat, two-dimensional image (in the same manner as world maps distort the true shape of a given land mass). This is not the case for Figures 10.1 and 10.2, as neither simulation accounted for curvature. If viewed on a curved surface, Figure 10.3 would exhibit a clearer separation and orientation of the dots.

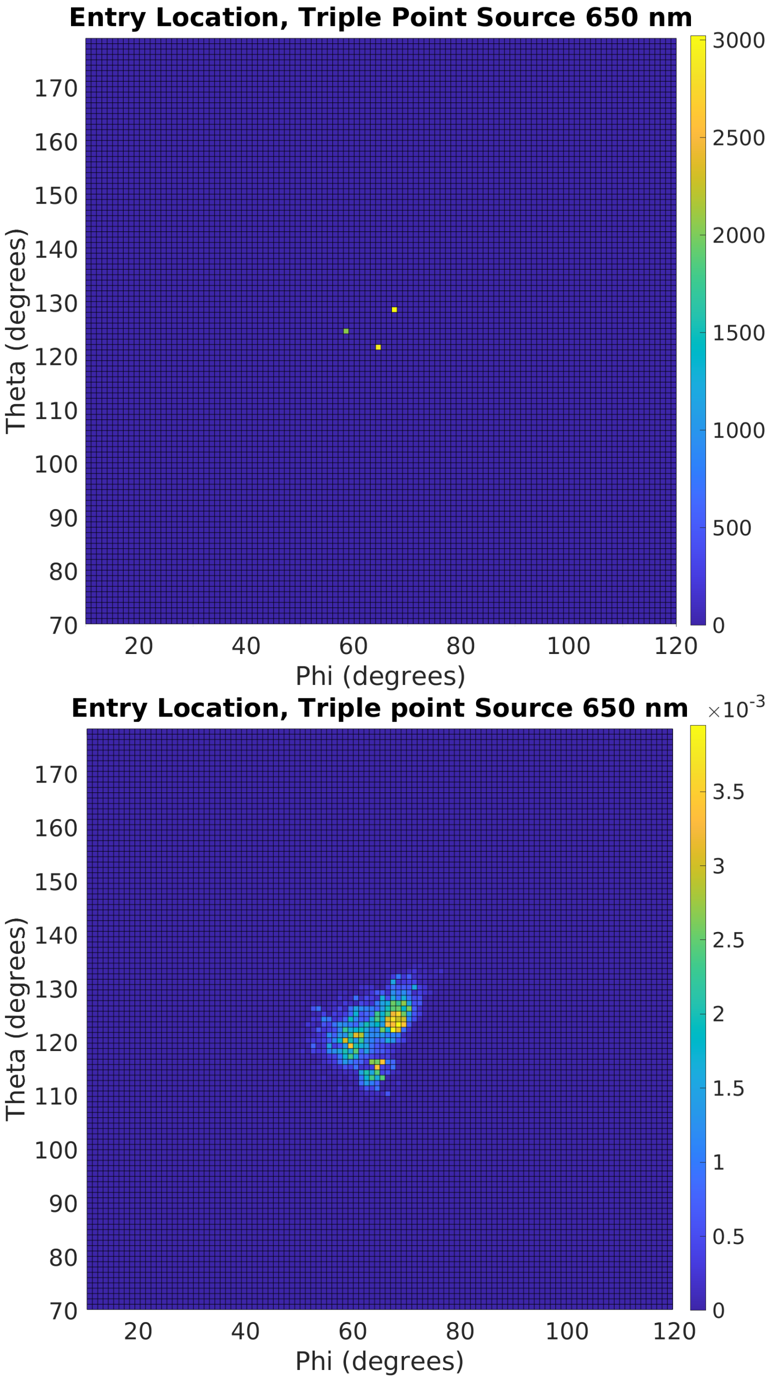

Figure 10.3: Top: Relative fluence (watts of power incident per cm^2 per W delivered) at skin delivery for three 650 nm point sources incident perpendicular to the tissue at approximate locations used by Reid et al. [2017]. Bottom: the same at entry to the womb. Theta is the angle measured from the positive x-axis, while phi is measured from the positive y-axis. Any pairing specifies an entry location. Note some minor distortion is evident due to the projection of a curved, three-dimensional output onto a flat, two-dimensional image.

Three clear regions of intensity can be seen in the uterus entry image, with some overlap evident due to the distortion mentioned above (but as discussed in Chapter 5, this is also perhaps due to stimuli being delivered too close together). Depending on the sensitivity of the fetal eye and its ability to discern similar intensities, this result would suggest that the image presented to the fetus by Reid et al. [2017] likely appeared less distinct than their initial estimate — yet more distinct than the estimate of Scheel et al. [2018]. In contrast to the previous work of these groups, this final result accounts for optical heterogeneity through the tissue medium by incorporating distinct layers, curvature of the womb by including non-planar surfaces, and varying tissue depths across layers due to the manipulation of ellipsoidal layer parameters. Consequently, this would presently appear to be the most physically accurate estimate of the appearance of such stimuli to the fetus.

References

R. M. Bradley and C. M. Mistretta. Fetal sensory receptors. *Physiological Reviews*, 55(3):352–382, 1975.

W. Chen, J. Wagner, N. Heugel, J. Sugar, Y. Lee, L. Conant, M. Malloy, J. Heffernan, B. Quirk, A. Zinos, S. Beardsley, R. Prost, and H. Whelan. Functional near-infrared spectroscopy and its clinical application in the field of neuroscience: Advances and future directions. *Frontiers in Neuroscience*, 14, 2020.

K. Das, T. Yuasa, I. Nishidate, H. Funamizu, and Y. Aizu. Simulated reflectance spectra and point spread functions in database constructed by moderate grouping of nine layers in skin model. *Optical Review*, 27, 02 2020.

M. Del Giudice. Alone in the Dark? Modeling the Conditions for Visual

Experience in Human Fetuses. *Developmental Psychobiology*, 53:214–219, 2011.

K. Dunn, N. Reissland, and V. M. Reid. The functional foetal brain: A systematic preview of methodological factors in reporting foetal visual and auditory capacity. *Developmental Cognitive Neuroscience*, 13:43–52, 2015.

Z. Isaac, J. Heerikhuisen, and V. Reid. The effect of adipose tissue on transdermal monochromatic light presented to the human fetus using Monte Carlo simulations. *Scientific Reports - Nature*, accepted, 2024.

Z. Isaac, J. Heerikhuisen, and V. Reid. Modeling the full human uterine visual environment. *Journal of the Royal Society Interface*, forthcoming, 2024.

Z. Isaac, J. Heerikhuisen, and V. Reid. Modeling the propagation of natural light to the human womb using Monte Carlo simulations. *Proceedings of the Royal Society B*, under review, 2024.

S. Jacques, D. Weaver, and S. Reppert. Penetration of Light Into the Uterus of Pregnant Mammals. *Photochemistry and Photobiology*, 45:637 – 641, 01 2008.

S. L. Jacques. Optical properties of biological tissues: a review. *Physics in Medicine & Biology*, 58(11):R37–R61, 5 2013.

M. Keijzer, S. Jacques, S. Prahl, and A. Welch. Light distributions in artery tissue: Monte Carlo simulations for finite-diameter laser beams. *Lasers in Surgery and Medicine*, 9:148–154, 1989.

M. Kozlov. Human trials of artificial wombs could start soon. Here's what you need to know. *Nature*, 621:458–460, 09 2023.

J. Lecanuet and B. Schaal. Fetal sensory competencies. *European Journal of Obstetrics & Gynecology and Reproductive Biology*, 68(1):1–23, 1996.

A. W. Liley. The foetus as a personality. *Australian & New Zealand Journal of Psychiatry*, 6(2):99–105, 1972.

M. Myowa-Yamakoshi and H. Takeshita. Do Human Fetuses Anticipate Self-Oriented Actions? A Study by Four-Dimensional (4D) Ultrasonography. *Infancy*, 10(3):289–301, 2006.

E. Partridge, M. Davey, M. Hornick, P. McGovern, A. Mejaddam, J. Vrecenak, C. Burgos, A. Olive, R. Caskey, T. Weiland, J. Han, A. Schupper, J. Connelly, K. Dysart, J. Rychik, H. Hedrick, W. Peranteau, and A. Flake. An extra-uterine system to physiologically support the extreme premature lamb. *Nature Communications*, 8:15112, 05 2017.

S. Rao, C. Chun, J. Fan, J. M. Kofron, M. B. Yang, R. S. Hegde, N. Ferrara, D. R. Copenhagen, and R. A. Lang. A direct and melanopsin-dependent fetal light response regulates mouse eye development. *Nature*, 494:243–246, 2013.

V. M. Reid, K. Dunn, R. J. Young, J. Amu, T. Donovan, and N. Reissland. The Human Fetus Preferentially Engages with Face-like Visual Stimuli. *Current Biology*, 27:1825–1828, 03 2017.

A. M. Scheel, S. J. Ritchie, N. J. L. Brown, and S. L. Jacques. Methodological problems in a study of fetal visual perception. *Current Biology*, 28(10): R594–R596, 2018.

M. B. Yang, S. Rao, D. R. Copenhagen, and R. A. Lang. Length of day during early gestation as a predictor of risk for severe retinopathy of prematurity. *Ophthalmology*, 120(12):2706–2713, 2013.

Appendix A

Co-Authorship Forms

The co-authorship forms related to the three articles included in this thesis are provided on the following pages.

THE UNIVERSITY OF
WAIKATO
Te Whare Wānanga o Waikato

Co-Authorship Form

Postgraduate Studies Office
Student and Academic Services Division
Wahanga Ratonga Matauranga Akonga
The University of Waikato
Private Bag 3105
Hamilton 3240, New Zealand
Phone +64 7 838 4439
Website: http://www.waikato.ac.nz/sasd/postgraduate/

This form is to accompany the submission of any PhD that contains research reported in published or unpublished co-authored work. **Please include one copy of this form for each co-authored work.** Completed forms should be included in your appendices for all the copies of your thesis submitted for examination and library deposit (including digital deposit).

Please indicate the chapter/section/pages of this thesis that are extracted from a co-authored work and give the title and publication details or details of submission of the co-authored work.

Chapter 5: The effect of adipose tissue on transdermal monochromatic light presented to the human fetus using Monte Carlo simulations.
Submitted to Scientific Reports, under peer review.

Nature of contribution by PhD candidate	Developed the model, conducted literature research, performed Monte Carlo simulations and subsequent analysis, and drafted the paper.
Extent of contribution by PhD candidate (%)	80%

CO-AUTHORS

Name	Nature of Contribution
Jacob Heerikhuisen	Supervised work, assisted with model development and analysis of data, and helped with drafting the paper
Vincent Reid	Provided input into the developmental psychology and experimental background and assisted with drafting the paper.

Certification by Co-Authors

The undersigned hereby certify that:

- ❖ the above statement correctly reflects the nature and extent of the PhD candidate's contribution to this work, and the nature of the contribution of each of the co-authors; and

Name	Signature	Date
Vincent Reid		29.05.24
Jacob Heerikhuisen	JHeerikhuisen	29/05/24

THE UNIVERSITY OF
WAIKATO
Te Whare Wānanga o Waikato

Co-Authorship Form

Postgraduate Studies Office
Student and Academic Services Division
Wahanga Ratonga Matauranga Akonga
The University of Waikato
Private Bag 3105
Hamilton 3240, New Zealand
Phone +64 7 838 4439
Website: http://www.waikato.ac.nz/sasd/postgraduate/

This form is to accompany the submission of any PhD that contains research reported in published or unpublished co-authored work. **Please include one copy of this form for each co-authored work.** Completed forms should be included in your appendices for all the copies of your thesis submitted for examination and library deposit (including digital deposit).

Please indicate the chapter/section/pages of this thesis that are extracted from a co-authored work and give the title and publication details or details of submission of the co-authored work.

Chapter 7: Modeling the propagation of natural light to the human womb using Monte Carlo simulations. Submitted to Proceedings of the Royal Society B, under peer review.

Nature of contribution by PhD candidate	Developed the model, conducted literature research, performed Monte Carlo simulations and subsequent analysis, and drafted the paper.
Extent of contribution by PhD candidate (%)	80%

CO-AUTHORS

Name	Nature of Contribution
Jacob Heerikhuisen	Supervised work, assisted with model development and analysis of data, and helped
	with drafting the paper.
Vincent Reid	Provided input into the developmental psychology background and assisted with
	drafting the paper.

Certification by Co-Authors

The undersigned hereby certify that:

- the above statement correctly reflects the nature and extent of the PhD candidate's contribution to this work, and the nature of the contribution of each of the co-authors; and

Name	Signature	Date
Vincent Reid		29.05.24
Jacob Heerikhuisen	JHeerikhuisen	29/5/24

THE UNIVERSITY OF
WAIKATO
Te Whare Wānanga o Waikato

Co-Authorship Form

Postgraduate Studies Office
Student and Academic Services Division
Wahanga Ratonga Matauranga Akonga
The University of Waikato
Private Bag 3105
Hamilton 3240, New Zealand
Phone +64 7 838 4439
Website: http://www.waikato.ac.nz/sasd/postgraduate/

This form is to accompany the submission of any PhD that contains research reported in published or unpublished co-authored work. **Please include one copy of this form for each co-authored work.** Completed forms should be included in your appendices for all the copies of your thesis submitted for examination and library deposit (including digital deposit).

Please indicate the chapter/section/pages of this thesis that are extracted from a co-authored work and give the title and publication details or details of submission of the co-authored work.

Chapter 9: Modeling the full human uterine visual environment with curvature using Monte Carlo simulations.
To be submitted to the Journal of the Royal Society Interface.

Nature of contribution by PhD candidate	Developed the model, conducted literature research, performed Monte Carlo simulations and subsequent analysis, and drafted the paper.
Extent of contribution by PhD candidate (%)	80%

CO-AUTHORS

Name	Nature of Contribution
Jacob Heerikhuisen	Supervised work, assisted with model development and analysis of data, and helped
	with drafting the paper.
Vincent Reid	Provided input into the developmental psychology background and assisted with
	drafting the paper.

Certification by Co-Authors

The undersigned hereby certify that:

- ❖ the above statement correctly reflects the nature and extent of the PhD candidate's contribution to this work, and the nature of the contribution of each of the co-authors; and

Name	Signature	Date
Vincent Reid		29.05.24
Jacob Heerikhuisen	JHeerikhuisen	29/05/24